3. THEORY OF THE X-RAY ABSORPTION SPECTRAL SHAPES

In this chapter the theory of the x-ray absorption spectral shapes is discussed. In section 3.1 a short historical account of x-ray absorption is given. The emphasis is on the strongly correlated limit; the history of the weakly correlated limit is described in detail in Ref. 1. Sections 3.2 to 3.7 describe the crystal field multiplet model, which is sued to describe the metal $2p$ x-ray absorption spectra. Section 3.2 gives a theoretical introduction to the important effects: atomic multiplets, the cubic crystal field and the multipole core hole interactions. Section 3.3 contains a paper which discusses the crystal field multiplet model to explain the metal $2p$ spectra for compounds with an empty $3d$-band and the paper in section 3.4 describes the spectra of systems with partly filled $3d$-bands. Section 3.5 discusses the effects of the $3d$ spin-orbit coupling and distortions from cubic crystal fields, section 3.6 the effects of polarization dependence and finally in section 3.7 the limits of the crystal field multiplet model are discussed. The chapter is concluded with a section describing the weakly correlated limit with electronic structure calculations within density functional theory.

3.1. History of x-ray absorption

The historical development of x-ray absorption started almost immediately after the discovery of the x-rays by W.C. Röntgen in 1895 [2]. Some important landmarks in the development of the x-ray absorption technique are outlined with the emphasis on the use of the x-ray absorption edge structure and the manner to derive information concerning the electronic structure of solids. The discussion of the early developments is mainly based on *A History of x-ray absorption fine structure* from R. Stumm von Bordwehr [1].

X-rays and atomic energy levels

The first big step in the use of x-rays came in 1913 with Moseley's identification of the x-ray energies with Bohr's atomic energy levels [3]. In the years before it was recognized that metals emit characteristic x-rays (Sagnac, 1898 [4]). This observation was systemized by Barkla, who notified two distinct series of characteristic x-ray energies which he named K and L [5]. In 1913 Bohr developed his atomic energy level theory [6], which was directly used by Moseley who found that the x-ray energies varied with the atomic number squared [3].

From lines to spectra

The next step was the recognition of the existence of 'fine structure' in the x-ray absorption lines. In his thesis W. Stenström noted that:

> *This intense absorption band is followed by an emission region and then by a weak second band* (W. Stenström, 1918 [7]).

This notion that the transition does not involve single lines, but can be structured was shown more convincingly for the chromium K edge by Fricke in 1920 [8]. With respect to the origins of the fine structure the notions of W. Kossel are important:

> *The greatest work has been done during the transition from the core to the surface, and the various paths that can still remove it from the immediate vicinity of the atom require only a small energy, [...] One is hopefully able to draw other conclusions concerning the phenomena that occur on the atom surface. This surface must depend, for instance, on the number of electrons that occupy it, i.e. on the ionization state of the atom. This is the point where the external conditions of the atom can have an influence on the Röntgen rays* (W. Kossel, 1920 [1,9]).

This notion is important because if the x-ray absorption process would yield only intra-atomic information it would be of little use in the study of the electronic structure of solids. The discovery of the fine structure is therefore the first sign that the electronic structure around the 'surface of the atom', or in other words the chemical bonding, is important for the x-ray absorption fine structure. Related to this are the first observations that the valency influences the energy of the x-ray absorption edge [10]. The trends were explained by Pauling as the effect of screening from the neighbouring atoms [11].

X-ray absorption spectra of atoms

After the foundation of quantum mechanics [12,13], the explanation of the x-ray absorption spectra of hydrogen developed quickly and a detailed ab-initio picture evolved [14]. Thereafter the development of the interpretation of more complex atoms was hampered mainly by the 'mathematical' problems to describe the electron-electron interaction. If the wavefunctions of the initial state and final state configurations are determined, the calculation of the transition probability is accomplished with the application of the Wigner-Eckart theorem, with its implicit selection rules, and the calculation of the radial overlap [15].

X-ray absorption spectra of solids

The interpretation of x-ray absorption spectra in solids and the related theory of the electronic structure of solids developed much slower. An important step was taken by Kronig, who developed a scattering theory to explain the intensity modulations in the x-ray absorption spectrum [16,17]. From Kronig's theory there is an almost straightforward development to the interpretation of the extended x-ray absorption fine structure (EXAFS):

The later progress of x-ray absorption spectra calculations was to gradually free oneself from Kronig's hypotheses (C. Brouder, 1989 [18]).

An important experimental result which confirmed the importance of the crystal structure was given by Veldkamp who showed that the iron K edge of fcc-NiFe is equivalent to fcc-nickel and not bcc-iron [19]. Kronig's theory was developed further by Smoluchowski [20] who found good agreement for his 'single scattering' theory with all structures above 50 eV from the edge.

In the thirties it became evident that Kronig's scattering theory did not take into account the transition rules correctly. The overlap of the core state with the final state is more important for shallow core levels, especially if the principal quantum number is not modified. In the band structure model the transition probability is equal to the transition matrix element times the partial density of states [22, 23]. In principle this formula is still used as the basis for x-ray absorption calculations, though the original method to calculate the partial density of states has been shown to be incorrect [24]. The band structure approach developed to explain the near edge structure, with its implicit assumption of the neglect of the effects of the core hole as well as the extra valence electron as will be discussed in section 3.8. The scattering theory developed for the analysis of the EXAFS spectra and the multiple scattering formalism became the usual model for determination of the near edge structure of hard x-ray spectra [25].

3.1.1. Atomic transitions in solids

Both the band structure and the multiple scattering approaches are valid within the weakly correlated limit. Systems which are strongly correlated are not described correctly within this limit and during the years it became evident that some x-ray absorption spectra were completely dominated by the intra-atomic interactions with none or little influence from the electronic structure of the valence electrons.

The development of the strongly correlated limit, largely excluded from Ref. 1, can be traced back to the thirties, but really started with Rule's 1945 paper on the $3d$ ($M_{4,5}$) edge of samarium, in which he observed a subsidiary absorption maximum on the low energy side of the principal absorption [28]. He attributed this, following the ideas of Lindberg [26] and Sandström [27], to a pre-edge structure related to localized $3d$ to $4f$ transitions, while the remainder was attributed to the principal $M_{4,5}$ edge.

This division into localized $3d \rightarrow 4f$ transitions and the 'true' edge, was maintained in the initial studies of the Leicester group [29, 30] For example in his study on the $3d$ edges of praseodymium, neodymium, samarium and europium (oxides), Zandy used this division and identified the localized pre-edge peaks in all edges except the M_5 edge of europium [30]. In 1966 K.C. Williams, also from the Leicester group, recognized that the division into pre-edge and 'true' absorption edge was basically incorrect [31]. He concluded that the whole edge structure is related to the localized $3d^{10}4f^N \rightarrow 3d^9 4f^{N+1}$ transition:

Absorption into the 4f shell is permitted by the x-ray absorption selection rules and may be generally represented by the transition of an electron from an initial

state $3d^{10}4f^N$ to a final state $3d^94f^{N+1}$. If strict jj-coupling is assumed between the $3d^9$ and $4f^{N+1}$ groups, then for Yb one transition is possible for the M_5 edge and none for the M_4. In the case of Tm, three M_5 transitions are possible and one M_4. This evidence seems to indicate that most of the large increase in $M_{4,5}$ absorption for these elements can be explained by attributing it to transitions into the 4f shell and that very little 'edge' absorption is occurring (K.C. Williams, 1966 [31]).

For the $M_{4,5}$ edge of Eu_2O_3 (Eu^{3+}-$4f^6$) Williams concludes:

For the particular case of trivalent Eu, it is possible for 107 *M_5 and* 79 *M_4 transitions to occur into the 4f shell. It is scarcely surprising therefore that the absorption spectra should be banded and complex, as illustrated* (K.C. Williams, 1966 [31]).

Although Williams' arguments can be considered as quite convincing the 1967 paper of Zandy [32] and the 1968 paper of Combley et al. [33] still used the original division into 'pre-edge' and main edge.

Also in 1966 high resolution x-ray absorption spectra of the 4*d* ($N_{4,5}$) edges of rare earth metals became available through the work of the Leningrad group [34, 35]. The spectra showed apart from the main absorption edge a whole series of small and extremely sharp 'pre-edge' peaks as is shown in figure 3.1. These peaks were, like the $M_{4,5}$ edges, were identified as atomic 4*d* to 4*f* transitions:

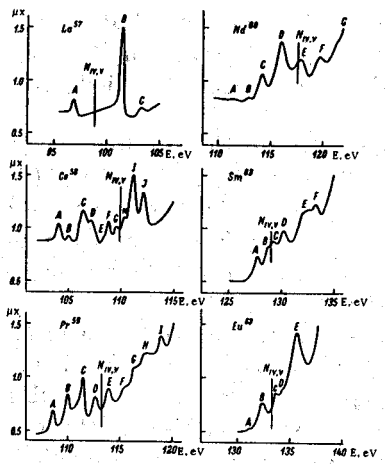

Figure 3.1: The 4*d* x-ray absorption spectrum of lanthanum, cerium, praseodymium, neodymium, samarium and europium. Taken from Fomichev et al. [35].

It is possible that the structure of the spectra corresponds to the transition of positive ions of the metals from an initial state with electronic configuration $4f^N$ to a final state $4d^94f^{N+1}$, the ions being bound in a solid state lattice. (Fomichev et al., 1966 [35]).

In 1970 the first synchrotron experiments on the $4d$ edges of the rare earths were performed by Haensel et al. [36]. They measured cerium, praseodymium and neodymium and found that for Pr and Nd the spectra of the oxides were identical to those of the pure metal, which confirmed the atomic nature of the transitions, or in other words the insensitivity of the $4d$ edge to chemical variations.

Williams' qualitative arguments for the attribution of the whole spectrum to transitions to the 4f states were shown to be correct in the early seventies when atomic multiplet calculations were performed in the groups of Fano and Cooper. Based on the interpretation of x-ray absorption in atoms [37], the 'atomic transitions in solids' were described in a series of papers by Dehmer, Starace, Sugar, Fano and Cooper [38–42] The emphasis was on the rare earth $4d$ edges which are marked by a series of small, sharp peaks (see figure 3.1), followed by a strong and asymmetric absorption edge.

The basic idea was that the complete spectrum can be described as the transition from the $4f^N$ ground state to $4d^9 4f^{N+1}$ final states. The separation into the low energy and high energy part originates from the so-called centrifugal barrier [38]: the high energy states autoionize which gives them their asymmetric Fano lineshape [37], whereas for the low energy peaks autoionization is prevented by the centrifugal barrier. Therefore the low energy states are relatively stable and thus sharp. The calculations showed that the final state multiplet is dominated by the df Slater integrals and is spread over about 20 eV, whereby nearly all intensity goes to the high energy states. The calculations used the computer code of C. Froese [43] to determine the Hartree-Fock values of the Slater integrals, and the resulting dipole spectrum was in agreement with the main features of the experimental results [38]. To optimize the result the df Slater integrals were reduced to 75% and the ff Slater integrals were taken from optical experiments [44].

The success of the calculations led Dehmer et al. to the prediction that their model could be extended to the $3p$ edges of the $3d$ transition metals. Simultaneously E.J. McGuire [45] predicted strong autoionization for the $3p$ edges due to the super Coster-Kronig process $3p^5 3d^{N+1} \rightarrow 3p^6 3d^{N-1} \varepsilon f$; εf denotes a continuum state of f-symmetry. At that time some spectra had been measured with line sources during the fifties [46] and a first set of high resolution spectra had been taken in 1969 with the DESY synchrotron by Sonntag et al. [47]. The spectra were broad and did not show a sharp edge but a rising intensity over some eV, which could be interpreted within the autoionization framework. A more detailed interpretation was not possible as the spectra were rather monotonic and did not show any pre-edge structures. The ideas concerning autoionization were developed further by Dietz et al. [48]; they were generalized by Davis and Feldkamp [49,50] and definitively confirmed by the high resolution data on manganese atoms [51]. In the following p[arts emphasis is given to the multiplet structures; more information concerning the autoionization effects can be found in the review article of Davis [52].

In 1974 S.-I. Nakai et al. measured the $3p$ edges of the $3d$-metal halides which, in contrast to the metals, showed sharp pre-edge peaks [53]. Their original interpretation was mainly bandstructure oriented and they used the distinction into localized $3p \rightarrow 3d$ transitions for the pre-peaks and a density of states interpretation for the 'main edge'. Figure 3.2 gives the results for some manganese halides. From these figures Nakai et al conclude:

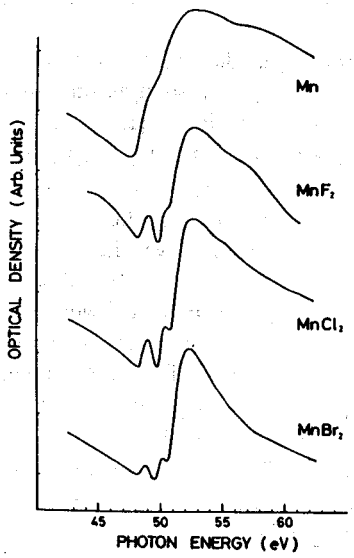

Figure 3.2: $3p$ x-ray absorption spectrum of manganese halides. Taken from Nakai et al. [53].

The absorption curves of MnF_2, $MnCl_2$ and $MnBr_2$ are very similar to one another, nevertheless these halides have different crystal structures..... The detailed structures in the low energy structures may be due to the $3p^5 3d^{N+1}$ multiplet (including the crystalline field splitting). (Nakai et al.,1974, [53]).

In their 1981 paper Shin et al. present the $3d$ spectra of $KMnF_3$ and $KCoF_3$ [54]. The spectra shown are identical to those of the halides, but the interpretation changed:

We assign the most part of the observed $M_{2,3}$ spectra to the $3p^6 3d^N \rightarrow 3p^5 3d^{N+1}$ transitions, contrary to the propositions given for other transition metal compounds in Refs. 53, 55 (Shin et al.,1981 [54]).

The spectra were consequently calculated with a crystal field multiplet program (discussed in detail in the next sections). The multiplet approach was originally developed simultaneously in Tokyo [56–58] and Winnipeg [59, 60] to study core level photoemission spectra. Though the core level photoemission experiments were in 'good agreement with the calculations' [60,61], the shortcomings of the approach were already indicated by Asada et al., who, following Refs. 62, 63, noted that the satellites are related to electron transfer from the ligand to the metal. In their 1976 paper, Asada and Sugano combined the multiplet model with charge transfer [64]. The hypothesis of charge transfer was shown to be correct by the calculations of Zaanen et al. who, using an Anderson impurity model, could explain all divalent nickel-halide spectra consistently [65]. For x-ray absorption the crystal field multiplet approach proved to be better suited (see section 3.2): Shin et al. neglected all states but the Hund's rule ground state and calculated the multiplet spectrum, neglecting also the $3d$ spin-orbit coupling. The $3d3d$ interactions were taken from experiment and the $3p3d$ multipole interactions were taken from atomic spectra but were reduced to approximately 60% [66]. The analysis was developed further in Ref. 67,68. Figure 3.3 is reproduced from

Ref. 68 and shows the spectral variations with changes in the cubic crystal field, from which it can be concluded that the spectral variations are not large and, given the uncertainties in the atomic parameters, it is difficult to use the $3p$ spectra for a detailed optimisation of the cubic crystal field value. However the calculations convincingly explain the spectral variations. The asymmetric lineshape of the high energy lines was explained qualitatively as autoionization [37,52].

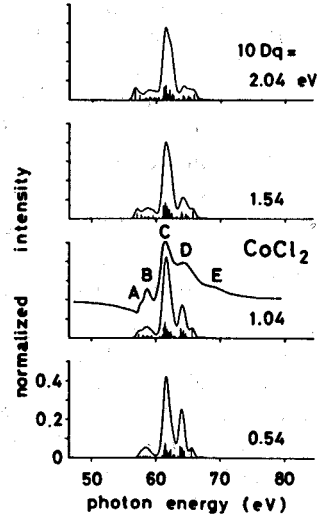

Figure 3.3: Cubic crystal field calculation for divalent cobalt. Taken from Shin et al. [68].

The calculations were generalized for all transition metal ions and for the $2p$ x-ray absorption as well as $2p$ XPS by Yamaguchi et al. [69,41]. In 1985 Thole et al. calculated all $4f^N \rightarrow 3d^9 4f^{N+1}$ transitions for the divalent and trivalent rare earth ions [71], using Cowan's atomic Hartree-Fock program [15,72]. Basically the calculations are equivalent to those performed by the groups of Fano and Cooper in the early seventies [38–41], but the improvement in computers made it possible to calculate a general $3d^9 4f^{N+1}$ multiplet in intermediate coupling, making use of (scaled) Hartree-Fock calculated Slater integrals and spin-orbit couplings. The agreement with experiments on rare earth metals convincingly confirmed the basic correctness of the method [71]. The atomic multiplet method was also used for the calculation of the $3d^5 \rightarrow 2p^5 3d^6$ multiplet to simulate spectra of manganese impurities in noble metals [73]. Again a basic agreement was found and the ground state could be identified as the Hund's rule ground state. The method was extended by B.T. Thole to include crystal field effects. The output of the atomic multiplet program was connected with the general group theoretical program of Butler [53]. The method is similar to the one used by Yamaguchi et al. [69,41], but it is made more general as $3d$ spin-orbit coupling can be included and the group theoretical projection can be made to any point group of interest. The first results of the method were given in Refs. 75,76.

3.2. The crystal field multiplet model

In this section the basic ingredients of the crystal field multiplet model are discussed. Sections 3.3 and 3.4 are reproductions of papers on the results of the calculations with a cubic crystal field. Limitations and extensions of the model are discussed in section 3.5 to 3.7.

3.2.1. Atomic multiplets

The general starting point for the strongly correlated limit is the atomic multiplet theory which describes the correlated electronic states in partly filled atomic shells. A single $3d$ electron has ten possibilities, respectively spin-up and spin-down states with m_l ranging from -2 to 2. The overall quantum numbers L and S of a $3d^1$ configuration are 2 and $\frac{1}{2}$. The total J quantum number has two possibilities, respectively $\frac{3}{2}$ (L-S) and $\frac{5}{2}$ (L+S). In term symbol notation, representing irreducible representations in spherical symmetry: ${}^{2S+1}L_J = {}^2D_{\frac{5}{2}}$ and ${}^2D_{\frac{3}{2}}$. LS-coupling is a correct description for the valence electron couplings of the light elements because the $3d$ spin-orbit coupling is rather small [77]. Thus the spin and angular momenta of the $3d$-electrons are first coupled to an overall L and S. In pure LS-coupling the 45 combinations of a $3d^2$-configuration are grouped in the term symbols ${}^1G$, ${}^3F$, ${}^1D$, ${}^3P$ and ${}^1S$. If jj-coupling is considered as a small perturbation the irreducible representations are indicated by their general ${}^{2S+1}L_J$ term symbol, i.e. ${}^1G_4$, ${}^3F_4$, ${}^3F_3$ ${}^3F_2$, ${}^1D_2$, ${}^3P_2$, ${}^3P_1$, ${}^3P_0$ and ${}^1S_0$. However if the jj-coupling becomes more dominant this term symbol notation loses its meaning as the states with equal J's start to mix and the states have to be described as linear combinations of term symbols. Finally in pure jj-couplings only 5 irreducible representations remain, distinguishable by their J-value only. The 'transition' from LS to jj coupling is indicated in figure 3.4.

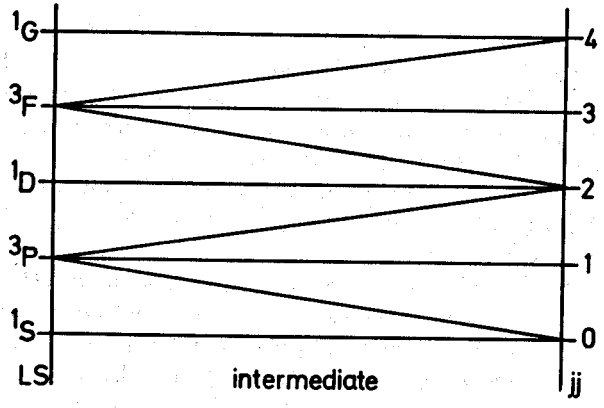

Figure 3.4: $LS \rightarrow jj$ transition for $3d^2$. In table 3.2 the physical ordering for LS-coupling is given.

If a $3d^3$-configuration is coupled according to LS-coupling there are 120 configurations divided over the term symbols: ${}^4F$, ${}^4P$, ${}^2H$, ${}^2G$, ${}^2F$, ${}^2D$ (2 times) and ${}^2P$. The main problem to solve is to find the wavefunctions of these term symbols. One way to proceed is

to couple first two electrons to $|d^2\mathbf{LS}\rangle$ and subsequently couple this with the third electron. From symmetry arguments and recoupling formulae it can be shown [15] that the overall wavefunction $|d^3\mathbf{L'S'}\rangle$ can be formed by a summation over all LS combinations of the two-electron wave functions multiplied by a specific coefficient:

$$|d^3\mathbf{L'S'}\rangle = \sum_{\mathbf{L,S}} |d^2\mathbf{LS}\rangle \cdot c_{\mathbf{LS}} \tag{3.1}$$

For example the quartet F state of $3d^3$ is built from its parent triplet states as:

$$|d^3[^4F]\rangle = \frac{4}{5}|d^2[^3F]\rangle - \frac{1}{5}|d^2[^3P]\rangle \tag{3.2}$$

Similarly all other $3d^3$ states can be built. They are denoted as $(d^2LS|\}\alpha LS)$ and are called *Coefficients of Fractional Parentage*, because the $3d^2$-states can be considered as the 'parents' of the $3d^3$-states. The coefficients for all partly filled d and f states are tabulated by Nielsen and Koster [78].

Core hole effect on atomic multiplets

Up to now only partly filled $3d$-states were considered. In the final state of the metal $2p$ x-ray absorption process a $2p^5 3d^{N+1}$ configuration is formed. As the dominant interaction is the core hole spin-orbit coupling, the actual coupling scheme is given as jj-coupling for the core hole and LS-coupling for the valence electrons. The overall coupling scheme is a mixture of both. The simplest 2p3d coupling is the $2p^5 3d^1$ state. The configurations are found from multiplying (the symmetries of) the $2p^5$ state with the $3d^1$ state.

$$^2P \otimes {}^2D = {}^1P_1 + {}^1D_2 + {}^1F_3 + {}^3P_{0,1,2} + {}^3D_{1,2,3} + {}^3F_{2,3,4} \tag{3.3}$$

Figure 3.5 sketches the transition from pure LS to jj coupling for the pd-multiplet. For configurations with two or more $3d$ electrons (and the $2p$ core hole) the intermediate coupling scheme makes a term symbol assignment of the states inappropriate.

In section 1.2 it was discussed that for x-ray induced transitions the dipole selection rules are applicable, i.e. $\Delta L = \pm 1$, $\Delta S = 0$ and $\Delta J = \pm 1, 0$ with $J + J' \geq 1$. Therefore in LS-coupling the transition from $3d^0 \rightarrow 2p^5 3d^1$ is a non-degenerate single line, because the the dipole selection rules allow only a ^1P final state. In jj-coupling the selection rules yield a (threefold degenerate) $J = 1$ final state; in the actual intermediate coupling scheme three states exist. In figure 3.5 it is shown that the degeneracy of the $J = 1$ is lifted. The actual states are described as linear combinations of the $^1P_1$, $^3P_1$ and $^3D_1$ term symbols.

Slater integrals, Racah parameters and Hund's rules

The origin of the term splittings can be found in the electron-electron interactions and the spin-orbit coupling. The usual method of determining the 2-electron integrals is by

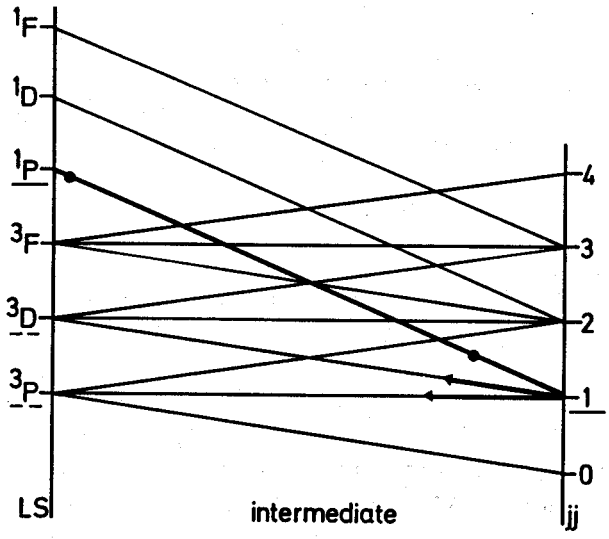

Figure 3.5: $LS \rightarrow jj$ transition for $2p^5 3d^1$. In LS-coupling only the $^1P_1$-state can be reached, but in intermediate coupling there is admixture of the $^1P_1$-state with the $^3P_1$-state and the $^3D_1$-state.

expanding them as a series of Legendre polynomials [15, 79, 12]. The radial part reduces to the integrals:

$$R^k(ab,cd) = \int_{r_1}\int_{r_2} \frac{r_<^k}{r_>^{k+1}} \cdot P_1(a)P_2(b)P_1(c)P_2(d)\, dr_1 dr_2 \tag{3.4}$$

It is common practice to divide the radial integrals in Coulomb terms and exchange terms. The Coulomb terms are denoted as $F^k(ab,ab) \Rightarrow F^k(a,b)$ and the exchange terms as $G^k(ab,ba) \Rightarrow G^k(a,b)$, the so-called Slater integrals. The angular part composes strong selection rules on the k-values in the series expansion, i.e. for two $3d$-electrons only F^0, F^2 and F^4 are possible and for a pd-interaction F^0, F^2, G^1 and G^3 have to be considered. Instead of the F^k, G^k superscript notation two alternative notations are used: in the subscript F_k notation the F^k Slater integrals are renormalised with a common k-dependent denominator D_k [79]. Another common notation for dd-interactions are the Racah parameters A, B and C. Table 3.1 gives their relation to the Slater integrals.

The effect of the electron-electron interaction on the $3d^2$ configuration is that the term symbols have the relative energies as given in table 3.3. The energy positions in this table reveal that the ground state of the $3d^2$ configuration is the ^3F state, which is an example of the rule that for a general $3d^N$ configuration the ground state is always the state with highest S, and for these states the state with the highest L: *Hund's rules* [82]. The Hund's rules are a direct consequence of the multipole dd-interaction described with the Slater integrals: S (and L) are maximized because the electron-electron repulsion is minimized if the electrons belong to different m_l-orbitals and also because electrons with parallel spin have an additional exchange interaction which lowers the total energy. If the ^3F-state is split due to $3d$ spin-orbit coupling the ground state is, according to Hund's third rule, the state with the lowest J (the $^3F_2$-state); in case more than five $3d$-electrons are present, the highest J-value has lowest energy. Notice that the Hund's rules do not explain the ordering

Racah	Slater Integrals
A	$= F^0 - F^4/9$
B	$= (9F^2 - 5F^4)/441$
C	$= 5F^4/63$

Table 3.1: Relation of Slater integrals with Racah parameters for $3d$-electrons

Symmetry	Relative energy	
$E(^1S)$	$14B + 7C$	+4.2 eV
$E(^1D)$	$-3B + 2C$	+0.5 eV
$E(^1G)$	$+4B + 2C$	+1.2 eV
$E(^3P)$	$+7B$	+0.7 eV
$E(^3F)$	$-7B$	−0.8 eV

Table 3.2: Relative energy positions of a $3d^2$ configuration. For the values in the third column the representative values B=0.1 eV and C=0.4 eV are used.

of the states, but only the symmetry of the ground state. In the final state of the metal $2p$ x-ray absorption process the dominant interaction is the core hole spin-orbit coupling (ξ_{2p}). Its magnitude ranges from about 3 eV for titanium to about 10 eV for nickel. If only this spin-orbit coupling is considered the $2p$ spectra are split in two , the L_3 and the L_2 edge, separated by $\frac{3}{2} \cdot \xi_{2p}$. The pd Coulomb and exchange terms, F^2_{pd}, G^1_{pd} and G^3_{pd}, are of the order of 5 to 10 eV and from table 3.3 it can be seen that the dd-interactions cause splittings of the order of 5 eV. The combination of the core hole spin-orbit interaction and the $3d3d$ and $2p3d$ electron-electron interactions gives for the general case of a $2p^5 3d^N$ configuration a complex distribution of states. The $3d$ spin-orbit coupling is small and possible effects are discussed in section 3.5.

The specific values of the pd-Slater integrals and the $2p$ spin-orbit coupling give the atomic multiplet spectrum of the $3d^0 \rightarrow 2p^5 3d^1$ transition two intense lines with an additional small 'pre-edge' peak (see section 3.4). The atomic multiplet for $3p$ x-ray absorption is described with exactly the same coupling scheme. However because the $3p$ spin-orbit coupling is relatively small and the $3p3d$ Slater integrals large, the coupling scheme is almost pure LS and more than 99% of the transition goes to the final state of ^1P-symmetry[1].

[1]The energy of the ^1P-state is about 10 eV above the lowest state, and this is the origin of the 'delayed onset' in $3p$ resonant photoemission experiments.

3.2.2. The cubic crystal field

Atomic multiplet theory can be extended to describe the $3d$-metal ions by incorporation of the dominating cubic crystal field. As an introduction first the cubic crystal field, which is the central phenomenon in describing the electronic structure of $3d$ transition metal ions [12,44], is introduced:

In an octahedral environment the potential of the central ion has cubic (O_h) symmetry which divides the 5-fold degenerate $3d$-orbitals into two distinct representations of T_{2g} and E_g symmetry. The twofold degenerate E_g state contains orbitals which point towards the center of the cube faces, that is directly towards the position of the ligands. Consequently they interact stronger, electrostatically as well as covalently, with the ligands. The three t_{2g} orbitals point towards the corners of the cube and therefore their interaction with the octahedral ligands is considerably lower. The five $3d$ electron-pairs, ($|JM_J\rangle =$) $|\bar{2}0\rangle$, $|\bar{1}0\rangle$, $|00\rangle$, $|10\rangle$ and $|20\rangle$, are regrouped by a cubic crystal field as indicated in table 3.3.

representation	orbital name	atomic states	Cartesian notation
E_g	d_{z^2}	$\|20\rangle$	$\frac{1}{2}(3z^2 - r^2)$
	$d_{x^2-y^2}$	$\frac{1}{\sqrt{2}}\|2\bar{2}\rangle + \frac{1}{\sqrt{2}}\|22\rangle$	$\frac{\sqrt{3}}{2}(x^2 - y^2)$
T_{2g}	d_{xy}	$\frac{1}{\sqrt{2}}\|2\bar{2}\rangle - \frac{1}{\sqrt{2}}\|22\rangle$	$\sqrt{3}(xy)$
	d_{yz}	$\frac{1}{\sqrt{2}}\|2\bar{1}\rangle + \frac{1}{\sqrt{2}}\|21\rangle$	$\sqrt{3}(yz)$
	d_{zx}	$\frac{1}{\sqrt{2}}\|2\bar{1}\rangle - \frac{1}{\sqrt{2}}\|21\rangle$	$\sqrt{3}(zx)$

Table 3.3: Effect of a cubic crystal field on a $3d$ electron

In the following the effects of the cubic crystal field on the electronic structure of a partly filled $3d$-band are considered. For this purpose two models are used:

- A simplified 'spin dependent molecular orbital' model which accounts only for the effects of the cubic crystal field on the Hund's rule ground state and therefore can be viewed as an effective single particle model.
- A more complete crystal field multiplet model which takes both atomic multiplets as well as the cubic crystal field into account.

The molecular orbital model can be described with two parameters, the cubic crystal field strength (10Dq or $\mathcal{D}$) and an effective exchange splitting $\mathcal{K}$ which gives the energy gain of two parallel spins. Henceforth this model is called the $\mathcal{DK}$-model; it allows for a direct qualitative assignment of the peaks in the observed oxygen $1s$ x-ray absorption spectra. In the crystal field multiplet model the atomic symmetries are projected to cubic symmetry. Table 3.4 gives the projection rules for cubic symmetry.

Spherical	Cubic
S	A_1
P	T_1
D	$E + T_2$
F	$A_2 + T_1 + T_2$
G	$A_1 + T_1 + T_2 + E$
H	$T_1 + T_1 + T_2 + E$
I	$A_1 + A_2 + T_1 + T_1 + T_2 + E$

Table 3.4: The $SO_3 \rightarrow O_h$ Branching rules in the Schönflies notation.

The $3d^0$ to $3d^3$ configurations

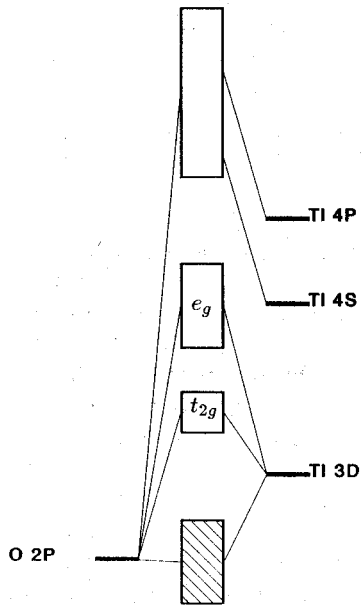

Figure 3.6: Schematic N-particle density of states of TiO_2, based on a molecular orbital description. The oxygen $2p$-band is filled and the empty $3d$-band is split into a t_{2g} and an e_g sub-band.

A system with a $3d^0$ configuration, like TiO_2 or CaF_2, has an electronic configuration with only completely filled or completely empty bands. Figure 3.6 sketches a simplified density of states picture of a $3d^0$ compound. The narrow $3d$-band is situated in between the filled

oxygen $2p$-band and the empty metal $4sp$ band. The $3d$-band is split in two and the t_{2g} sub-band is positioned at lower energy and is considerably sharper (less interaction) than the e_g sub-band. The filled oxygen $2p$-band contains a considerable amount of metal $3d$-character and correspondingly the empty $3d$-band contains states of oxygen $2p$-character. For example the band structure calculation of $SrTiO_3$ yields a titanium $3d$ occupation of 1.5 electrons (see section 3.8). The electron addition spectrum of a $3d^0$ compound shows respectively a t_{2g}-peak, an e_g-peak and a structure related to the $4sp$-band. In the final state there is only one electron in the $3d$-band, hence no multipole correlation effects.

A $3d^1$ configuration has a ground state of ${}^2T_2$-symmetry and the electron addition spectrum (in the $\mathcal{DK}$-model) contains four peaks related to the filling of respectively a t_{2g}^+, t_{2g}^-, e_g^+ or e_g^- orbital. The splitting between the t_{2g}^+ and the e_g^+ state is equal to the cubic crystal field strength ($\mathcal{D}$), and the splitting between the t_{2g}^+ and the t_{2g}^- state is equal to $\mathcal{K}$. The exchange interactions are slightly different for respectively t_{2g} and e_g electrons. The exchange interactions are taken from Ref. 83 and a calculation for the atomic Slater integrals of Mn^{IV} shows that $\mathcal{K}_{ee} \approx 1.05$ eV, $\mathcal{K}_{tt} \approx 0.92$ eV and $\mathcal{K}_{et} \approx 0.79$ eV. For trivalent and divalent manganese the values are slightly lower. Figure 3.7 sketches the energy situation (in the final state) of a $3d^1$ ground state.

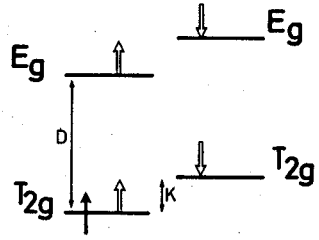

Figure 3.7: The $\mathcal{DK}$-model for a $3d^1$-configuration

In the crystal field multiplet model the electron addition spectrum consists of all atomic multiplets split by the cubic crystal field: the ${}^3F$-state splits into ${}^3T_1$, ${}^3T_2$ and ${}^3A_2$, the ${}^3P$-state to ${}^3T_1$. The energy positions are determined by the Slater integrals and the cubic crystal field. The difference between the models is that the $\mathcal{DK}$-model effectively neglects the Slater integrals apart from the energy difference between singlet and triplet states and as a consequence only states are considered which contain at least one t_{2g}^+ electron, as other states do not couple to the ground state under neglect of the Slater integrals. A $3d^2$-configuration contains two (t_{2g}^+) electrons and its symmetry is ${}^3T_1$. That is the ${}^3F$ ground state splits in three (${}^3T_1$, ${}^3T_2$ and ${}^3A_2$), of which ${}^3T_1$ has the lowest energy. As the ${}^3P$-state also projects onto a ${}^3T_1$-state, the actual ${}^3T_1$ ground state is a combination of the two states of this character [12]. Figure 3.8 shows the effect of increasing cubic crystal field, the so-called Tanabe-Sugano diagram, for $3d^2$. Electron addition in the $\mathcal{DK}$-model gives four peaks at the energies 0, $\mathcal{D}$, $2\mathcal{K}$ and $\mathcal{D} + 2\mathcal{K}$. For $\mathcal{K}$ the value for $\mathcal{K}_{te}$ are used. In the crystal field multiplet model the electron addition states relate again to all $3d^3$ states, which can couple to the ground state of the $3d^2$-state with the addition of a $3d$-electron. A $3d^3$-configuration contains three (t_{2g}^+) electrons which form a ground state of ${}^4A_2$-symmetry. Electron addition in the $\mathcal{DK}$-model gives only three peaks as the t_{2g}^+-state is full.

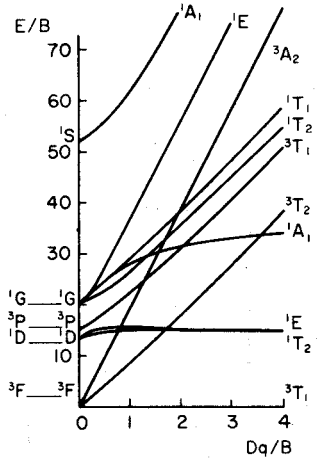

Figure 3.8: Tanabe Sugano diagram for a $3d^2$ ground state in cubic symmetry. Taken from Ref. 44.

High-spin versus low-spin

If four electrons have to be accommodated in the five $3d$-orbitals in an octahedral surrounding, two different situations can occur. If $3\mathcal{K}_{(te)} > \mathcal{D}$, a high spin $(t_{2g}^+)^3(e_g^+)^1$-configuration with ^5E-symmetry is formed from the Hund's rule ^5D ground state. If however $3\mathcal{K} < \mathcal{D}$, a low spin $(t_{2g}^+)^3(t_{2g}^-)^1$-configuration with $^3T_1$-symmetry, originating from five atomic triplet states, is formed [44,12]. Figure 3.9 sketches the addition of an electron to respectively the high-spin and the low-spin ground state. In case of low-spin the addition of an electron in the e_g^+-band costs $\mathcal{D}$ but one gains $3\mathcal{K}_{te}$; with the addition of an electron in the t_{2g}^--band one gains $\mathcal{K}_{tt}$. The e_g^+-band is positioned at an energy $\mathcal{D}$ above the t_{2g}^+-band and the relative energy of the t_{2g}^--band is - $\mathcal{D}$ + $3\mathcal{K}_{te}$ - $\mathcal{K}_{tt}$. This places the t_{2g}^--band at an energy $3\mathcal{K}_{te}$ - $\mathcal{K}_{tt}$ above the t_{2g}^+-band. Because the energy difference between $\mathcal{K}_{te}$ and $\mathcal{K}_{tt}$ is only 0.1 eV it is neglected, and the expression for the relative energy of the t_{2g}^--band reduces to $2\mathcal{K}$ as given in the figure. To simplify the discussion the difference between $\mathcal{K}_{te}$ and $\mathcal{K}_{tt}$ is neglected in the following sections. If the t_{2g}^--level and the e_g^+-level are close to degenerate, they give rise to an intermediate spin state if $3d$ spin-orbit coupling is included [75] (see section 3.5). For $3d^5$, $3d^6$ and $3d^7$ ground states the high-spin versus low-spin dichotomy exist. Table 3.5 gives the respective configurations, symmetries and electron addition states (in the $\mathcal{DK}$-model).

Table 3.5 shows that for $3d^5$ to $3d^7$ the high-spin states consist only of two electron addition states, split by $\mathcal{D}$, as only spin-down electrons can be added. The low-spin $3d^6$ has only one electron addition state as the e_g^+ and e_g^- states are exactly degenerate because of the singlet ground state. Because the number of final states is limited the electron addition states of $3d_{HS}^7$ are a good example to show the actual difference between the $\mathcal{DK}$-model and the crystal field multiplet model. The ground state has $^4T_1$-symmetry, thus the electron addition $3d^8$-states must be triplet states. In the atomic $3d^8$ multiplet there are only two triplet states: ^3F and ^3P. In the $\mathcal{DK}$-model there are also only two available states:

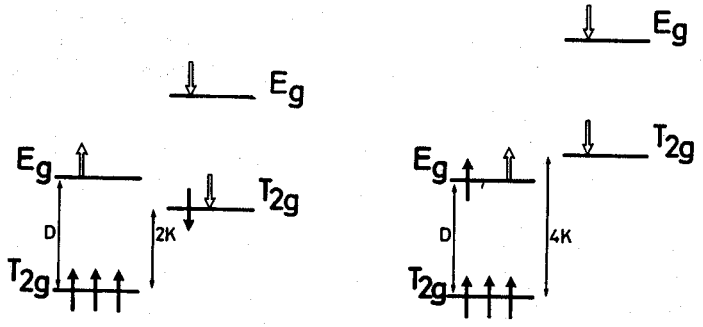

Figure 3.9: The $\mathcal{DK}$-model for a $3d^4$-configuration: (left) low spin; (right) high-spin. The energy difference between $\mathcal{K}_{te}$ and $\mathcal{K}_{tt}$ has been neglected.

state	configuration	symmetry	energy of one electron addition		
$3d^4_{HS}$	$(t^+_{2g})^3(e^+_g)^1$	^5E	$\mathcal{D}$	$4\mathcal{K}$	$\mathcal{D}+4\mathcal{K}$
$3d^4_{LS}$	$(t^+_{2g})^3(t^-_{2g})^1$	$^3A_2$	$\mathcal{D}$	$2\mathcal{K}$	$\mathcal{D}+2\mathcal{K}$
$3d^5_{HS}$	$(t^+_{2g})^3(e^+_g)^2$	$^6A_1$	$5\mathcal{K}$	$\mathcal{D}+5\mathcal{K}$	
$3d^5_{LS}$	$(t^+_{2g})^3(t^-_{2g})^2$	$^2T_2$	$\mathcal{D}$	$\mathcal{K}$	$\mathcal{D}+\mathcal{K}$
$3d^6_{HS}$	$(t^+_{2g})^3(e^+_g)^2(t^-_{2g})^1$	$^5T_2$	$4\mathcal{K}$	$\mathcal{D}+4\mathcal{K}$	
$3d^6_{LS}$	$(t^+_{2g})^3(t^-_{2g})^3$	$^1A_1$	$\mathcal{D}$		
$3d^7_{HS}$	$(t^+_{2g})^3(e^+_g)^2(t^-_{2g})^2$	$^4T_1$	$3\mathcal{K}$	$\mathcal{D}+3\mathcal{K}$	
$3d^7_{LS}$	$(t^+_{2g})^3(t^-_{2g})^3(e^+_g)^1$	^2E	$\mathcal{D}$	$\mathcal{D}+\mathcal{K}$	

Table 3.5: Symmetries of the $3d^N$ ground state configurations and the 'electron addition states' in the $\mathcal{DK}$-model.

$(t^+_{2g})^3(e^+_g)^2(t^-_{2g})^3$ and $(t^+_{2g})^3(e^+_g)^2(t^-_{2g})^2(e^-_g)^1$, or in hole notation $(\underline{e}^-_g)^2$ and $(\underline{e}^-_g)(\underline{t}^-_{2g})$ or simply $\underline{ee}$ and $\underline{et}$. The atomic multiplet model takes into account the Slater integrals only, whereas the $\mathcal{DK}$-model allows for one electron addition only. The crystal field multiplet model allows for multi-electron transitions to the whole crystal field multiplet and figure 3.10 sketches the transition from the atomic multiplet (in LS-coupling) to the one electron addition model for a cubic crystal field.

The ^3F state splits into states of $^3A_2$, $^3T_2$ and $^3T_1$ symmetry and the ^3P state transforms to $^3T_1$ symmetry. Increasing the cubic crystal field (divided by the Slater integrals) trans-

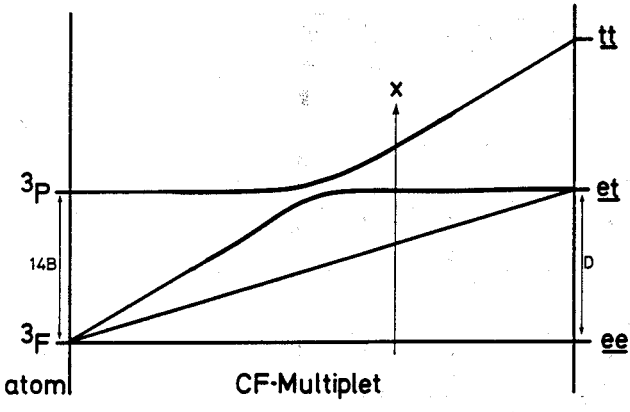

Figure 3.10: Transformation between the states in an atomic multiplet (right) and one electron $\mathcal{DK}$-model (left). The crystal field multiplet model refers to a situation in between these extremes. For the $\mathcal{DK}$-model the $\underline{tt}$ state has zero intensity as it cannot be reached by one electron addition to the $(t_{2g}^+)^3(e_g^+)^2(t_{2g}^-)^2$ ground state.

forms the ${}^3A_2$-state to the pure $\underline{ee}$-state and the ${}^3T_2$-state to the $\underline{et}$-state. The situation for the ${}^3T_1$-state is more complicated as there are two states of the same symmetry. The ${}^3T_1$ state originating from the ${}^3P$ atomic state has to transform to the $\underline{et}$-state, whereas the ${}^3T_1$ state originating from the ${}^3F$ atomic state has to transform to the $\underline{tt}$-state, i.e. the overall atomic states are spherical symmetric (${}^3F \rightarrow \underline{ee} + \underline{et} + \underline{tt}$ and ${}^3P \rightarrow \underline{et}$). From figure 3.10 it can be seen that the ${}^3T_1$-like states tend to cross, which is forbidden as they have the same symmetry. Therefore the two ${}^3T_1$-states repel each other; both states have strongly mixed atomic ${}^3P$ plus ${}^3F$ states, or alternatively strongly mixed $\underline{te}$ plus $\underline{tt}$ crystal field character. The pure $\underline{tt}$ state does not couple to the ground state and therefore in the $\mathcal{DK}$-model only two states can be reached. The crystal field multiplet model has four allowed states. In table 3.6 the number of states is given for the atomic multiplet, the crystal field multiplet (without core hole) and the $\mathcal{DK}$-model for all $3d^N$-configurations. In case of a ground state with A_1-symmetry the number of final states is relatively small, because only T_2 and E states can be reached. Because the ${}^6A_1$-state only the quintet states can be reached, only two states is found in the crystal field multiplet.

3.2.3. Core hole effect on the crystal field multiplet

A central phenomena of the x-ray absorption process is the creation of a core hole. In the final state the core hole gives rise to additional interactions, as discussed for the atomic case. If the valence electrons are described by a crystal field multiplet similar effects occur. The dominant effect of the core hole is that the symmetries of the valence band crystal field multiplet have to be multiplied with the spin-orbit split ${}^2P_{3/2}$ and ${}^2P_{1/2}$-symmetries of the core hole. This gives rise to two distinct multiplets related to the L_3 and the L_2 edge. As discussed before additional core hole effects occur due to considerable overlap of the $2p$ and $3d$ wavefunctions. Because of this the existence of a $2p$ core hole gives rise to strong correlations with $3d$ electrons, and the multipole F_{pd}^2 and the (multipole) exchange G_{pd}^1 and G_{pd}^1 Slater integrals cause a drastic reordering of the crystal field multiplet. Therefore it is

state	symmetry	atom	CFM	$\mathcal{DK}$
$3d^1$	$^2T_2$	5	16	4
$3d^2$	$^3T_1$	8	32	4
$3d^3$	$^4A_2$	7	10	3
$3d^4_{HS}$	^5E	5	11	3
$3d^4_{LS}$	$^3T_1$	15	20	3
$3d^5_{HS}$	$^6A_1$	1	2	2
$3d^5_{LS}$	$^2T_2$	14	36	3
$3d^6_{HS}$	$^5T_2$	2	3	2
$3d^6_{LS}$	$^1A_1$	6	9	1
$3d^7_{HS}$	$^4T_1$	2	4	2
$3d^7_{LS}$	^2E	5	11	2
$3d^8$	$^3A_2$	1	1	1
$3d^9$	^2E	1	1	1

Table 3.6: Comparison of the number of states in the crystal field multiplet model (CFM) as compared with the DK-model and the atomic multiplet.

more appropriate to discuss the complete $2p$ crystal field multiplet at once in an intermediate coupling scheme. The crystal field multiplet program as developed by B.T. Thole takes all interactions within the $2p^5 3d^{N+1}$ final state into account simultaneously. The symmetries of the atomic states, calculated with an atomic multiplet program, are projected according to the branching rules [53]. The papers included in the sections 3.3 and 3.4 give the actual effects of the cubic crystal field on the spectral shape of the atomic multiplets of a series of $3d$-metal ions. Section 3.5 discusses the low-energy splittings originating from the $3d$ spin-orbit coupling and non-cubic crystal fields and section 3.6 deals with the effects of polarization dependence. The limitations of the model are discussed in section 3.7.

3.3. Metal 2p x-ray absorption of $3d^0$ compounds

Reproduced from *Physical Review B.*, volume **41**, page 928-937 (1990).

This paper contains the crystal field multiplet calculations for compounds with an empty $3d$-band. The crystal field multiplets of the $3d^0 \rightarrow 2p^5 3d^1$ transition are calculated. The effects of the cubic crystal field on the theoretical spectral shape is studied in detail. The theoretical results are compared with $2p$ x-ray absorption spectra of $FeTiO_3$, TiO_2, Sc_2O_3, ScF_3, CaF_2 and the potassium halides. The peaks in the experimental spectra can be related to single final states of the crystal field multiplet. This makes it possible to measure the broadening of the individual transitions in the $3d^0 \rightarrow 2p^5 3d^1$ multiplet. The origins of the different mechanisms for the symmetry dependent broadening effects are discussed.

$L_{2,3}$ x-ray-absorption edges of d^0 compounds: K^+, Ca^{2+}, Sc^{3+}, and Ti^{4+} in O_h (octahedral) symmetry

F. M. F. de Groot and J. C. Fuggle
Research Institute for Materials, University of Nijmegen, Toernooiveld, 6525 ED Nijmegen, The Netherlands

B. T. Thole and G. A. Sawatzky
Materials Science Centre, University of Groningen, Nijenborgh 18, Paddepoel, 9747 AG Groningen, The Netherlands

(Received 17 July 1989)

The $L_{2,3}$ x-ray-absorption edges of $3d^0$ compounds are calculated with use of an atomic description of the $2p^6 3d^0$ to $2p^5 3d^1$ excitation, with the inclusion of the crystal field. For reasons of clarity, we confine ourselves to d^0 compounds in octahedral symmetry, but the same approach is applicable to all other d^N compounds in any point-group symmetry. The experimental spectra of $FeTiO_3$, Sc_2O_3, ScF_3, CaF_2, and the potassium halides are well reproduced by the present calculations, including the previously misinterpreted small leading peaks. The splitting between the two main peaks in both the L_3 and L_2 edge are related, though not equal, to the crystal-field splitting. Comparison to experiment showed that the broadening of the main multiplet lines is different. This can be related to Coster-Kronig Auger processes for the L_2 edge and to a solid-state broadening which is a combination of vibrational (phononic) and dispersional broadenings. With the full treatment of the atomic multiplets, the atomic effects can be separated from solid-state effects, which offers a better description of the latter. This includes vibrational broadenings, the covalent screening of the intra-atomic Coulomb and exchange interactions, via the position of small leading peaks, and surface effects. The same general framework can be used to discuss crystal-field effects in both lower symmetries, with the possibility of polarization-dependent spectra (e.g., TiO_2), and partly filled d bands.

I. INTRODUCTION

In the past few years experimental progress in the field of soft-x-ray absorption has been tremendous. The attainable experimental resolution has improved to its present best value of 30 meV at 300 eV.[1,2] This technical progress has opened the possibility to measure the transition metal $L_{2,3}$ x-ray-absorption edges, including also K and Ca, with great accuracy.[3]

Theoretical developments have lagged behind those of experiment but the improvement in resolution has created the need for a much more advanced description. In this paper we contribute to a description of the transition metal $L_{2,3}$ x-ray-absorption spectra.[4] The starting point is an atomic multiplet calculation.[5–7] We then treat those cases where the most prominent effect of the solid state is the crystal field, the breaking of the spherical symmetry around the atom. We prefer to use the term crystal field rather than ligand field, because in principle we only change the point-group symmetry. The crystal field is put in as a parameter fit to the experiment. In this manner the hybridization effect of the ligands is implicitly taken into account. Dispersional effects, which have been treated earlier for the elemental transition metals,[8,9] are not taken explicitly into account here.

Using group-theory formalism,[10–12] it is possible to project the atomic spectrum (spherical symmetry) onto a specific symmetry group. All point-group symmetries can be addressed in this way. However, the lower the symmetry, the more parameters are needed to account for all possible interactions. In this paper we only consider O_h symmetry, which accounts for both sixfold (octahedral) and eightfold (simple-cubic) surroundings. We will show that with the restriction to O_h symmetry we are already able to obtain excellent results, even for some cases in which the actual symmetry is lower. To limit the complexity of the theory presented, we postpone the discussion of lower symmetries.

We start with an outline of the theoretical approach (Sec. II). In Sec. III we will present some general results for the d^0 compounds, where we take Ti^{4+} as an example. We show that the splittings in the x-ray-absorption spectroscopy (XAS) spectrum are due to, but do not directly scale with, the crystal-field parameter $10Dq$. In Sec. IV we will make a comparison to experimental results of K^+, Ca^{2+}, Sc^{3+}, and Ti^{4+} compounds.

II. THEORY

We calculated the excitation from the d^0 ground state to the final-state $2p^5 3d^1$ multiplet by means of an optical dipole transition. The central point in our analysis will be the crystal field. First it is necessary, however, to calculate the atomic multiplet.

A. Atomic multiplet theory

For reasons of clarity we will briefly repeat atomic multiplet theory as can be found in the standard text-

books.[13,14] The Hamiltonian for atomic multiplets can be written as

$$H = H_{\text{av}} + \mathbf{L}\cdot\mathbf{S}(p) + \mathbf{L}\cdot\mathbf{S}(d) + g(i,j) .$$

H_{av} consists of the kinetic term and the interaction with the nuclei. It gives the average energy of the multiplet and does not contribute to the multiplet splittings. The splittings in the multiplet are caused by the spin-orbit couplings, $\mathbf{L}\cdot\mathbf{S}$, for the $2p$ and $3d$ electron, and by the Coulomb repulsion term, $g(i,j)$. This two-electron operator can be expressed in terms of spherical harmonics,[13] which necessitates the division of radial and angular parts. The radial part, $R^K(l_1 l_2; l_3 l_4)$ is divided in direct Coulomb terms, $F^K(l_1 l_2; l_1 l_2)$, and exchange terms, $G^K(l_1 l_2; l_2 l_1)$. The angular part of $g(i,j)$ results in the selection rules, or in other words it gives the possible K values. For the direct Coulomb term, no odd K values are allowed, and the maximum K value is two times the minimal l value. For the p^5d^1 multiplet this results in F^0 and F^2, while for a d^2 multiplet F^4 also comes into play. The K values in the exchange term equal $|l_1 - l_2|$, $|l_1 - l_2 + 2k|, \ldots, l_1 + l_2$. For the p^5d^1 multiplet this results in G^1 and G^3. Thus we can evaluate the two-electron operator $g(i,j)$ for the p^5d^1 multiplet in terms of four interactions: F^0, F^2, G^1, and G^3. F^0 only contributes to the average energy and is taken into H_{av}. The *ab initio* calculated Coulomb, exchange and spin-orbit parameters (F^2, G^1, G^3, $\mathbf{L}\cdot\mathbf{S}_p$, and $\mathbf{L}\cdot\mathbf{S}_d$) of K^+, Ca^{2+}, Sc^{3+}, and Ti^{4+} are given in Table I. For the actual crystal-field calculations, the *ab initio* (Hartree-Fock) values of F^2, G^1, and G^3 are scaled down to 80% of their original value to account for many-body corrections.[15]

B. The atomic excitation from $2p^63d^0$ to $2p^53d^1$

The ground state d^0 consists of one single ^1S state. Therefore with x-ray absorption, following the optical transition selection rule, only the ^1P final state is within reach in LS coupling, thus only one peak would appear in the XAS spectrum. Turning on the spin-orbit coupling of the $2p$ core hole, but still neglecting the spin-orbit coupling of the $3d$ electron and the Coulomb repulsion term, $g(i,j)$, leads to the well-known approximation of two peaks with an intensity ratio of 1:2, denoted by the L_3 and L_2 edge. This is caused by the transformation from LS to jj coupling which results in the mapping of ^1P (LS) onto ^1P, ^3P, and ^3D (jj), of which both triplet states have equal energy.[8] As is directly evident from the values of Table I, the direct Coulomb and exchange terms F^2, G^1, and G^3 are not negligible. The result is a splitting of the L_3 edge and consequently three absorption lines. The intensities of these lines are also strongly redistributed by F^2, G^1, and G^3. Figure 1 gives only the result for Ti^{4+} as the atomic spectra for K^+, Ca^{2+}, and Sc^{3+} are similar. The small leading peak has predominantly triplet character and is mixed through the spin-orbit interaction and the Coulomb repulsion into the main L_3 edge. This small leading peak retains its intensity when the crystal field is considered and will give rise to a general small leading peak in x-ray-absorption spectra of d^0 compounds. We stress this atomic multiplet feature as it has been overlooked in some x-ray-absorption literature.

C. Crystal-field effect on the $2p^53d^1$ multiplet

We now consider the crystal field. In terms of group theory the effect of an octahedral crystal field is the reduction of symmetry from O_3 to O_h. All irreducible representations (henceforth referred to as IR) in spherical symmetry are projected onto the O_h group. We have to consider separately (1) the ground state IR, (2) the final state IR's, and (3) the transition IR.

Using jj coupling in O_3 symmetry, there exists one IR per J value, with a degeneracy of $2J+1$. The d^0 ground state has a J value of 0, and the transition has a J value of 1. The accessible final states are thus restricted to those with a J value of 1. The 60 possible states of the p^5d^1 multiplet are distributed over five IR's with J values of 0, 1, 2, 3, and 4, and with degeneracies of, respectively, 1, 3, 4, 3, and 1. Notice that in LS coupling the p^5d^1 multiplet has six IR's: singlet and triplet F, D, and P.

We have to transform these O_3 IR's to O_h symmetry, where there are five possible IR's. Their standard notation is A_1, A_2 (one-dimensional), E (two-dimensional), T_1, and T_2 (Ref. 14) (three-dimensional). The transformation from O_3 to its subgroup O_h, mostly called the O_3-O_h branching, can be found in the work of Butler.[10]

TABLE I. Values for the atomic multiplet, from an *ab initio* calculation. E_{av} gives the average energy of the multiplet and $\mathbf{L}\cdot\mathbf{S}$ gives the parameters for the spin-orbit coupling. The *ab initio* value of the Coulomb and exchange parameters or Slater integrals F^2, G^1, and G^3 are given; they are normalized to 80% of their *ab initio* value in the real calculation, to simulate configuration interaction.

Ion	K^+	Ca^{2+}	Sc^{3+}	Ti^{4+}
E_{av}	298.40	350.37	405.75	464.81
$\mathbf{L}\cdot\mathbf{S}(p)$	1.88	2.4	3.03	3.78
$\mathbf{L}\cdot\mathbf{S}(d)$	0.005	0.011	0.020	0.032
F^2_{pd}	2.20	3.79	5.09	6.30
G^1_{pd}	1.32	2.51	3.58	4.62
G^3_{pd}	0.74	1.42	2.03	2.63

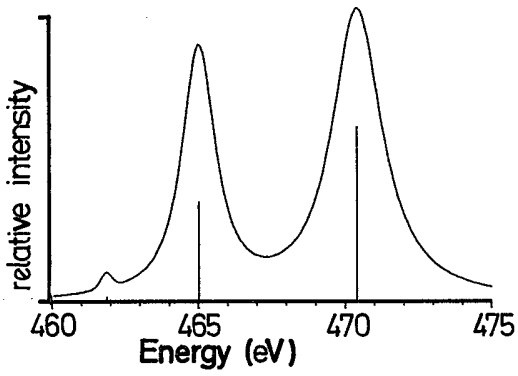

FIG. 1. Atomic multiplet spectrum for the $3d^0$ to $2p^53d^1$ excitation of Ti^{4+}; the Slater integrals are reduced to 80% of their Hartree-Fock values.

TABLE II. The branching table from O_3 to O_h is given for integer values of J in O_3 (as occur for the p^5d^1 multiplet). See Butler for more details and all other branching tables.

O_3	→	O_h
$J=0$	→	A_1
$J=1$	→	T_1
$J=2$	→	$E+T_2$
$J=3$	→	$T_1+T_2+A_2$
$J=4$	→	$A_1+T_1+E+T_2$

The essential details are repeated in Table II.

The ground state and the transition IR are transformed to, respectively, A_1 and T_1. The entire effect of the crystal field to split and shift the peaks in the spectrum is thus concentrated in the final state. All possible final states must have T_1 symmetry, otherwise the transition matrix element equals zero. The T_1 IR can be reached not only from the $J=1$ IR, but also from the $J=3$ and $J=4$ IR's (see Table II). The $J=1$ and $J=3$ IR's are both threefold degenerate and the $J=4$ IR is nondegenerate. This results in seven possible T_1 IR's in O_h symmetry, or, in other words, seven possible final states. The XAS spectrum consists, in principle, of seven lines, as can be seen in Fig. 2, where the Ti^{4+} XAS spectrum for a crystal-field splitting ($10Dq$) of 1.8 eV is calculated.

D. Generality of the method

The method used starts with the calculation of the atomic (initial and final) multiplets. The Slater integrals (F^2, G^1, and G^3) are scaled down to 80% of their *ab initio* values. Then the reduced matrix elements of all necessary operators in the spherical group are calculated with the use of Cowan's atomic multiplet program.[7] To obtain the reduced matrix elements in any point group, Butler's program is used for the calculation of all necessary factors ($3J$ symbols). With this general approach, the program is, in principle, capable of calculating the transition probabilities between any two configurations in XAS, x-ray photoemission spectroscopy (XPS), or bremsstrahlung isochromat spectroscopy (BIS) in all point-group symmetries.[7,16]

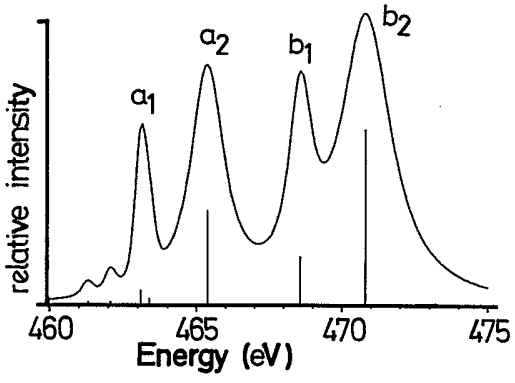

FIG. 2. Multiplet spectrum for the $3d^0$ to $2p^53d^1$ excitation of Ti^{4+} in octahedral symmetry; the crystal-field parameter $10Dq$ was taken as 1.8 eV. The 80% reduction of the Hartree-Fock values was used.

This means that for the $L_{2,3}$ XAS edges any transition from a d^N ground state to a p^5d^{N+1} final state can be calculated. The number of final states increases drastically if $N>0$. Also, ground-state crystal-field effects become important, which complicates the analysis. We have calculated the complete d^N series in O_h symmetry, which will be published elsewhere.[17] The calculation of lower symmetries, using the necessary branchings, means that the number of parameters increases. For example, O_h needs only one parameter while D_{4h} needs three, which makes the analysis more difficult. Another important effect of lower symmetries such as D_{4h} is the polarization dependence of the spectrum. The possibility to use lower symmetries to correctly describe x-ray-absorption spectra was used for rutile TiO_2.[18]

III. RESULTS FOR d^0 COMPOUNDS

Experimentally it is found that the crystal field splits the L_3 and L_2 x-ray-absorption edges. Often this is pictured as a splitting of both edges into two, with the energy difference between both peaks assumed equal to the crystal-field parameter $10Dq$. Using the crystal-field program we have calculated the p^5d^1 multiplet for a number of $10Dq$ values. Figure 3 gives the results for Ti^{4+} using both positive and negative values, related to, respectively, sixfold (octahedral) and eightfold (simple-cubic) surroundings. The crystal field has to compete with all intra-atomic interactions [F^2, G^1, G^3, $\mathbf{L}\cdot\mathbf{S}(p)$, and $\mathbf{L}\cdot\mathbf{S}(d)$]. The result is a complex change of the spectrum as a function of $10Dq$. The value of the crystal-field splitting is indicated as the distance between the vertical line and the diagonal. In Fig. 4 the distance between the two main peaks in the L_3 (peak a_1 and a_2) and L_2 (peak b_1 and b_2) edge is given as a function of the crystal field. The result is evident: *The energy splitting in the XAS spectra, is, in general, not equal to 10Dq.*

Starting with the atomic calculation (Fig. 4, $10Dq=0$) and turning on a small crystal field, a small energy splitting immediately appears. This does not mean that the atomic lines are split in two, but that other final states are mixed in. These states were not accessible in spherical symmetry as discussed in Sec. II. The intensities of these new transitions (opened channels for O_h) are small for low crystal fields as can be seen in Fig. 5.

The following picture then emerges: In O_h symmetry the p^5d^1 multiplet consists of seven lines, four of which are forbidden in spherical symmetry. The crystal field has the effect of (1) shifting the seven final states in energy (see Figs. 3 and 6) and (2) redistributing the absorption intensity over all seven lines (see Fig. 5).

The crystal field has a slightly different, though equivalent, effect on the L_3 edge, compared to the L_2 edge. This small difference between the L_3 and L_2 edge can also be seen in the experimental spectra, but this was not extensively discussed until now. With the present improvement in resolution,[2] it is possible to show the ine-

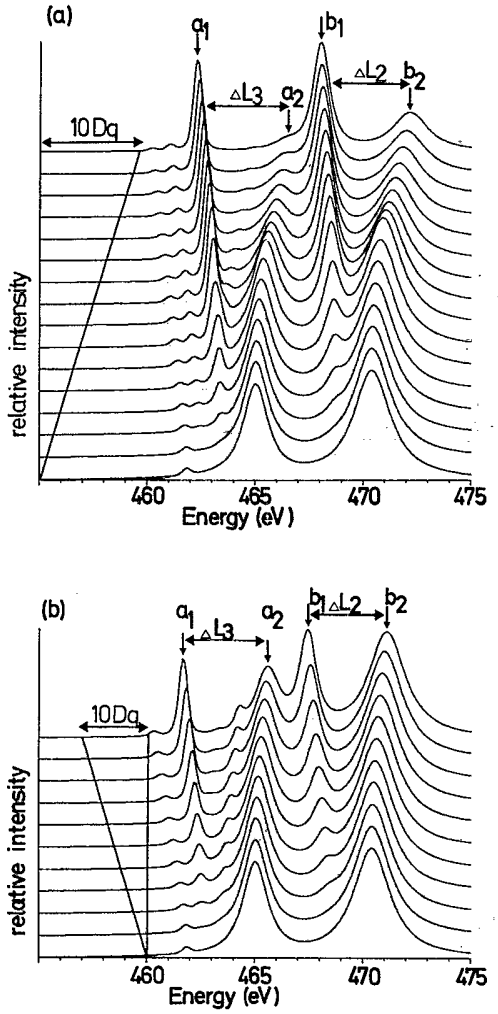

FIG. 3. Ti^{4+} $2p^5 3d^1$ excitation spectra in O_h symmetry as a function of the crystal-field splitting $10Dq$. (a) The value of $10Dq$ is positive and ranges from 0.0 to 4.5 eV, indicated by the diagonal line; (b) the value of $10Dq$ is negative. ΔL_3 measures the distance between the peaks a_1 and a_2, split by the crystal field.

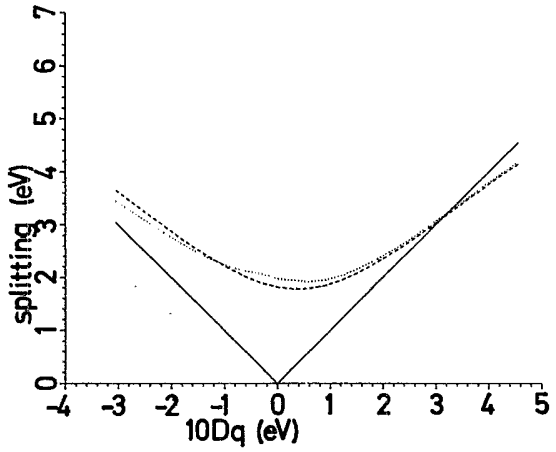

FIG. 4. The splitting between peaks a_1 and a_2 (ΔL_3, dashed line) and between peaks b_1 and b_2 (ΔL_2, dotted line) is given as a function of the crystal-field parameter $10Dq$. For the solid line, the assumption of a splitting equal to $10Dq$ is made.

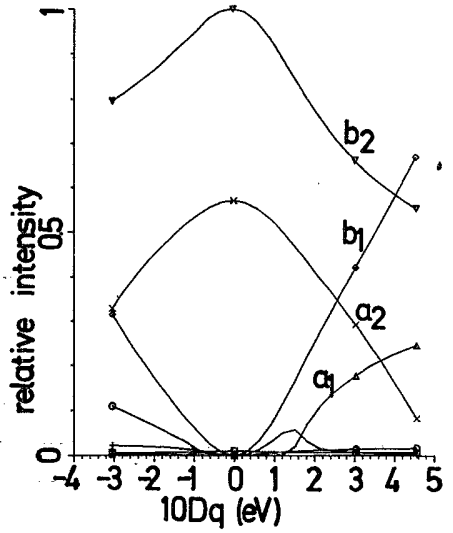

FIG. 5. For Ti^{4+} in O_h symmetry the changes in intensity are given as a function of the crystal-field splitting $10Dq$. The symbols correspond to the seven absorption lines ordered for increasing energy (see Fig. 6).

quivalence of peak separations in the L_2 and L_3 peaks convincingly. The clearest case is CaF_2 (see Sec. IV C).

IV. COMPARISON WITH EXPERIMENT

We compare our results for the $2p^5 3d^1$ optical transition multiplet with x-ray-absorption spectra for K^+, Ca^{2+}, Sc^{3+}, and Ti^{4+} compounds. We start with Ti^{4+} in ilmenite, $FeTiO_3$ (Sec. IV A). A comparison to the Sc^{3+} compounds Sc_2O_3 and ScF_3 is given in Sec. IV B. The

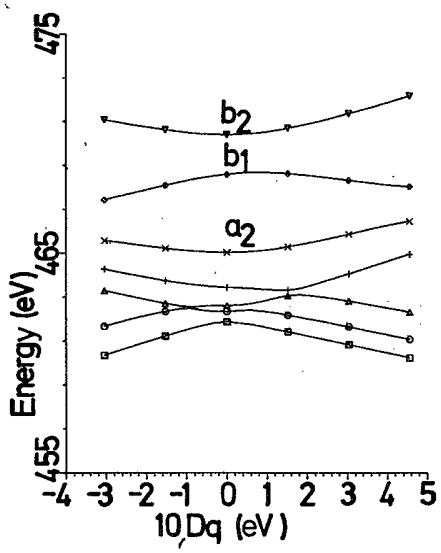

FIG. 6. For Ti^{4+} in O_h symmetry the changes in energy position are given as a function of the crystal-field splitting $10Dq$. The symbols correspond to the seven absorption lines ordered for increasing energy.

scandium compounds show well separated peaks, from which we can show that it is possible to make more accurate comparisons with the exact position of the small leading peaks. Section IV C deals with CaF_2, whose (bulk) spectrum is completely reproduced. We end with a comparison with a series of potassium-halide K $L_{2,3}$ edges,[19] which will be discussed in Sec. IV D.

A. The Ti $L_{2,3}$ XAS spectrum of $FeTiO_3$

We have compared the titanium $L_{2,3}$ edge of $FeTiO_3$ with the calculation of Ti^{4+} in O_h symmetry. The exact structure of $FeTiO_3$ (see Table V) (Refs. 20 and 21) and the resulting point group of Ti^{4+} are not critical for our analysis. Figure 7 gives the $FeTiO_3$ spectrum compared with the calculation in O_h symmetry, which shows good agreement and justifies the approximation of octahedrally surrounded Ti^{4+} ions. Although we will not discuss the theoretical Ti^{3+} spectrum we calculated, we note that the experimental Ti $L_{2,3}$ XAS spectrum of $FeTiO_3$ is only consistent with Ti^{4+}, not Ti^{3+}.[22]

To obtain the optimum agreement with experiment, it is necessary to choose different Lorentzian broadenings for the four peaks. The optimum values for the broadening are given in Table III. After the Lorentzian broadening the whole spectrum was convoluted with a Gaussian broadening of 0.15 eV (Ref. 23) to simulate the experimental resolution. From this choice of broadenings and from the resulting agreement with experiment, *it is clear that each peak in the $L_{2,3}$ XAS spectrum has its own characteristic broadening.* Noticing this we will try to find the underlying reasons. The extra broadening of the peaks belonging to the L_2 edge (peak b_1 and b_2) originates from the shorter lifetime of the $p_{1/2}$ states. A $p_{1/2}$ state has an extra decay channel, the Coster-Kronig (CK) Auger decay process,[5,24] by which it can fall back to a $p_{3/2}$ hole, with the simultaneous ejection of a d electron. The energy difference between a $2p_{1/2}$ and a $2p_{3/2}$ hole, due to the $(2p)$ spin-orbit coupling, must be larger than the binding energy of the d electron, otherwise the CK Auger channel is closed.

From Table III we conclude that the CK Auger broadening of the L_2 edge (peak a_2 and b_2) is 0.4 eV. Subtracting this broadening,[25] both peaks a_2 and b_2 have an extra broadening of about 0.5 eV with respect to peaks a_1 and b_1. The origin of this broadening could be due to (1) a lifetime effect similar to the L_2 CK Auger decay, (2) an effect of the actual point-group symmetry, (3) vibrational (phononic) broadening, and (4) dispersional

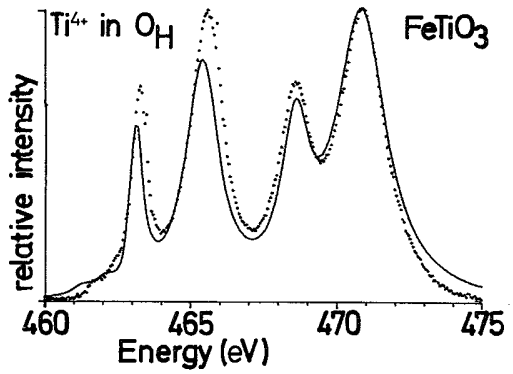

FIG. 7. The experimental $FeTiO_3$ spectrum (dotted), measured with the SX700 monochromator at Berliner Elektronenspeicherring-Gesellschaft für Synchrotronstrahlung m.b.H (BESSY), is compared with a multiplet calculation in O_h symmetry. The crystal-field parameter is 1.8 eV; the broadening factors are tabulated in Table III.

broadening. The possibility of a large broadening effect of a decay process (1) seems unlikely. The energy difference with respect to the lowest main peak is only about 2 eV, which prohibits real Auger decay processes, though virtual processes cannot be excluded. The effect of an actual lower point-group symmetry may be important in the special case of $FeTiO_3$. Because in the other compounds which we will discuss O_h symmetry is better obeyed and their broadenings are equivalent (see Table IV), we do not expect a large extra broadening effect of the reduced symmetry, though in the case of $FeTiO_3$ it may be considerable. In Sec. V we will come back to the possible effect of a lower symmetry and make a connection with the vibrational broadening mechanism. We will now further concentrate on effects (3) and (4), the vibrational and dispersional broadening mechanisms, which can be combined under the heading solid-state broadening.

In a simple picture of a transition metal in octahedral symmetry, the two peaks in both the L_3 and the L_2 edge can be related to t_{2g} (d_{xy}, d_{xz}, and d_{yz} orbitals) and e_g (d_{z2} and d_{x2-y2} orbitals) symmetry.[14] Although in a full atomic multiplet plus crystal-field description this division is not exact, it is a good starting point. In octahedral symmetry e_g orbitals point to the ligands, while t_{2g} orbitals point in between them. This causes the e_g orbitals to bind more strongly to the ligands and conse-

TABLE III. The broadening factors for the $FeTiO_3$ spectrum: The total broadening (Γ) is divided in the Coster-Kronig Auger broadening (α) and the solid-state broadening (β). From the adjustment to experiment it is found that $\alpha=0.4$ eV and $\beta=0.5$ eV (see Fig. 7).

Peak	Total Γ	CK Auger α	Γ-α	Solid state β	Γ-α-β
a_1	0.1 eV		0.1 eV		0.1 eV
a_2	0.6 eV		0.6 eV	0.5 eV	0.1 eV
b_1	0.5 eV	0.4 eV	0.1 eV		0.1 eV
b_2	1.0 eV	0.4 eV	0.6 eV	0.5 eV	0.1 eV

quently to a higher energy of the (antibonding) e_g state, compared to the (antibonding) t_{2g} state. This is in fact the origin of the crystal-field splitting.[14] We can now conclude that, independent of the exact symmetry, the second peak will always be related to a state that has a larger hybridization with the ligands.

Large hybridization, which arises when the states are directed towards the ions, also means that the equilibrium interatomic distances are strongly dependent on occupation of the levels. In x-ray absorption the antibonding levels become occupied, which means that the final-state interatomic distance is larger than the equilibrium ground-state interatomic distance. This is indicated in Fig. 8 [$R^*(e_g) > R\cdot$]. Following the Franck-Condon principle[26] this means a large final-state vibrational broadening (see Fig. 8). For small hybridization (i.e., the t_{2g} orbitals) this Franck-Condon broadening will be smaller. Thus the larger hybridization can cause the extra broadening of the a_2 and b_2 peak. We would also expect a large temperature dependence because of the occupancy of excited vibrational states in the (electronic) ground state. Thermal effects will broaden both the "t_{2g}" and "e_g" states, but the effect on the e_g state will be larger. This thermal broadening more or less scales with the final-state vibrational broadening, which is also present at 0 K [see Fig. 8; compare the energy widths for e_g and t_{2g} at 0 K and at finite temperature (T^*)].

The possibility of dispersional broadening is related to the amount of hybridization. The larger hybridization of the e_g states results in larger bandwidths in the solid state. This dispersion can, however, be reduced or eliminated by excitonic effects due to the large core-hole $3d$ attraction, which localizes the $3d$ electron.[27] The conclusion is that the a_2 and b_2 peaks, because of their larger hybridization, can have stronger vibrational broadening and possibly also stronger dispersional broadening. We do not see a possibility to separate these two broadening mechanisms. Therefore we would like to denote the experimentally found broadening of the e_g peaks in general as a solid-state broadening. This solid-state broadening is found to be 0.5 eV in $FeTiO_3$ (see Table III). From the discussion of the potassium-halide spectra (Sec. IV D), vibrational broadening is found to be the major broadening mechanism.

The analysis procedure of the $FeTiO_3$ $L_{2,3}$ XAS spectrum can be generalized in the following way: First measure the experimental splittings between the a_1 and a_2 peak (ΔL_3) and between the b_1 and b_2 peak (ΔL_2). The splittings found can be related to the value of $10Dq$ with use of the theoretical ΔL versus $10Dq$ lines as given in Fig. 4. With the observed $10Dq$ value, the spectrum can be simulated and from a comparison with the experimental spectrum the exact broadening factors are found.

Although we will not discuss other symmetries in detail, it is interesting to see what happens for a strongly distorted system, such as rutile TiO_2.[28] The strong distortion makes it impossible to simulate its XAS spectrum with the Ti^{4+} p^5d^1 multiplet in O_h symmetry. If the symmetry is reduced to D_{4h}, however, good agreement with experiment can be reached (see Fig. 9).[29] We have used the same range of broadenings as found for $FeTiO_3$. In D_{4h} symmetry the p^5d^1 multiplet consists of 22 lines (seven in O_h). Also one has to consider three crystal-field parameters (only one in O_h) and the polarization dependence of the spectrum. Further discussion of D_{4h} symmetry and the TiO_2 spectrum will be given elsewhere.[18]

B. The Sc $L_{2,3}$ edge of Sc_2O_3 and ScF_3

Figure 10 shows the Sc $L_{2,3}$ edge of Sc_2O_3 overlayed with a calculated spectrum for a crystal field of 1.83 eV. The broadening factors used are given in Table IV. The ScF_3 spectrum, Fig. 11, was measured by Chen *et al.* at Brookhaven National Laboratory (BNL).[19]

The ScF_3 spectrum is similar to Sc_2O_3, but some interesting differences can be seen: The broadening factors for the fluoride are smaller than for the oxide (see Table

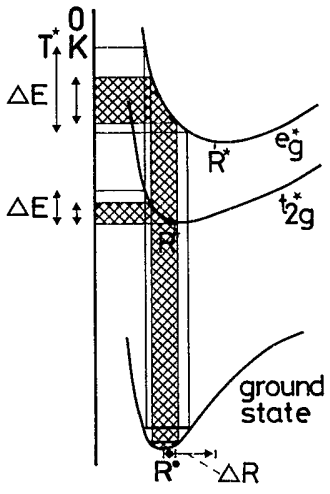

FIG. 8. Because an electron is added to an antibonding e_g or t_{2g} orbital, the equilibrium interatomic distance (R) becomes larger. The largest ΔR occurs for the e_g^* orbital. Following the Franck-Condon principle this leads to the largest broadening (ΔE). Raising the temperature from 0 K (T) to a finite temperature (T^*) enlarges ΔE both for the e_g and t_{2g} peaks.

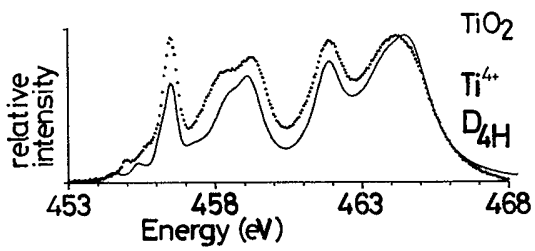

FIG. 9. The experimental TiO_2 spectrum (dotted), measured with the SX700 monochromator at BESSY, is compared with a multiplet calculation in D_{4h} symmetry. The crystal-field parameter ($10Dq$) is 1.8 eV and the values for the 420 and 220 branches are 0.75 and 0.3 eV, respectively; the broadening factors are similar to those for $FeTiO_3$.

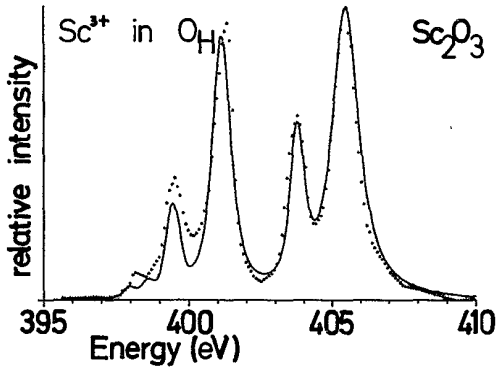

FIG. 10. The experimental Sc_2O_3 spectrum (dotted), measured with the SX700 monochromator at BESSY, is compared with a multiplet calculation in O_h symmetry. The crystal-field parameter is 1.8 eV; the broadening factors are tabulated in Table IV.

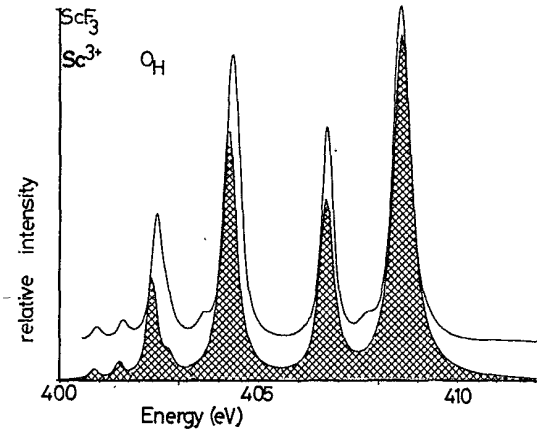

FIG. 11. The experimental ScF_3 spectrum (solid line), measured with the "dragon" monochromator at Brookhaven National Laboratory (BNL) Chen *et al.*, is compared with a multiplet calculation in O_h symmetry (shaded area). The crystal-field parameter is 1.7 eV; the broadening factors are tabulated in Table IV.

IV). Notice that this is no resolution effect, which is taken care of by the extra Gaussian broadening. The small leading peaks come out more clearly in the ScF_3 spectrum: Close comparison of the calculated multiplets with $FeTiO_3$ and Sc_2O_3 (Figs. 7 and 10), shows small discrepancies in the energy position of the leading peaks. In the experimental spectra they are situated closer to the rest of the spectrum. This discrepancy is not found in ScF_3 (and CaF_2, see the next section), which indicates that for the fluorides the Coulomb and exchange parameters (F^2, G^1, and G^3), which dominate the precise energy position of the leading peaks, have the atomic value, and thus are not screened. In our present calculations we used a 20% reduction from the *ab initio* Hartree Fock (HF) values. The reduction to 80% of the HF values originate from the practice of fitting calculated multiplets to atomic data.[15] The reduction results from the inclusion of many-body corrections (configuration interaction) leading to effective parameters.

We can conclude that, while for ScF_3 the atomic approach works out well, the spectra of the oxides indicate that the effective Coulomb and exchange parameters must be further reduced. This leads to leading peaks closer to the rest of the spectrum, but another result is a change in the intensity distribution of the main peaks resulting in a change in the L_3/L_2 branching ratio.[8,9,30,31] The reduction of the intra-atomic interactions in the oxides means that solid-state effects are more important. Covalent screening can cause reduced effective values of the intra-atomic interactions. We find that these screening effects do not play a significant role in ScF_3 and CaF_2 (see Fig. 13), which marks a clear distinction between fluorides and oxides. This agrees with the clearly larger solid-state broadening in the oxides compared with the fluorides (see Table IV) and with the concept that fluorides are more ionic.

C. The Ca $L_{2,3}$ edge of CaF_2

CaF_2 has been frequently studied because of its interesting theoretical and practical aspects.[32–35] With our calculations we are able to disprove the suggestion that the small leading peaks in the $L_{2,3}$ XAS spectrum of

TABLE IV. The broadening parameters for Lorentzian broadening of the individual peaks. σ is the Gaussian broadening factor which simulates the experimental resolution. The individual numbers should not be taken too literally. The trend in the values for the CK Auger (α) and the solid-state broadening (β) is, however, clear. The crystal-field splitting ($10Dq$) shows a trend similar to the broadenings. Notice that all *KX* spectra were fitted with the same broadenings, which were not fully optimized and from which it is not possible to derive values for α and β.

	Peaks							
Compound	a_1	a_2	b_1	b_2	σ	α	β	$10Dq$
KX	0.14	0.22	0.20	0.22	0.03			0.6 (KF) 1.1 (KI)
CaF_2	0.08	0.15	0.10	0.18	0.03	0.02	0.07	−0.9
ScF_3	0.13	0.20	0.19	0.26	0.03	0.06	0.07	1.7
Sc_2O_3	0.10	0.30	0.25	0.45	0.15	0.15	0.20	1.8
$FeTiO_3$	0.10	0.60	0.50	1.00	0.15	0.40	0.50	1.8

CaF_2 are related to Ca^+ ($4s$).[32] Figure 12 shows the spectrum with a crystal-field splitting ($10Dq$) of about -0.9 eV, which compares well with the experimental result for bulk CaF_2 (Ref. 34) [and also for seven layers of CaF_2 on Si (Refs. 32 and 33)]. Notice that negative values of $10Dq$ are used, because the calcium ion is in eightfold coordination (simple-cubic). The two main lines are reproduced, as well as the small leading peaks. In this case the leading peaks also include the low-energy peaks of the crystal-field doublet, the a_1 and b_1 peak, which have low intensity because of the small and negative value of $10Dq$. The ΔL_2 and ΔL_3 splittings deviate strongly from $10Dq$ and from each other, which prohibits a direct explanation of the individual peaks and thus necessitates a full atomic multiplet calculation. Including the crystal field, this can fully explain the Ca $L_{2,3}$ XAS spectrum and the small leading peaks come out "automatically," without recourse to the $4s^1$ configuration.

In Fig. 12 there are some small discrepancies: In the experimental spectrum there exists an extra peak at ~ 352.3 eV (b') and also the a' peak at ~ 348.7 eV is considerably more intense. We believe that this originates from a shifted superposition of the spectrum as a result of surface (or damage) effects. This shift is also observed in a surface study of CaF_2 on Si,[32,33] in which it is suggested that in the surface layer of CaF_2 the Ca ions have an extra $4s$ electron. The (formally) monovalent Ca^+ ions shift the spectrum to lower energy. If this is correct the spectrum originates from a $4s^1$ to $2p^5 3d^1 4s^1$ transition, which can result in a modified multiplet spectrum. To check this we performed a series of calculations with different crystal fields: We calculated the Ca^+ $2p^5 3d^1 4s^1$ in O_h symmetry and also in lower symmetries (D_{4h} and D_{3d}) to make a better simulation of the surface symmetry. Experimentally a polarization dependence is found,[32] which clearly proves the existence of a symmetry lower than O_h. In a future paper we will focus on CaF_2 and discuss the different multiplet calculations in detail.[36]

D. The K $L_{2,3}$ edges of potassium halides

To complete the series of d^0 compounds, we have calculated the potassium $L_{2,3}$ edges from the K^+ $2p^5 3d^1$ multiplets with the crystal-field parameter between 0 and 1 eV, and compared the results with the data of the potassium halides from Sette *et al.*[37]

Our calculations are in excellent agreement with the experimental results. In Fig. 13 the experimental results are compared with approximately the corresponding calculated K^+ $p^5 d^1$ multiplets. We did not optimize our results accurately to the experimental spectra, but the excellent visual agreement makes one sure of the possibility to do so. With the use of the relation between $10Dq$ and the splittings between the main peaks (see Fig. 4), the values for $10Dq$ can be extracted from the experimental spectra. The small inequality of the L_3 and L_2 splittings (Fig. 4) and the small leading peaks are visible in the experiment. The small peaks in between the L_3 and L_2 edge, and the bumps around 300 eV, are not explained by the present multiplet calculation. They are probably related to the $4s$ bands, although there is also a possibility that they originate from a lower symmetry, eventually in combination with surface effects (as for CaF_2).

The four calculated spectra in Fig. 13 are broadened

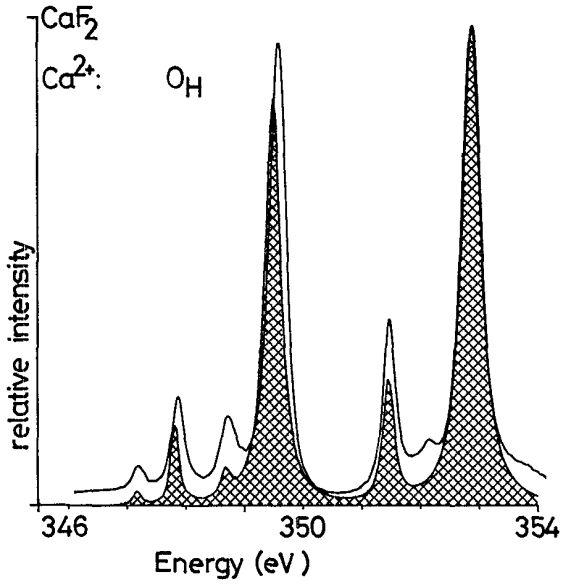

FIG. 12. The experimental CaF_2 spectrum (solid line), measured with the "dragon" monochromator at BNL by Chen *et al.*, is compared with a multiplet calculation in O_h symmetry (shaded area). The crystal-field parameter is -0.9 eV; the broadening factors are tabulated in Table V.

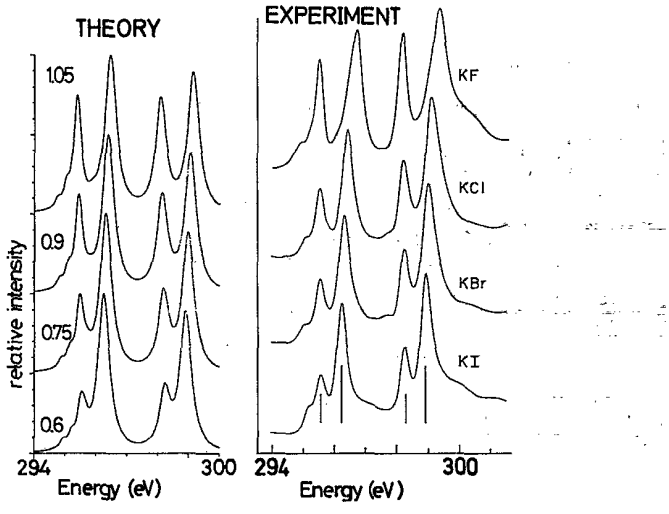

FIG. 13. Four K^+ $2p^5 3d^1$ excitation spectra in O_h symmetry (right side) are compared with the four potassium halide spectra, measured with the dragon monochromator at BNL by Chen *et al.* (left side). The calculated spectra are not completely optimized to the experiment. The broadenings used are adjusted to KI. Notice that the KF spectrum is broader (see text).

with identical broadening factors (see Table IV). Close comparison to the experimental spectra reveals that the a_2 and b_2 peaks are extra broadened for KF compared to KI. Or in other words, the solid-state broadening of the e_g peaks (see Sec. IV B) is considerably larger for KF. Going through the halide series the dominant change is the potassium-halide interatomic distance, as given in Table V. We will examine their relation to the possibility of vibrational and dispersional broadening.

A shorter interatomic distance means that the final-state vibrational broadening will be larger: A shorter distance results in a larger expansion (ΔR) after the filling of the antibonding e_g orbital. KF has shorter interatomic distances than KI, thus KF should have a larger broadening.[38] The trend in the vibrational broadening is thus in agreement with experiment.

Considering the dispersional effects a distinction can be made between broadening due to K^+-halide hybridization and K^+-K^+ hybridization. The direct cation interactions are expected to be smaller and in general they can be neglected for ioniclike compounds. We will, however, shortly consider both possible sources of dispersion. The hybridization with the ligand is expected to be largest for iodide, which would lead to the largest broadening for KI, opposite to the experimental trend. Thus ligand hybridization cannot explain the observed broadenings. Direct cation-cation interactions (K^+-K^+ hybridization) should in rocksalt structure be larger for the t_{2g} orbitals, compared to the e_g orbitals. This is also in contrast with the experimental observation that the a_2 and b_2 peaks (corresponding largely to e_g orbitals) are broader than the a_1 and b_1 peaks (corresponding largely to t_{2g} orbitals).

The conclusion is that both possible sources of dispersional broadening do not agree with the experimental observation. Thus the extra broadening for the e_g peaks in KF is caused by vibrational broadening, which also suggests that, at least for the potassium halides, final-state vibrational broadening is the dominant broadening factor. As can be seen in Table IV the amount of broadening scales with the interatomic distance for all compounds discussed.

TABLE V. The crystal structure and nearest-neighbor metal-ligand distances (R_{ML}) of the discussed compounds. Data from Ref. 28.

Compound	Crystal structure	R_{ML}
KF	rocksalt	2.66
KCl	rocksalt	3.14
KBr	rocksalt	3.29
KI	rocksalt	3.53
CaF_2	fluorite	2.27
ScF_3	cubic ReO_3	2.11*
Sc_2O_3	Re_2O_3-C	2.01*
$FeTiO_3$	ilmenite	1.92(3)
		2.06(3)
TiO_2	rutile	1.94(4)
		1.99(2)

*Reference 27.

V. CONCLUDING REMARKS

We have shown that an atomic multiplet calculation followed by a transformation to a cubic crystal field (O_h symmetry) can reproduce excellently the transition-metal $L_{2,3}$ x-ray-absorption edges of the d^0 compounds discussed. Within this description it becomes clear that the splitting between the two main peaks in both the L_3 and L_2 edge is related, though not equal to the crystal-field splitting $10Dq$. Also the small leading peaks can be explained as a part of the p^5d^1 multiplet. Their position is controlled by the Coulomb and exchange parameters (F^2, G^1, and G^3). The crystal field does not influence them strongly, which causes their uniform appearance in the spectra.

Each main peak has its own individual broadening, which is caused by the Coster-Kronig Auger decay process of the L_2 edge and by the solid-state broadening of the "e_g" peaks. From the discussion of the potassium-halide spectra it becomes clear that the dominant solid-state broadening effect is the final-state vibrational broadening.

The central discriminating factor for the e_g broadening is the interatomic radius. A small radius results in a large broadening and also a large crystal-field splitting. This causes the broadening trend for the potassium halides to be $F^- > Cl^- > Br^- > I^-$, in agreement with the trend in the radii. From this observation it can be concluded that for the potassium halides the crystal-field splitting originates dominantly from ionic factors. The covalent contribution, which can be expected to be largest for iodide, can be neglected in first approximation.

It is shown that the small leading peaks in the fluoride spectra (CaF_2 and ScF_3) fully agree with the "atomic" multiplet spectra. In the oxide spectra, however, the leading peaks are closer to the rest of the spectrum, which is a mark of decreased intra-atomic Coulomb and exchange parameters. In the oxides the effects of the solid state (covalent screening) are so large that the intra-atomic interactions (on the empty $3d$ electron states) are rescaled, while for F^- no effect is found. This marks a different "nature" of the oxides compared to the fluorides. Fluorides can be considered as ionic, while oxides have some important covalent character.

We have shown that with our calculations, which treat the atomic multiplet effects in detail, it becomes possible to separate out the atomic effects from solid-state effects. This makes it possible to study the latter, i.e., the broadening of the peaks, related to the final-state vibrational broadening and the CK Auger decay, the exact position of the small leading peaks, related to the covalent screening of intra-atomic (pd) Coulomb and exchange interactions, and the presence of extra peaks, related to surface effects and/or reduced symmetry.

Finally we point out the relationship between vibrational broadening and the (static) lowering of the symmetry. Vibrations can be viewed as dynamical distortions of the site symmetry. The Franck-Condon principle states that x-ray absorption is a fast process with respect to vibrations. The symmetry of the absorbing (transition-metal) cation is constantly changing. This affects the

XAS spectrum, which in this picture can be viewed as a superposition of all possible distorted site symmetries. The difference with a static symmetry breaking is that in that case a specific point-group symmetry can be applied to all cations, which results in a different spectrum, as for TiO_2. For cases like $FeTiO_3$, with structureless peaks it is not trivial to separate the (small) static lowering of symmetry from the dynamical (vibrational) symmetry-breaking effects. To answer the questions concerning these effects it would be desirable to study a compound more closely, experimentally as well as theoretically. Measurements at low temperatures can reduce the dynamical effects and possibly reveal the static symmetry effects. Theoretically all lower point groups can be calculated, and in principle also the dynamical effects can be simulated.

ACKNOWLEDGMENTS

We are grateful to the staff of the Berliner Elektronenspeicherring-Gesellschaft für Synchrotronstrahlung (BESSY) for their support during the XAS experiments. This work was supported, in part, by the Dutch Foundation for Chemical Research [Stichting Scheikundig Onderzoek Nederland (SON)] with financial assistance of the Netherlands Organization for Scientific Research [Nederlandse Organisatie voor wetenschappelijk Onderzoek (NWO)] and by the Committee for the European Development of Science and Technology (CODEST) program. We also thank C. T. Chen, F. Sette, and F.J. Himpsel for permission to reproduce previously unpublished results.

[1]Examples of high-resolution (1:1000) monochromators in the 300–800-eV range include the SX700 at BESSY, H. Petersen, Nucl. Instrum. Methods A **246**, 260 (1986), and the 10-m grazing-incidence monochromator at Photon Factory, H. Maezawa, S. Nakai, S. Mitani, A. Mikuni, T. Namioka, and T. Sasaki, *ibid.* **246**, 310 (1986).

[2]An even better resolution (up to 1:10 000) is reached by the dragon monochromator at BNL: C. T. Chen, Nucl. Instrum. Methods A **256**, 595 (1987).

[3]Compare the present resolution with, e.g., the resolution reached in 1982 as can be found in R. D. Leapman, L. A. Grunes, and P. L. Fejes, Phys. Rev. B **26**, 614 (1982).

[4]A former description has been given by T. Yamaguchi, S. Shibuya, S. Suga, and S. Shin, J. Phys. C **15**, 2641 (1982).

[5]This approch has been proven very successful for the rare-earth $M_{4,5}$ edges; see, e.g., B. T. Thole, G. van der Laan, J. C. Fuggle, G. A. Sawatzky, R. C. Karnatak, and J. M. Esteva, Phys. Rev. B **32**, 5107 (1985).

[6]For the $L_{2,3}$ x-ray-absorption edges the atomic approach is not sufficient and the crystal field has to be included; see, e.g., B. T. Thole, R. D. Cowan, G. A. Sawatzky, J. Fink, and J. C. Fuggle, Phys. Rev. B **31**, 6856 (1985).

[7]The theoretical basis for this method can be found in R. D. Cowan, J. Opt. Soc. Am. **58**, 808 (1968), and R. D. Cowan, *The Theory of Atomic Structure and Spectra* (University of California Press, Berkeley, 1981).

[8]J. Zaanen, G. A. Sawatzky, J. Fink, W. Speier, and J. C. Fuggle, Phys. Rev. B **32**, 4095 (1985).

[9]J. Fink, Th. Müller-Heinzerling, B. Scheerer, W. Speier, F. U. Hillebrecht, J. C. Fuggle, J. Zaanen, and G. A. Sawatzky, Phys. Rev. B **32**, 4899 (1985).

[10]P. H. Butler, *Point Group Symmetry, Applications, Methods and Tables* (Plenum, New York, 1981).

[11]J. R. Derome and W. T. Sharp, J. Math. Phys. **6**, 1584 (1965).

[12]P. H. Butler and B. G. Wybourne, Int. J. Quantum Chem. **10**, 581 (1976).

[13]E. U. Condon and G. H. Shortley, *The Theory of Atomic Spectra* (Cambridge University Press, Cambridge, 1964).

[14]This part is also nicely discussed by C. J. Ballhausen, in *Introduction to Ligand Field Theory* (McGraw-Hill, New York, 1962).

[15]R. D. Cowan, *The Theory of Atomic Structure and Spectra* (University of California Press, Berkeley, 1981), p. 464, and references therein.

[16]G. van der Laan, B. T. Thole, and G. A. Sawatzky, Phys. Rev. B **37**, 6587 (1988).

[17]F. M. F. de Groot, B. T. Thole, and G. A. Sawatzky (unpublished).

[18]F. M. F. de Groot, B. T. Thole, and G. A. Sawatzky (unpublished).

[19]C. T. Chen and F. Sette (private communication).

[20]A. F. Wells, *Structural Inorganic Chemistry,* 3rd ed. (Clarendon, Oxford, 1962), p. 486.

[21]R. E. Newnham, J. H. Fang, and R. P. Santoro, Acta Crystallogr. **17**, 240 (1963).

[22]J. B. Goodenough, Phys. Rev. **117**, 1442 (1960); Prog. Solid State Chem. **5**, 145 (1972).

[23]With a Gaussian broadening of 0.15 eV we mean that the parameter σ is chosen as 0.15 eV; this also applies for the Lorentzian broadenings.

[24]J. Zaanen and G. A. Sawatzky, Phys. Rev. B **33**, 8074 (1986).

[25]This procedure is not exact, but it is good enough for the accuracy needed.

[26]C.-O. Almbladh and L. Hedin, in *Handbook on Synchrotron Radiation,* edited by E. E. Koch (North-Holland, Amsterdam, 1983), Vol. 1, p. 635.

[27]D. K. G. de Boer, C. Haas, and G. A. Sawatzky, Phys. Rev. B **29**, 4401 (1984).

[28]A. F. Wells, Ref. 20, p. 461.

[29]Our spectrum is equivalent to the EELS spectrum of Brydson *et al.*, R. Brydson, B. G. Williams, W. Engel, H. Sauer, E. Zeitler, and J. M. Thomas, Solid State Commun. **64**, 609 (1987).

[30]B. T. Thole and G. van der Laan, Phys. Rev. B **38**, 3158 (1988).

[31]G. van der Laan and B. T. Thole, Phys. Rev. Lett. **60**, 1977 (1988).

[32]D. Rieger, F. J. Himpsel, U. O. Karlsson, F. R. McFreely, J. F. Morar, and J. A. Yarmoff, Phys. Rev. B **34**, 7295 (1986).

[33]F. J. Himpsel, U. O. Karlsson, J. F. Morar, D. Rieger, and J. A. Yarmoff, Phys. Rev. Lett. **56**, 1497 (1986).

[34]C. T. Chen and F. Sette, Phys. Rev. Lett. **60**, 160 (1988).

[35]F. J. Himpsel, U. O. Karlsson, J. F. Morar, D. Rieger, J. A. Yarmoff, Phys. Rev. Lett. **60**, 161 (1988).

[36]F. J. Himpsel *et al.* (unpublished).

[37]F. Sette, B. Sinkovic, Y. J. Ma, and C. T. Chen, Phys. Rev. B **39**, 11 125 (1989).

3.4. Metal $2p$ x-ray absorption of $3d$ transition metal compounds

Metal 2p x-ray absorption of 3d transition metal compounds

Reproduced from *Physical Review B.*, volume **42**, page 5459 - 5468 (1990).

This paper contains the crystal field multiplet calculations for compounds with a partially filled $3d$-band. The crystal field multiplets of the $3d^N \rightarrow 2p^5 3d^{N+1}$ transitions are given for the common valencies of the $3d$-metal ions. A comparison with $2p$ x-ray absorption experiments is made for VF_3, MnF_2 and CoF_2 and excellent agreement is found. (Due to an error in a plotting routine, some multiplets for $10Dq = 0$ as given in the paper are not correct. The correct spectra will be almost equal to the spectra as given for $10Dq = 0.3$ eV in all cases).

2p x-ray absorption of 3d transition-metal compounds: An atomic multiplet description including the crystal field

F. M. F. de Groot and J. C. Fuggle
Research Institute for Materials, University of Nijmegen, Toernooiveld, 6525 ED Nijmegen, The Netherlands

B. T. Thole and G. A. Sawatzky
Materials Science Centre, University of Groningen, Nijenborgh 18, Paddepoel, 9747 AG Groningen, The Netherlands
(Received 30 January 1990; revised manuscript received 4 June 1990)

The metal 2p x-ray-absorption spectra (or $L_{2,3}$ edges) of 3d transition-metal compounds are calculated, using atomic multiplet theory with inclusion of the cubic crystal field. A general overview of the effect of the cubic crystal field on the shape of the $3d^N$ to $2p^5 3d^{N+1}$ excitation spectrum is given for 14 common valencies of 3d transition-metal ions. Comparison to some high-resolution 2p x-ray-absorption spectra shows excellent agreement, which confirms the validity of the approach. Possible refinements of the theory, including lower-symmetry calculations and the inclusion of configuration interaction, are discussed.

I. INTRODUCTION

As a result of the experimental progress in the field of (soft-) x-ray-absorption spectroscopy (XAS), the attainable resolution has improved to its present best value of 1:10 000.[1] The high-resolution 2p x-ray-absorption spectra of transition-metal compounds show a large amount of structure at the edge, which now can be investigated in detail. In this paper we present a theoretical analysis of these spectra, based on atomic multiplet theory with the inclusion of the cubic crystal field. A similar method has been used by Yamaguchi *et al.*[2]

We summarize briefly the general description of the absorption process to clarify the difference of our approach with the more common single-particle density of states (DOS) and multiple-scattering approaches. The x-ray-absorption cross section is given by[3]

$$\sigma(E_x) \sim \sum_f |\langle \phi_i | X | \phi_f \rangle|^2 \delta(E_i + E_x - E_f) , \quad (1)$$

where E_x, E_i, and E_f are, respectively, the energy of the photon, the initial state, and the final state. X is the perturbation acting on the system, which in this case is the absorption process of the photon, for which we will use the dipole approximation.[3] ϕ_i and ϕ_f are the initial- and final-state wave functions. In the single-particle DOS approach, ϕ_i is taken as a core state and ϕ_f is an empty state, which is coupled via the dipole selection rules. For 2p x-ray absorption, the dipole-allowed transitions are $2p \rightarrow 3d$ and $2p \rightarrow 4s$, but as transitions to 3d states dominate over transitions to 4s states, the latter will be neglected. This leads to the expression

$$\sigma_{2p}(E_x) \sim |\langle \phi(2p) | X | \phi(3d) \rangle|^2 \mathcal{P}_{3d}(E_x - E_{2p}) , \quad (2)$$

where $\mathcal{P}_{3d}(E)$ is the unoccupied 3d-projected DOS. The (projected) DOS is normally calculated using density-functional theory (DFT).[4] For the description of x-ray absorption, real-space multiple-scattering (MS) methods, which have been shown to be equivalent to DFT,[5] are also used.

We follow another approach in treating the x-ray-absorption cross section. Our main assumption is that for 3d transition-metal compounds, the 3d-3d as well as the 2p-3d two-particle interactions are most important for the description of the 2p XAS spectrum. It is these two-particle interactions which define the ground state of the transition-metal ion and which split the XAS final state into a large number of configurations. In the single-particle DOS approximations, the 3d-3d and 2p-3d two-particle interactions are not included. Because we want to calculate them explicitly, we start with the calculation of the atomic multiplets, thereby neglecting all solid-state effects. In the atomic approach the 2p XAS cross section for $3d^N$ transition-metal ions is,

$$\sigma_{2p}(E_x) \sim \sum_j |\langle \phi_G(3d^N)_{O(3)} | X | \times \phi_{fj}(2p^5 3d^{N+1})_{O(3)} \rangle|^2 \delta(E_G + E_x - E_f) , \quad (3)$$

where $\phi_G(3d^N)_{O(3)}$ is the ground state of the $3d^N$ multiplet in spherical [O(3)] symmetry. $\phi_{fj}(2p^5 3d^{N+1})_{O(3)}$ is state j in the final-state atomic multiplet spectrum. To include solid-state effects, a cubic-crystal-field term is added to the Hamiltonian. The cubic-crystal-field coupling is treated as a free parameter to be varied to obtain the best fit to experiment. Distortions from cubic symmetry are not considered.

In Sec. II we repeat some general aspects of atomic multiplet theory as far as what is important for partly filled initial states. In Sec. III we will present an overview of the effect of the cubic crystal field on the $3d^N$ to $2p^5 3d^{N+1}$ excitation for 14 common vacancies of transition-metal ions. We will use crystal-field strengths between 0 and 2.5 eV. As examples for the validity of our method, we will compare the results with some high-

resolution experimental results of $3d$ transition-metal fluorides in Sec. IV. Section V describes possible reasons for discrepancies and possible refinements.

II. THEORY

The calculations consist of three steps. First, the energy levels in the initial-state $3d^N$ multiplet and the final-state $2p^5 3d^{N+1}$ multiplet are calculated in O(3) symmetry. Then the atomic multiplet spectrum is calculated by means of the dipole transition from the ground state (in the initial-state multiplet) to all final states. The third part is the projection of the O(3) multiplets to cubic (O_h) symmetry.

A. Atomic multiplet spectrum

The Hamiltonian of the $3d^N$ initial-state multiplet consists only of the $3d$-$3d$ Coulomb interaction (H_{dd}), which is developed in spherical harmonics.[6] The radial parts F^0_{dd}, F^2_{dd}, and F^4_{dd} are calculated within the Hartree-Fock (HF) limit and corrected by hand to 80% of the HF result to include intra-atomic configuration interaction (CI).[7] The isotope interaction ($f_0 F^0$) does not affect the multiplet, but causes a shift in the average energy position. Our calculation is not suited for the calculation of the absolute energy position. Therefore, we simply shift our calculated multiplet for comparison to experiment. The multiplet splitting is determined by the multipole terms of the $3d$-$3d$ interaction, F^2_{dd} and F^4_{dd}, which also determine the Hund's-rule ground state within the initial-state $3d^N$ multiplet.[8] The $3d$ spin-orbit coupling is small and is neglected as hybridization and temperature effects will mix the spin-orbit-split states.

The $2p^5 3d^{N+1}$ final-state Hamiltonian is extended with two terms related to the $2p$ core hole: first, the spin-orbit coupling of the $2p$ hole ($H_{\underline{c}LS}$), which causes the division of the $2p$ edge into the $2p_{3/2}$ (L_3) and $2p_{1/2}$ (L_2). In our calculation we will always consider the full $2p$, thus $L_{2,3}$, spectrum. The second term which originates from the core hole is the $2p$-$3d$ Coulomb and exchange interaction ($H_{\underline{c}d}$). Again, the radial parts of the $2p$-$3d$ Coulomb (F^0_{pd} and F^2_{pd}) and exchange (G^1_{pd} and G^3_{pd}) multipole interactions are calculated *ab initio*. The isotropical $2p$-$3d$ Coulomb interaction $f_0 F^0_{pd}$ is equal for all final states (in a specific $2p^5 3d^{N+1}$ multiplet). The total Hamiltonian for the atomic multiplet then is

$$H_A = H_{dd} + H_{\underline{c}LS} + H_{\underline{c}d} \ .$$

B. Cubic-crystal-field effect on the $2p^5 3d^{N+1}$ multiplet

To simulate the solid we add an extra term to the Hamiltonian describing the cubic crystal field (H_{CCF}). In the present calculations we assume that the cubic-crystal-field parameter ($10Dq$) is equal for initial and final states.

In terms of group theory, the effect of a cubic crystal field is the reduction of symmetry from O(3) to O_h. The group-theoretical treatment of the transformation from O(3) symmetry to its subgroup O_h, further called O(3)-O_h branching, can be found in Refs. 9–11. In our paper on the d^0 compounds, we considered it in more detail.[12]

The cubic crystal field splits the initial-state multiplet. For small cubic crystal fields, the ground state does not change character and originates from the atomic ground state, which according to Hund's rules is high spin. For strong crystal fields a change of character can occur and the ground state can become low spin. That is, it originates from an excited state in the initial-state atomic multiplet. The general results of the influence of the cubic crystal field on the initial-state $3d^N$ multiplet can be found in the Tanabe-Sugano diagrams.[13]

The crystal field also splits the final-state multiplet. If the character of the ground state is not changed from the atomic situation, the same final states are reached. In this case the changes in the spectrum are a result from the crystal-field effect on the final state. Levels are split and/or shifted, and the transition matrix elements are modified due to changes in the final-state wave functions. This modifies the spectrum. If a change of the ground-state character occurs, this is immediately visible in the spectral shape as the dipole transitions from this new ground state reach a totally new set of final states. The dipole transition operator is not split in cubic symmetry, which means that no polarization dependence can occur.

In the Hamiltonian we neglect all other crystal-field couplings related to lower symmetries, taken together in H_{LCF}, the $3d$ spin-orbit coupling, (H_{LS}), magnetic interactions (H_{ex}), and any form of CI, intra-atomic (e.g., $3d^{N-1}4p$) as well as extra-atomic (e.g., $3d^{N+1}\underline{L}$). H_{LCF}, H_{LS}, and H_{ex} all will influence the ground-state character. But for the total, polarization-averaged XAS spectrum their influence is negligible as the effects on the final-state multiplet are too small. However, for polarization-dependent XAS measurements, a more accurate determination of the character of the ground state is needed and some extra terms will have to be added to the Hamiltonian. In Sec. V we will discuss possible refinements of the calculations in more detail.

III. CALCULATIONS

The intra-atomic interaction parameters, as calculated in the Hartree-Fock limit, are collected in Table I. The Coulomb and exchange parameters (F^2_{dd}, F^4_{dd}, F^2_{dd}, G^1_{pd}, and G^3_{pd}) are renormalized to 80% of the HF values to account for intra-atomic CI. The multiplet of the $3d^N$ initial state and the $2p^5 3d^{N+1}$ are calculated, and the ground state $\phi_G(3d^N)_{\mathrm{O(3)}}$ is determined. The XAS cross section is calculated. According to Eq. (3), the result is a series of lines at energies ($E_G - E_{fj}$) with respective intensities $|\langle \phi_G(3d^N)_{\mathrm{O(3)}} | X | \phi_{fJ}(2p^5 3d^{N+1})_{\mathrm{O(3)}} \rangle|^2$. Figure 1 gives the atomic multiplet for d^5 Mn^{2+}. Addition of the cubic-crystal-field changes the energy positions and matrix elements. Figure 2 shows the result if the cubic-crystal-field parameter ($10Dq$) is 0.9 eV.

To compare with experiment, the spectra have to be broadened. Besides the experimental broadening, there are several intrinsic broadening mechanisms. These include lifetime effects, vibrations, and hybridization (covalency), all of which are compound and final state

dependent. Because of the hundreds of (unresolvable) final states, this creates an enormous problem to solve quantitatively. For compounds with a $3d^0$ ground state, information of the final-state dependence of the broadening can be found experimentally as each of the main multiplet lines can be resolved.[12] Analysis showed that for fluorides, vibrational broadening dominates, but for oxides, also covalence causes broadening. A general result is that the lifetime broadening of the L_2 part is increased due to the opening of Coster-Kronig Auger decay channels. As a detailed analysis of the broadening is not possible from XAS alone, we decided to use an equal broadening for every line. For the L_3 part, a Lorentzian broadening with $\sigma=0.1$ eV (Ref. 14) is used; for the L_2

TABLE I. Hartree-Fock values of the parameters used in the multiplet calculation. Given are the multipole terms of the 3d-3d interaction (F^2_{dd} and F^4_{dd}) of the ground and final states. The final-state-3d–spin-orbit interaction ($\mathbf{L}\cdot\mathbf{S}_d$), 2p-hole–spin-orbit interaction ($\mathbf{L}\cdot\mathbf{S}_p$), and multipole terms of the 2p-3d interaction (F^2_{pd}, G^1_{pd}, and G^3_{pd}). In the actual multiplet calculation, the multipole terms are normalized to 80% of their *ab initio* value, to account for intra-atomic configuration interaction (all values in eV).

d_N	Ion	F^2_{dd} final states	(g.s.)	F^4_{dd} final states	(g.s.)	$\mathbf{L}\cdot\mathbf{S}_d$	$\mathbf{L}\cdot\mathbf{S}_p$
d^1	Ti^{3+}	10.343	(0.000)	6.499	(0.000)	0.027	3.776
	V^{4+}	11.965	(0.000)	7.554	(0.000)	0.042	4.650
d^2	V^{3+}	10.974	(10.127)	6.888	(6.354)	0.036	4.649
d^3	Cr^{3+}	11.596	(10.777)	7.270	(6.755)	0.047	5.667
	Mn^{4+}	13.177	(12.416)	8.299	(7.820)	0.066	6.845
d^4	Cr^{2+}	10.522	(9.649)	6.552	(6.002)	0.041	5.668
	Mn^{3+}	12.210	(11.415)	7.649	(7.148)	0.059	6.845
d^5	Mn^{2+}	11.155	(10.316)	6.943	(6.414)	0.053	6.846
	Fe^{3+}	12.818	(12.043)	8.023	(7.535)	0.074	8.199
d^6	Fe^{2+}	11.779	(10.966)	7.327	(6.815)	0.067	8.200
	Co^{3+}	13.422	(12.663)	8.395	(7.917)	0.092	9.748
d^7	Co^{2+}	12.396	(11.605)	7.708	(7.209)	0.083	9.746
	Ni^{3+}	14.022	(13.277)	8.764	(8.295)	0.112	11.506
d^8	Ni^{2+}	0.000	(12.234)	0.000	(7.598)	0.102	11.507

d^N	Ion	F^2_{pd}	G^1_{pd}	G^3_{pd}
d^1	Ti^{3+}	5.581	3.991	2.268
	V^{4+}	6.759	5.014	2.853
d^2	V^{3+}	6.057	4.392	2.496
d^3	Cr^{3+}	6.526	4.788	2.722
	Mn^{4+}	7.658	5.776	3.288
d^4	Cr^{2+}	5.841	4.024	2.388
	Mn^{3+}	6.988	5.179	2.945
d^5	Mn^{2+}	6.321	4.606	2.618
	Fe^{3+}	7.446	5.566	3.166
d^6	Fe^{2+}	6.793	5.004	2.844
	Co^{3+}	7.900	5.951	3.386
d^7	Co^{2+}	7.260	5.397	3.069
	Ni^{3+}	8.350	6.332	3.603
d^8	Ni^{2+}	7.721	5.787	3.291

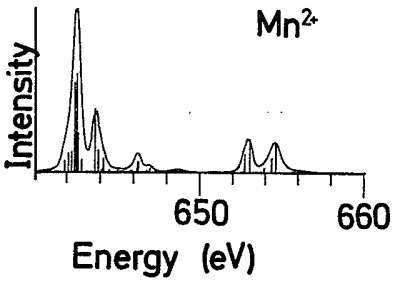

FIG. 1. Mn^{2+} $3d^5$ to $2p^53d^6$ atomic multiplet spectrum. The line spectrum is broadened as described in the text.

part, $\sigma=0.3$ eV. Then the spectra are convoluted with a Gaussian with $\sigma=0.15$ eV. We expect these broadening procedures to represent early transition-metal fluoride spectra taken with the present high-resolution monochromators.[1] Oxide and late transition-metal fluoride spectra will in general be broader (see Sec. V). Figures 1 and 2 show the effect of the broadening procedure on the two Mn^{2+} multiplet spectra.

Figures 3–16 show the effect of increasing cubic crystal field on the x-ray-absorption spectrum. The calculated energy scale is used; for comparison to experiment the spectra will have to be shifted over some eV (see Sec. IV). The $10Dq$ value is given on the right. The changes as a function of $10Dq$ are in general smooth and reflect the influence of the cubic crystal field on the final-state multiplet as discussed in Sec. II. In cases where the ground state changes character, from high to low spin, a sudden change in the spectral shape occurs as a new subset of final states is reached. This is visible for, e.g., Cr^{2+} (d^4) and Co^{3+} (d^6) between 2.1 and 2.4 eV. Because of the clear difference between high- and low-spin spectra, the actual situation is easy to determine from experiment. Some care has to be taken because the presented calculations are performed in a standard way and do not give the $10Dq$ value for this transition very accurately. Furthermore, $10Dq$ can be slightly different in initial and final states. There is no problem to include this, but it does need dedicated, compound-specific calculations.

Two ions with an equal number of $3d$ electrons, such as d^1 V^{4+} and Ti^{3+}, have a similar atomic multiplet spectrum. The only differences are the atomic parameter values of the intra-atomic interactions (see Table I), which slightly modify the spectra.

However, more important is the fact that multiplets do change significantly as the number of $3d$ electrons is changed. Compare for example, Mn^{2+}, Mn^{3+}, and Mn^{4+}. Besides the shift to higher energy with higher valency, the spectral shape does change significantly, which makes determination of the valency, and its cubic-crystal-field splitting, straightforward.

IV. COMPARISON TO EXPERIMENT

To show the validity of our approach, we make a comparison to some high-resolution $2p$ x-ray-absorption data of transition-metal fluorides obtained with the Dragon monochromator by Chen and Sette.[15]

In our paper on the $3d^0$ compounds, we showed the excellent agreement with potassium, calcium, scandium, and titanium oxides and fluorides. As the final-state p^5d^1 is simple and well resolved, it was possible to obtain detailed information, such as individual broadenings for each state. Such detailed analysis is not possible for the p^5d^{N+1} multiplets (for $N>0$), as the individual lines are not resolved (there are typically 600 lines spread over 20 eV). Therefore, the standard broadening as discussed in Sec. III is used.

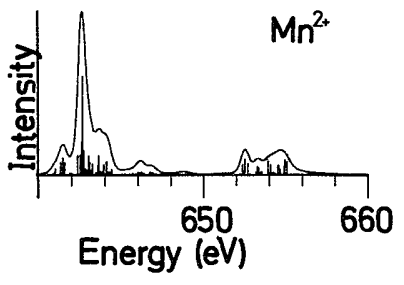

FIG. 2. Mn^{2+} $3d^5$ to $2p^53d^6$ multiplet spectrum, projected to O_h. The cubic-crystal-field parameter ($10Dq$) is 0.9 eV. The line spectrum is broadened as described in the text.

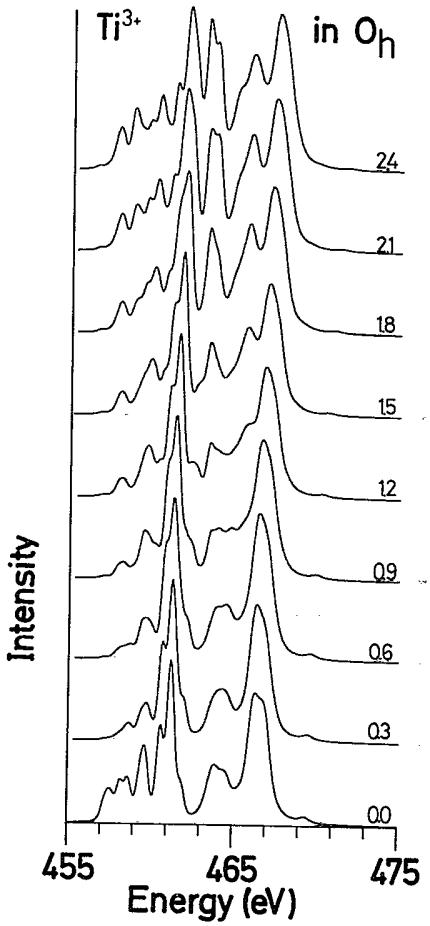

FIG. 3. Ti^{3+} $3d^1$ to $2p^53d^2$ transition in cubic crystal fields. $10Dq$ ranges from 0.0 (bottom) to 2.4 eV.

In Fig. 17 the theoretical spectra of V^{3+} (d^2), Mn^{2+} (d^5), and Co^{2+} (d^7) are compared with the experimental spectra of VF_3, MnF_2, and CoF_2 (see Table II for the crystal structures) as obtained with the Dragon,[15] The cubic-crystal-field parameters ($10Dq$) used are, respectively, 1.5, 0.75, and 0.75 eV. The overall agreement found is good for all compounds. From this we conclude that the atomic multiplet approach with the inclusion of the cubic crystal field gives a good description of all spectral details of the 2p x-ray-absorption spectra of 3d transition-metal fluorides. This also shows that the tetragonal symmetry of the metal site in CoF_2 and MnF_2 (Table II) is a too-small distortion from cubic symmetry to cause clear disagreement between experiment and the present cubic symmetry simulation. However, for the description of polarization-dependent spectra of a tetragonal site, the inclusion of the exact lower symmetry is absolutely necessary. In other words, with polarization-dependent measurements small tetragonal distortions will show up. Unfortunately, a rutile crystal structure is not suitable for polarization-dependent studies because of different orientations of the tetragonal sites.

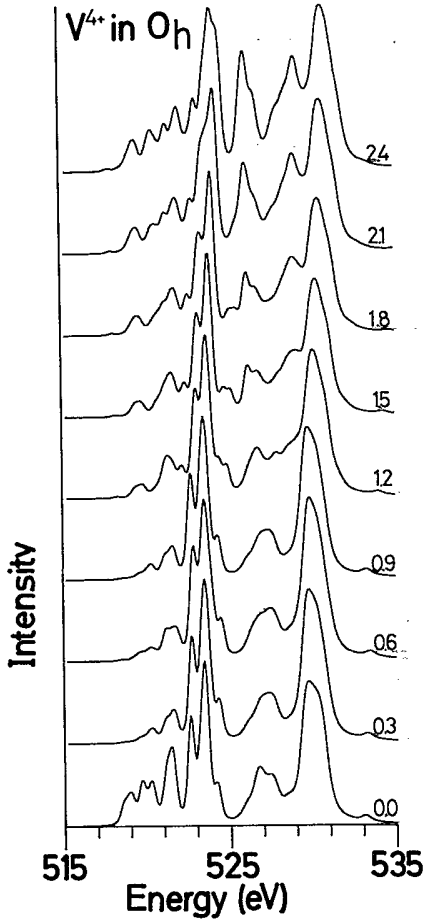

FIG. 4. V^{4+} $3d^1$ to $2p^53d^2$ transition in cubic crystal fields. $10Dq$ ranges from 0.0 (bottom) to 2.4 eV.

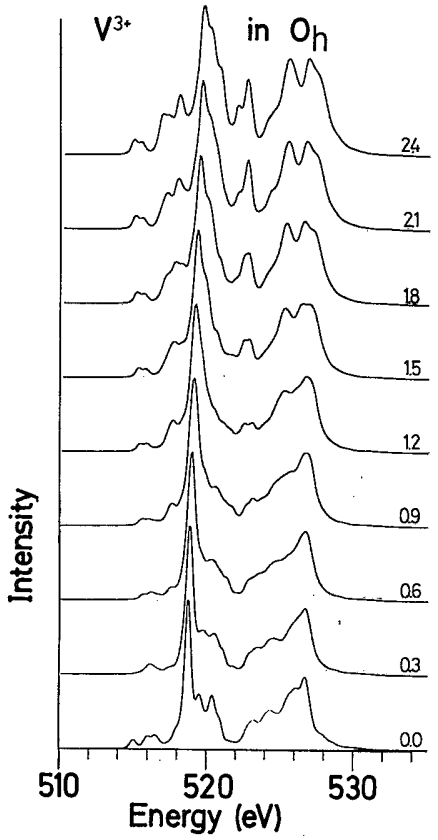

FIG. 5. V^{3+} $3d^2$ to $2p^53d^3$ transition in cubic crystal fields. $10Dq$ ranges from 0.0 (bottom) to 2.4 eV.

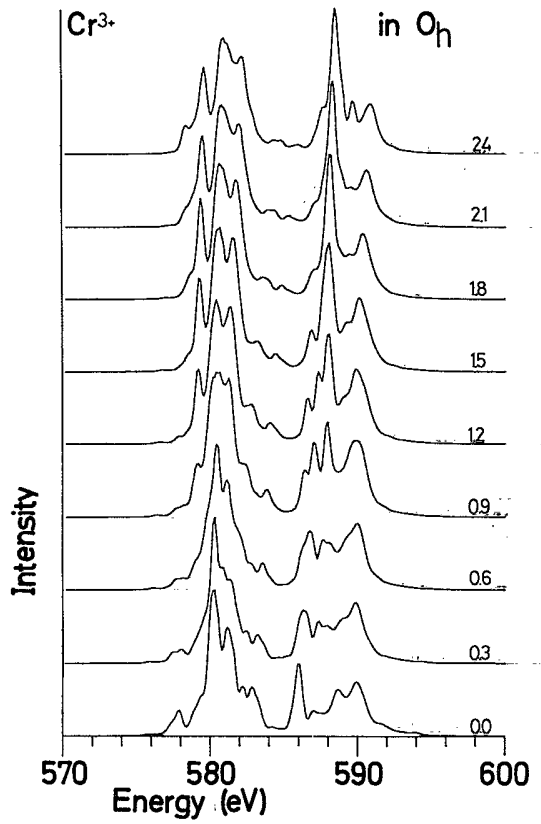

FIG. 6. Cr^{3+} $3d^3$ to $2p^53d^4$ transition in cubic crystal fields. $10Dq$ ranges from 0.0 (bottom) to 2.4 eV.

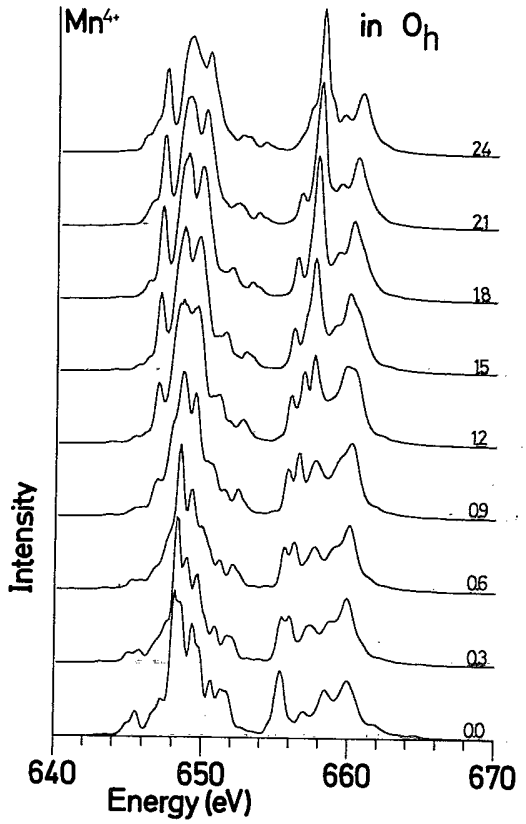

FIG. 7. Mn^{4+} $3d^3$ to $2p^53d^4$ transition in cubic crystal fields. $10Dq$ ranges from 0.0 (bottom) to 2.4 eV.

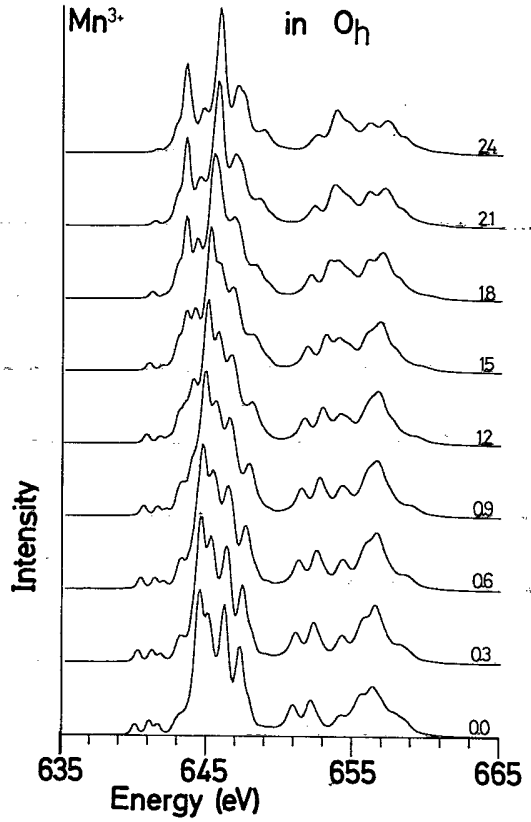

FIG. 9. Mn^{3+} $3d^4$ to $2p^53d^5$ transition in cubic crystal fields. $10Dq$ ranges from 0.0 (bottom) to 2.4 eV.

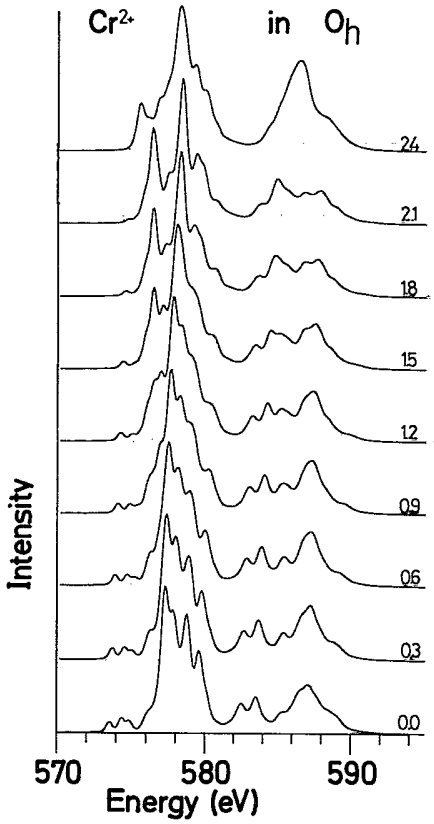

FIG. 8. Cr^{2+} $3d^4$ to $2p^53d^5$ transition in cubic crystal fields. $10Dq$ ranges from 0.0 (bottom) to 2.4 eV.

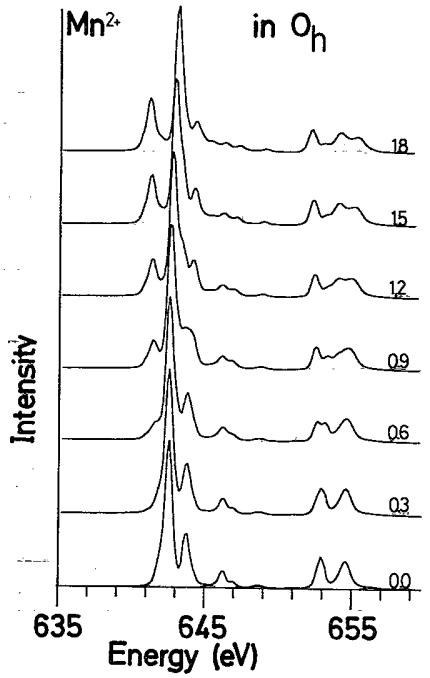

FIG. 10. Mn^{2+} $3d^5$ to $2p^53d^6$ transition in cubic crystal fields. $10Dq$ ranges from 0.0 (bottom) to 1.8 eV.

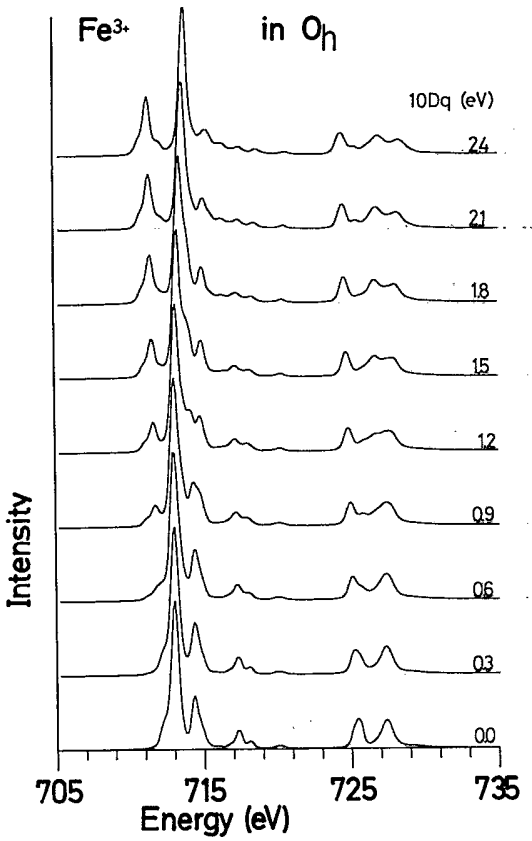

FIG. 11. Fe^{3+} $3d^5$ to $2p^5 3d^6$ transition in cubic crystal fields. $10Dq$ ranges from 0.0 (bottom) to 2.4 eV.

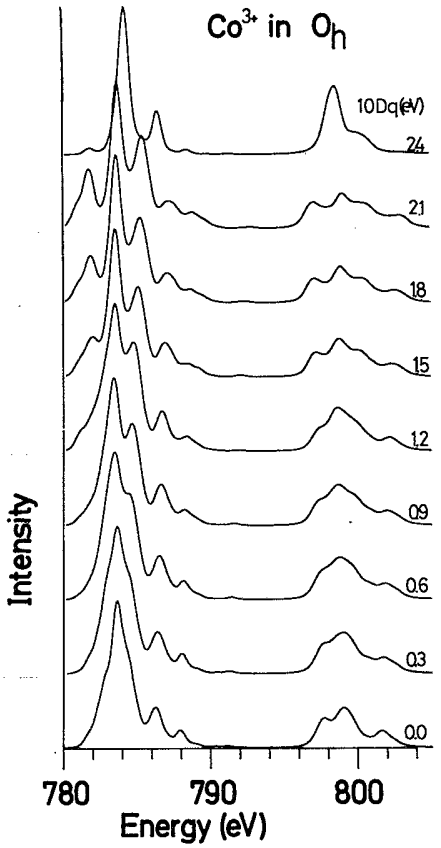

FIG. 13. Co^{3+} $3d^6$ to $2p^5 3d^7$ transition in cubic crystal fields. $10Dq$ ranges from 0.0 (bottom) to 2.4 eV.

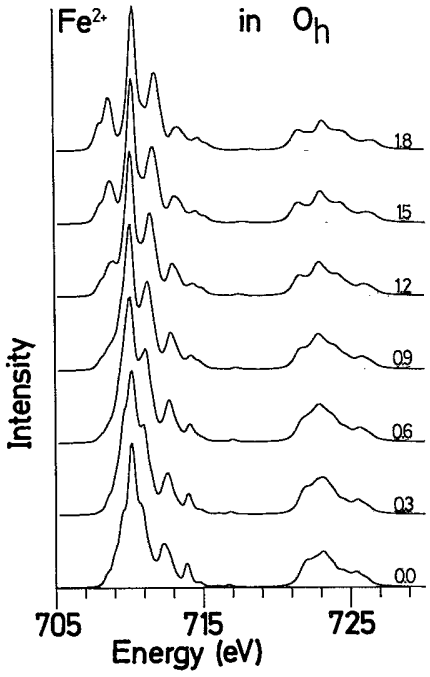

FIG. 12. Fe^{2+} $3d^6$ to $2p^5 3d^7$ transition in cubic crystal fields. $10Dq$ ranges from 0.0 (bottom) to 1.8 eV.

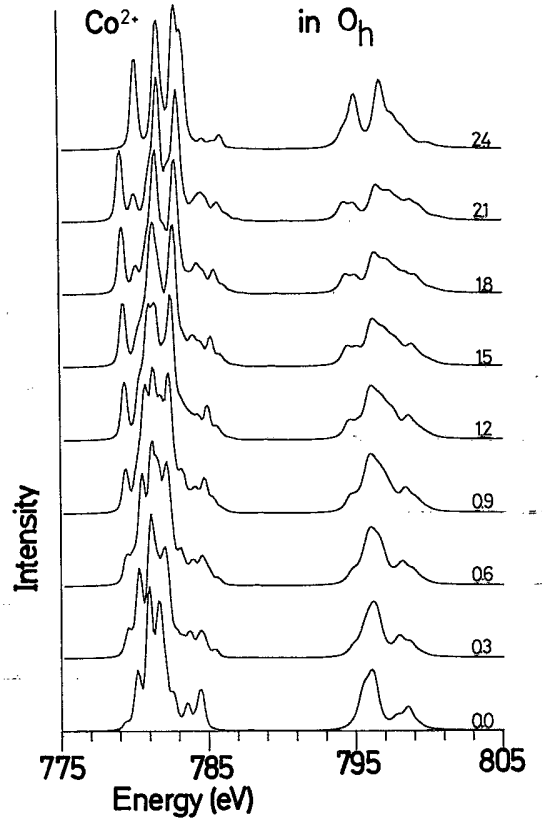

FIG. 14. Co^{2+} $3d^7$ to $2p^5 3d^8$ transition in cubic crystal fields. $10Dq$ ranges from 0.0 (bottom) to 2.4 eV.

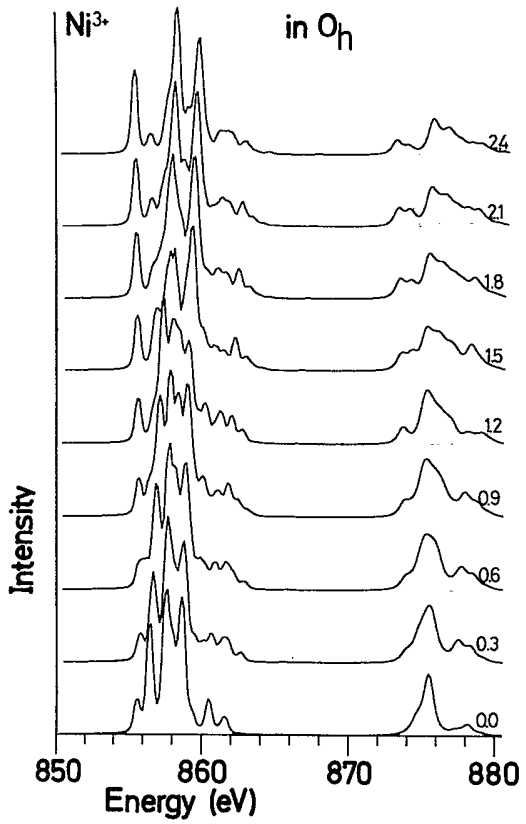

FIG. 15. Ni^{3+} $3d^7$ to $2p^5 3d^8$ transition in cubic crystal fields. $10Dq$ ranges from 0.0 (bottom) to 2.4 eV.

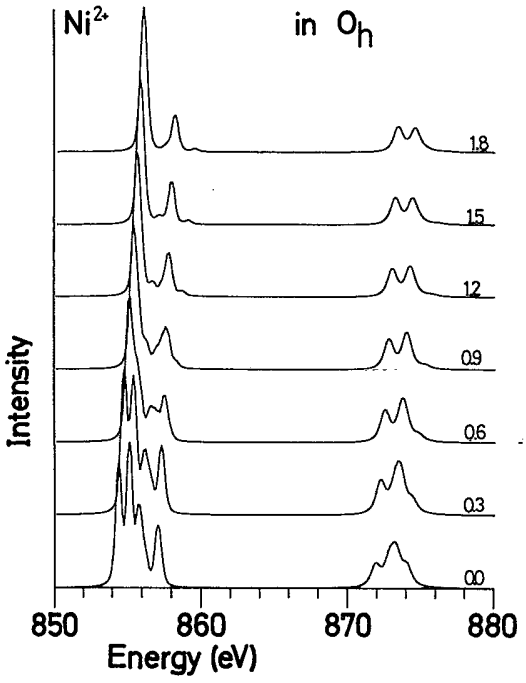

FIG. 16. Ni^{2+} $3d^8$ to $2p^5 3d^9$ transition in cubic crystal fields. $10Dq$ ranges from 0.0 (bottom) to 2.4 eV.

V. LIMITATIONS OF THIS APPROACH

There are two main limitations in the present approach to explain the $2p$ x-ray-absorption edges. First, the character of the ground state is not considered in detail. Second, the effects on the spectral shape of hybridization, vibrations, lifetime, and experimental resolution are treated very roughly as a general Lorentzian-plus-Gaussian broadening.

In Sec. II we already mentioned the necessity to include the exact lower-site symmetries (H_{LCF}), magnetic

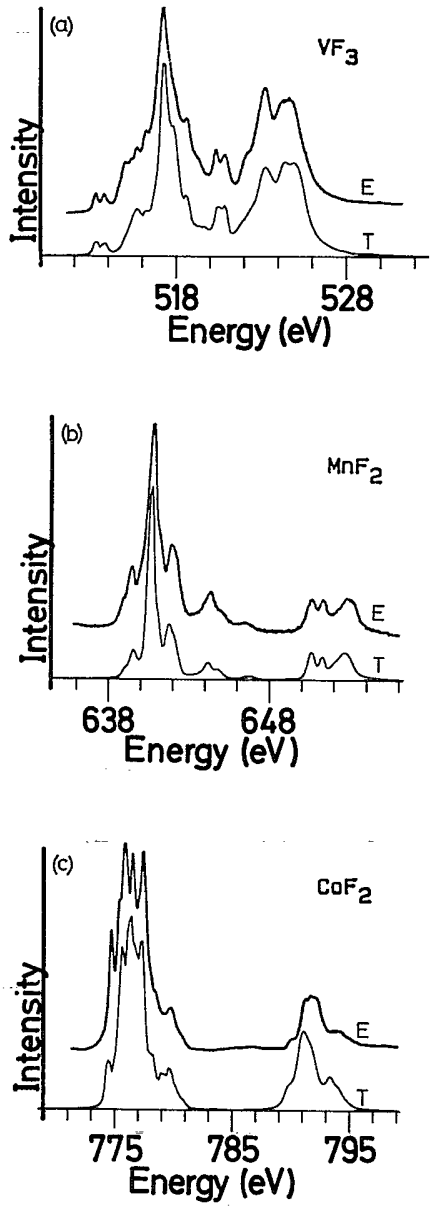

FIG. 17. $2p$ x-ray-absorption spectra of (a) VF_3, (b) MnF_2, and (c) CoF_2 compared, respectively with, the d^2V^{3+} (1.5 eV), the d^5 Mn^{2+} (0.75 eV), and the d^7 Co^{2+} (0.75 eV) multiplet calculations. The used values of $10Dq$ are given in parentheses. The theoretical spectra are shifted, by about 2 eV to lower energy, to align with experiment.

TABLE II. Crystal structures of the 3d transition-metal fluorides (Ref. 26).

Compound	Crystal structure	Point group of metal ion
VF_3	(intermediate) close packed	O_h (octahedral)
MnF_2	rutile	D_{4h} (tetragonal)
CoF_2	rutile	D_{4h} (tetragonal)

field effects (H_{ex}), and 3d spin-orbit coupling (H_{LS}) to describe the character of the ground state more accurately. H_{LCF} and H_{ex} will not influence the polarization-averaged spectral shape because the effects are generally too small to be seen in the final-state multiplet. That is, even if they modify the ground-state character considerably, the polarization-averaged (!) matrix elements hardly change. Only for strongly distorted sites can a visible effect be expected. However, for the polarization-dependent spectra, knowledge of the ground-state character is crucial for the determination of the respective matrix elements for $\Delta m = +1, -1$, or 0.[16,17] Then the interplay of H_{LCF}, H_{ex}, and H_{LS} will determine the exact ground state and, consequently, the differences in spectral shape for linear (difference between $\Delta m = 0$ and $+1/-1$) and circular (difference between $\Delta m = 1$ and -1) dichroism.

The 3d spin-orbit coupling might influence the spectral shape for solids. Its influence on the polarization-averaged spectra will be directly evident from the branching ratio between L_3 and L_2.[18] Its influence will be largest, if present at all, for the late 3d transition metals (see Table I), and indeed for CoF_2 [see Fig. 17(c)] the branching ratio, as well as the total spectral shape, is improved if the 3d spin-orbit coupling is included.[19]

We now turn to the second limitation, the use of an equal broadening for all final states in the L_3 and L_2 parts to simulate effects such as hybridization, vibrations, and lifetime. These effects will be different for every compound and even for every line in the 600-line final-state multiplet, making a detailed description totally out of reach. However, some aspects are becoming clear: For the d^0 compounds it was shown that the e_g-like states show more broadening than the t_{2g}-like states, which we related to vibrational effects. For the $2p^5 3d^{N+1}$ multiplets such conclusions cannot be drawn, but similar effects can be expected.

Hybridization, which can be treated as extra-atomic configuration interaction, will modify the spectrum considerably. Especially for more covalent materials, such as oxides, the amount of extra-atomic configuration interaction cannot be neglected: The coupling of $3d^N$ with $3d^{N+1}\underline{L}$ becomes more prominant, introducing more $3d^{N+1}\underline{L}$ character in the ground state. These aspects can be taken into account by performing a real CI calculation, as was done for the early 3d transition metals[20] and for the nickel-dihalides.[21] For the cases considered here, such a CI approach is at present not a routine task, but this line will certainly be followed in future efforts.

An alternative route is to include the effects of hybridization effectively in the atomic multiplet calculations. Hybridization, the mixing of the transition-metal 3d orbitals with the ligand p orbitals, has the effect of delocalizing the d functions, thereby reducing their mutual interactions: the nephelauxatic effect.[22] This effect can be simulated by an extra reduction of the two-particle interaction parameters F^2_{dd} and F^4_{dd}. Also the final-state interactions with the core hole will be affected. Preliminary calculations, where we reduced all parameters by the same amount, are encouraging, although the possible accuracy has to be investigated,[23] and shake-up satellites will not be reproduced properly.

The last effect which is not treated in detail is the lifetime broadening. It can be expected that the lifetime is different for about everyone of the 600 final states. The states at higher energy can lose energy by Coster-Kronig-like Auger decay to lower states, and the other decay routes will be different also. This problem relates to the more general question of the coupling of core-hole creation and decay, and its influence on the spectral shape of the different spectroscopic techniques. The answer will have to be formed by a combination of normal x-ray absorption and x-ray photoemission with "resonance" experiments, in which the x-ray energy is scanned through the $L_{2,3}$ XAS energy range, and the resulting x-ray-emission spectra,[24] Auger spectra,[25] and/or photoemission spectra are measured.

VI. CONCLUDING REMARKS

We have shown that the atomic multiplet approach with the inclusion of the cubic crystal field reproduces the metal 2p x-ray-absorption spectra of 3d transition-metal fluorides. For more covalent compounds, such as oxides, the presented spectra are probably less accurate, although this remains to be checked. As discussed, this can be improved upon by an effective reduction of the 3d-3d Coulomb interactions. By comparison to experiment an accurate measure of the crystal-field-strength parameter $10Dq$ can be obtained. In fact, the final-state value of $10Dq$ is found, which can be different from the "initial"-state values that are found by optical spectroscopy. A study of this would be of quite some interest.

The field of application of the atomic multiplet plus crystal-field approach as presented here will probably be limited to the more ionic 3d transition-metal compounds. For the pure metals and alloys, band-structure effects may be of equal or greater importance than the atomic multiplet effects.[20] A systematic experimental study of band-versus-atomic effects would be of great interest in this regard.

ACKNOWLEDGMENTS

We are grateful to C. T. Chen and Francesco Sette for making available their unpublished results of the

transition-metal fluorides, taken with the high-resolution Dragon monochromator. This study was supported in part by the Dutch Foundation for Chemical Research [Stichting Scheikundig Onderzoek in Nederland (SON)] with financial assistance of the Netherlands Organization for Scientific Research [Nederlandse Organisatie voor wetenschappelijk Onderzoek (NWO)], and by the Committee for the European Development of Science and Technology (CODEST) Program.

[1]A resolution up to 1:10 000 is reached by the Dragon monochromator at Brookhaven National Laboratory (Upton, NY): C. T. Chen, Nucl. Instrum. Methods A **256**, 595 (1987). Other high-resolution monochromators in the 300–800-eV range include the SX700 at BESSY, Berlin: H. Petersen, *ibid.* **246**, 260 (1986); and the 10-m-focal-length grazing-incidence monochromator at the Photon Factory: H. Maezawa, S. Nakai, S. Mitani, A. Mikuni, T. Namioka, and T. Sasaki, *ibid.* **246**, 310 (1986).

[2]T. Yamaguchi, S. Shibuya, and S. Sugano, J. Phys. C **15**, 2625 (1982), T. Yamaguchi, S. Shibuya, S. Suga, and S. Shin, *ibid.* **15**, 2641 (1982).

[3]S. Gasiorowicz, *Quantum Physics* (Wiley, New York, 1974), Chap. 22.

[4]The use of DFT for x-ray absorption is worked out in J. E. Müller and J. W. Wilkins, Phys. Rev. B **29**, 4331 (1984).

[5]C. R. Natoli and M. Benfatto, J. Phys. Colloq. **47**, C8-11 (1986).

[6]The theoretical basis for this method can be found in R. D. Cowan, J. Opt. Soc. Am. **58**, 808 (1968), and R. D. Cowan, *The Theory of Atomic Structure and Spectra* (University of California Press, Berkeley, 1981).

[7]R. D. Cowan, *The Theory of Atomic Structure and Spectra* (University of California Press, Berkeley, 1981), p. 464, and references therein.

[8]See, e.g., C. J. Ballhausen, *Introduction to Ligand Field Theory* (McGraw-Hill, New York, 1962).

[9]P. H. Butler, *Point Group Symmetry, Applications, Methods and Tables* (Plenum, New York, 1981).

[10]J. R. Derome and W. T. Sharp, J. Math. Phys. **6**, 1584 (1965).

[11]P. H. Butler and B. G. Wybourne, Int. J. Quantum Chem. **10**, 581 (1976).

[12]F. M. F. de Groot, J. C. Fuggle, B. T. Thole, and G. A. Sawatzky, Phys. Rev. B **41**, 928 (1990).

[13]S. Sugano, Y. Tanabe, and H. Kamimura, *Multiplets of Transition Metal Ions in Crystals* (Academic, New York, 1970), Chap. 5.1.

[14]For the late 3*d* transition metals, the Lorentzian broadening of 0.1 eV is too small, as only lifetime effects will cause a larger broadening. See, e.g., J. C. Fuggle and S. Alvarado, Phys. Rev. A **22**, 1615 (1980), and references therein.

[15]C. T. Chen and F. Sette (private communication).

[16]R. D. Cowan, Ref. 7, p. 403.

[17]We have made several observations of such effects in cooperation with various other groups, and these will be published in the near future.

[18]B. T. Thole and G. van der Laan, Phys. Rev. B **38**, 3158 (1988).

[19]F. M. F. de Groot (unpublished).

[20]J. Fink, Th. Müller-Heinzerling, B. Scheerer, W. Speier, F. U. Hillebrecht, J. C. Fuggle, J. Zaanen, and G. A. Sawatzky, Phys. Rev. B **32**, 4899 (1985); J. Zaanen, G. A. Sawatzky, J. Fink, W. Speier, and J. C. Fuggle, *ibid.* **32**, 4905 (1985).

[21]J. Zaanen, C. Westra, and G. A. Sawatzky, Phys. Rev. B **33**, 8060 (1986).

[22]C. K. Jorgensen, *Absorption Spectra and Chemical Bonding in Complexes* (Pergamon, Oxford, 1962), Chap. 8.

[23]F. M. F. de Groot *et al.* (unpublished).

[24]J.-E. Rubensson, D. Mueller, R. Schuker, D. L. Ederer, C. H. Zhang, J. Jia, and T. A. Callcott, Phys. Rev. Lett. **64**, 1047 (1990).

[25]D. D. Sarma, C. Carbone, P. Sen, and W. Gudat, Phys. Rev. B **40**, 12 542 (1989).

[26]A. F. Wells, *Structural Inorganic Chemistry*, 4th ed. (Clarendon, Oxford, 1975), pp. 350–355, and references therein.

3.5. Spin-orbit coupling and non-cubic symmetries

In sections 3.2 to 3.4 the ground state of the partly filled $3d$-band is assumed not to be influenced by the $3d$-spin-orbit coupling. In this section the limits of this approximation are investigated. The treatment of the $3d$-spin-orbit coupling in the crystal field multiplet program are discussed and arguments are given concerning the actual physical effects of the spin-orbit coupling.

For the projection of the spin symmetries from spherical to cubic symmetry the same branching rules as for the angular momentum apply. Compounds with an even number of $3d$ electrons have an integer spin and the branching rules as given in table 3.4 can be used. For compounds with an odd number of $3d$ electrons the spin will be 1/2, 3/2 or 5/2. The atomic $S = 1/2$ state projects to E_1-symmetry in a cubic crystal field. Similarly $S = 3/2$ projects to G-symmetry and $S = 5/2$ is split into states of E_2-symmetry and of G-symmetry.

state	symmetry	spin-projection	overall symmetry	degeneracy
$3d^1$	$^2T_2$	E_1	$E_2 + G$	2
$3d^2$	$^3T_1$	T_1	$E + T_1 + T_2 + A_1$	4
$3d^3$	$^4A_2$	G	G	1
$3d^4_{HS}$	^5E	$E + T_2$	$A_1 + A_2 + E + T_1 + T_2$	5
$3d^4_{LS}$	$^3T_1$	T_1	$E + T_1 + T_2 + A_1$	4
$3d^5_{HS}$	$^6A_1$	$G + E_2$	$G + E_2$	2
$3d^5_{LS}$	$^2T_2$	E_1	$E_2 + G$	2
$3d^6_{HS}$	$^5T_2$	$E + T_2$	$A_1 + E + 2 \cdot T_1 + 2 \cdot T_2$	6
$3d^6_{LS}$	$^1A_1$	A_1	A_1	1
$3d^7_{HS}$	$^4T_1$	G	$E_1 + E_2 + 2 \cdot G$	4
$3d^7_{LS}$	^2E	E_1	G	1
$3d^8$	$^3A_2$	T_1	T_2	1
$3d^9$	^2E	E_1	G	1

Table 3.7: Effects of spin-orbit coupling on $3d^N$ ground state

If the $3d$ spin-orbit coupling is taken into consideration, the overall symmetry of the spin plus the angular momentum must be determined. In spherical symmetry this is accomplished by multiplying L with S to all possible J's. Similarly in cubic symmetry the irreducible representations of the spin must be multiplied with those of the angular momentum. Table 3.7 gives the results for the low-spin and high-spin configurations of all $3d^N$ states. It can be seen that in cubic symmetry the multiplicity of the spin (2S+1) does not directly relate to the total number of states. For example the $^5T_2$ state is split in six (and not in five!) different states. The crystal field multiplet program uses in all cases the branchings for both spin and angular momentum and thus the overall symmetries of the states as given in table 3.7. If the $3d$ spin-orbit coupling is neglected all states with the same angular symmetry are degenerate because the spin in itself does not influence the energy of

the state.

3.5.1. Effects of 3d spin-orbit coupling

$3d$ spin-orbit coupling has a large effect on partly filled t_{2g} states, that is the ground states of the $3d^1$, $3d^2$, $3d^4_{LS}$, $3d^5_{LS}$, $3d^6_{HS}$ and $3d^7_{HS}$ symmetries. The effects on states of E-symmetry are considerably smaller [12]. The difference in effect on T_2-states respectively E-states is directly related to the way in which a t_{2g}, respectively an e_g wavefunction is build from the atomic wavefunctions. As has been shown in table 3.3 an e_g wavefunction can be build from $m_l = 0$ or 2 (or -2) functions. A spin-orbit coupling effect can only affect states which differ by one in their m_l-value, hence in first order the e_g states are not affected, in contrast to the t_{2g} states (See for example Ref. 12 for the mathematical details). Spin-orbit coupling does not affect states of A_1 or A_2 symmetry.

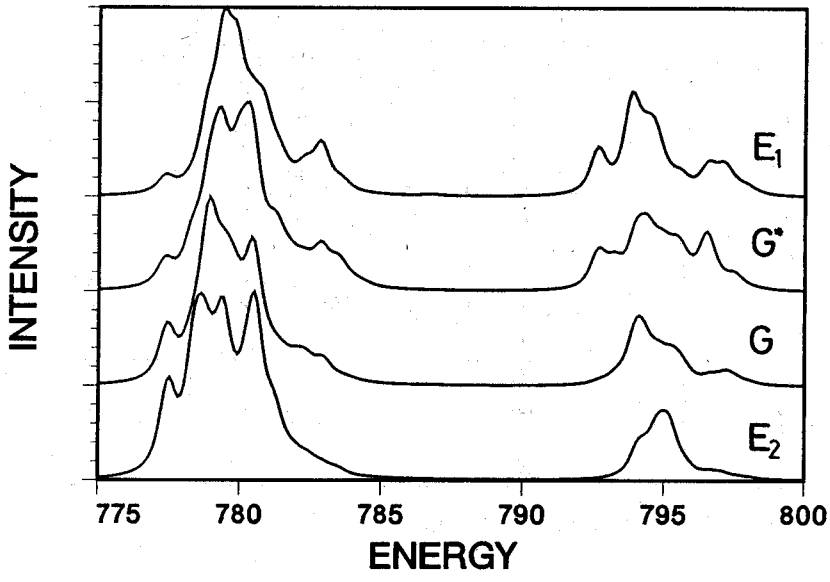

Figure 3.11: Theoretical x-ray absorption spectra for the $3d^7_{HS}[\Gamma_i] \rightarrow 2p^5 3d^8$ transition for the four different $3d$ spin-orbit split symmetries of the $^4T_1$ ground state. The respective symmetries are from bottom to top: E_2, G, G^* and E_1.

The magnitudes of the $3d$ spin-orbit coupling of the $3d$-metal ions were given in section 3.3. Because the spin-orbit coupling strength increases with the atomic number, the best case to investigate the effect of $3d$ spin-orbit coupling is the $3d^7_{HS}$ configuration. The $3d^7_{HS}$ ground state configuration is found in for example CoF_2 and CoO. In section 3.4 the CoF_2 spectrum is compared with a crystal field multiplet calculation in which the $3d$ spin-orbit coupling is neglected. From table 3.7 it is found that if $3d$ spin-orbit coupling

is included, the ${}^4T_1$ ground state of the $3d^7_{HS}$-configuration splits in four states of E_1, E_2 and two times G-symmetry. The actual multiplet calculation with the atomic value of the $3d$ spin-orbit coupling (83 meV) and a cubic crystal field strength of 0.9 eV gives the four states at energies of respectively 0 (E_2), 44 meV (G), 115 meV (G^*) and 128 meV (E_1). Figure 3.11 gives the crystal field multiplets of the $3d^7_{HS}[\Gamma_i] \rightarrow 2p^5 3d^8$ transition for the four different symmetries. Given this spread in the initial states, the room temperature (25 meV) spectrum is dominated by the lowest state of E_2-symmetry, with a 17% contribution of the first excited state of G-symmetry.

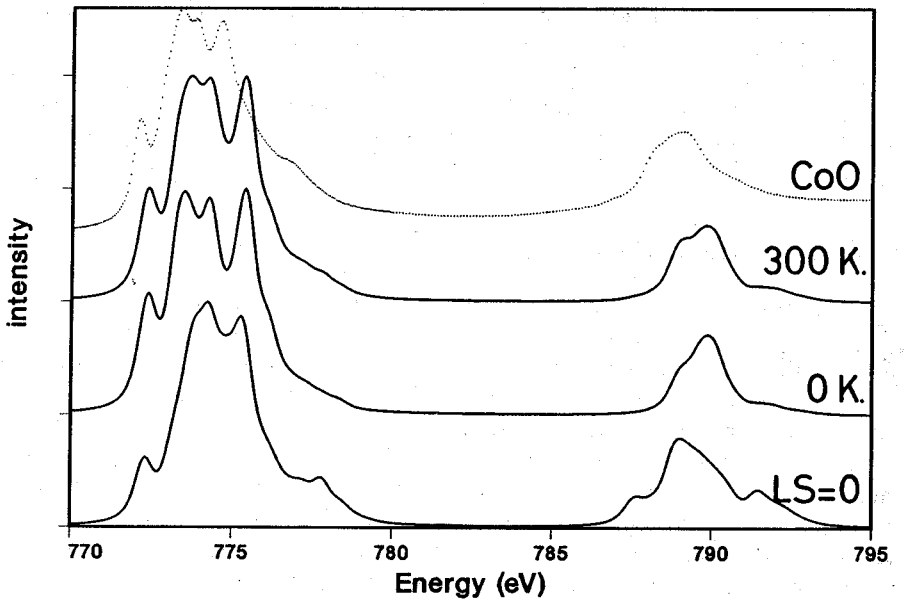

Figure 3.12: Comparison of the theoretical spectra of (from bottom to top) (a) the spectrum under neglect of $3d$ spin orbit coupling, (b) the ground state, and (c) the spectrum at 300 Kelvin, with the experimental spectrum of CoO.

Figure 3.12 gives the theoretical spectra corresponding respectively to the ground state E_2 spectrum, the 300 Kelvin spectrum and the spectrum under neglect of $3d$ spin-orbit coupling. It is clear that the inclusion of the $3d$ spin-orbit coupling enhances the agreement considerably. The good agreement between theory and experiment makes it possible to determine the energies of the low-lying excited states from an analysis of the experimental spectrum, preferably measured for a series of temperatures. Hence it can be concluded that in potential temperature dependent x-ray absorption experiments can reveal the magnitude of the $3d$ spin-orbit coupling (which can different from the atomic value).

Above it has been shown that the $3d$ spin-orbit coupling has a detectable influence on the spectral shape of divalent cobalt $3d^7_{HS}$-compounds. Another configuration which is influenced considerably is $3d^4_{LS}$, which has ${}^3T_1$-symmetry and splits in four states if the $3d$

spin-orbit coupling is included. The trivalent manganese oxides have a $3d^4$ ground state. In these compounds the cubic crystal field strength is approximately equal to the effective exchange splitting which places the trivalent manganese oxides close to the high-spin low-spin transition point. As a result of $3d$ spin-orbit coupling the low-spin $^3T_1$-state splits in four and the high-spin ^5E-state splits in five though its actual splittings will be small. In table 3.7 it can be checked that the overall symmetries of the spin-orbit split high-spin and low-spin states contain E, T_1, T_2 and A_1 irreducible representations. Hence, if the high-spin and low-spin states are close to degenerate these representations are allowed to form bonding and anti-bonding admixtures. The spin-state of these combinations (thus of the ground state) will not be pure high-spin (S=2) or low-spin (S=1) but have an effective spin-state with S in between 1 and 2. This concept will be used in section 4.3 to explain the spectral shape of the manganese $2p$ x-ray absorption spectrum of $LiMnO_2$. The formation of admixtures of spin states has been used also in a study of iron phthalocynanine ($3d^5$ in a D_{4h} point group) by Thole et al. [84].

3.5.2. Effects of non-cubic symmetries

Another type of low-energy splittings of the crystal field multiplet is caused by distortions from cubic symmetry. A difference can be made between initial state effects and final state effects. Initial state splittings can be important for room temperature experiments if they are of the order of 25 meV. Final state effects will be visible only if they cause spectral changes over an energy range of about 200 meV or more (depending on the specific multiplet, amount of covalency, etc). From this consideration it might be expected that initial state effects of symmetry distortions from cubic symmetry will cause large spectral changes in almost all compounds. However if the actual effects of the lower crystal fields on the spectral shapes are studied it is found that even if a symmetry distortion causes initial state splittings of the order of 100 meV, the spectral shape of the ground state is hardly modified from the spectral shape of the ground state of the non-distorted spectrum. Hence in order to show a visible effect on the spectral shape the demand of initial state splittings of the order of 25 meV is in itself not enough to cause spectral changes, and considerably larger splittings are needed. In this respect it is important to notice that a splitting of 50 meV will show drastic effects on the spectral shape if caused by $3d$ spin-orbit coupling, but the same splitting will cause hardly any effect if caused by distortions from cubic symmetry.

Large initial state effects of lower symmetries are found if the cubic $3d^N$ ground state contains a partly filled e_g band. Elongation of the z-axis lifts the degeneracy of the e_g orbitals: the Jahn-Teller effect [85]. A similar effect occurs in case of a partly filled t_{2g}, but the energy effects of the tetragonal distortion are larger for partly filled e_g-states. (Notice that in contrast $3d$ spin-orbit coupling has a considerably larger effect on partly filled t_{2g}-states) Partly filled e_g states occur for $3d^4_{HS}$, $3d^7_{LS}$ and $3d^9$. The effects on the $3d^4_{HS}$-state are well-known for divalent chromium-compounds. As discussed above in the trivalent manganese oxides the high-spin and low-spin configuration are close to degenerate, and the Jahn-Teller distortion of the high-spin state will further complicate the analysis (see the discussion of $LiMnO_2$ in section 4.3). The $3d^7_{LS}$-configuration does not occur as such and for

example the 'low-spin like' trivalent nickel compounds are dominated by $3d^8\underline{L}$-character (see chapter 4). The tetragonal distortion (or in other words the square planar surrounding) of the $3d^9$-configuration is well known, for example in the CuO-based high T_C superconductors.

Final state effects of lower symmetries can be important for all $3d^N$ configurations if the site geometry is strongly distorted from cubic. Final state effects of lower symmetries are best observable for $3d^0$-compounds due to their simple spectral shape in which all multiplet transitions are resolved as individual peaks. In rutile (TiO_2) the site symmetry of titanium is D_{2h} and the effective configuration is $3d^0$. Effects of the symmetry reduction can be expected for the $2p^5e_g^1$-like states and indeed the rutile spectrum (given in section 3.3) clearly shows a splitting of the e_g-peak which is reproduced in a calculation for D_{4h}-symmetry.

Similar final state effects of lower symmetries are expected for systems with a partly filled $3d$-band. However it can be argued that crystal field effects, including distortions from cubic symmetry, are more important for early $3d$-metal oxides compared with the late $3d$-metal oxides. The important parameters are the radial extend of the wavefunctions of the $3d$-electrons (r_ϕ) and the inter-atomic distances (R). It is known that the ratio r_ϕ/R decreases in the 3-metal series [86,87], and especially in systems with one or more occupied e_g orbital, relatively large inter-atomic distances are found [88]. Crystal field effects scale with r_ϕ/R, hence effects of lower symmetries (and also the cubic crystal field strengths) are largest for the early $3d$-metals.

Branching rules for lower symmetries

The crystal field multiplet program can handle any point group symmetry. As an example, the branching rules of a D_{2h} point group are given in figure 3.13. The projection from spherical symmetry to D_{2h} symmetry is accomplishes in three steps. First the symmetry is reduced to cubic, in the second step the cubic (O_h) to tetragonal (D_{4h}) symmetry reduction is included and the third step goes to D_{2h} symmetry. The necessary extra crystal field terms in the Hamiltonian can be deduced directly from this figure: The Hamiltonian has A_1-symmetry, thus all branchings to A_1-symmetry take part in the Hamiltonian. For cubic symmetry, apart from the S-state, the G-state projects to the A_1-state. This $G \rightarrow A_1$ branching describes the inclusion of cubic crystal field term in the Hamiltonian. Similarly for tetragonal symmetry the cubic E-state projects to the A_1-state. In turn the cubic E-state has two parent states in spherical symmetry, hence there are two additional paths $D \rightarrow E \rightarrow A_1$ and $G \rightarrow E \rightarrow A_1$. In other words there are two additional crystal field parameters in the Hamiltonian of D_{4h} symmetry. The total number of crystal field parameters of a specific point group can be found directly from the total number of different paths leading to the A_1-symmetry state. It should be noticed that the 'route' to reach the D_{2h} point group is not uniquely defined, and instead of the route via O_h (as given in the figure) an alternative route via $D_{\infty h}$ can be chosen. The choice of the route determines the meaning of the crystal field parameters and because of the central place of the cubic crystal field strength, in general the route via O_h symmetry is used. The different branchings for all point groups and also all possible choices for the routes to reach a specific point group are given in Ref. 53.

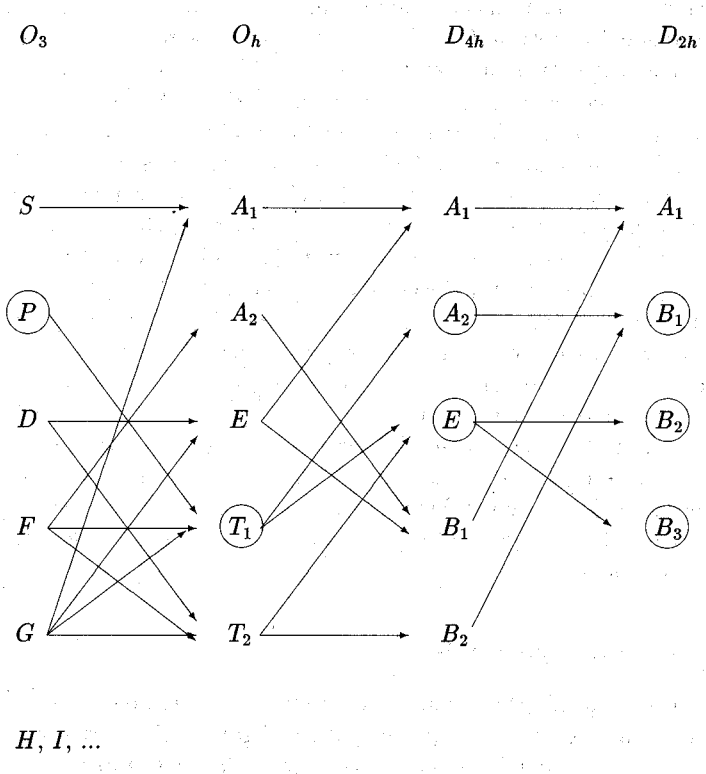

Figure 3.13: Schematic branchings from O_3-symmetry (atomic) to D_{2h}-symmetry, via O_h and D_{4h}. Encircled are all representations which can be reached from atomic P-symmetry. (Notice that this also describes symmetry effects on the polarization dependence of a dipole transition, see section 3.6).

3.6. Polarization dependence

In the foregoing the discussion has been limited to the total x-ray absorption cross section. The x-ray absorption spectrum however depends on the polarization of the incoming x-ray. The polarization dependence can be found directly from the angular part of the transition matrix elements. This angular part is (see equation 1.7 on page 7) given as the 3J-symbol:

$$\begin{pmatrix} J & 1 & J' \\ -M & q & M' \end{pmatrix} \tag{3.5}$$

The triangle relations of the 3J-symbol give $\Delta M = M' - M = -q$. With the use of this equation one tacitly assumes only dipole transitions to occur. Quadrupole transitions have possibly some effect on specific edges [89], but as far as the transition metal $2p$ edges are concerned they do not play any role.

As discussed in the experimental section synchrotron radiation is linearly polarized in the plane of the orbiting electrons and out of plane it is partly circularly polarized. If the x-ray impinges on a substrate under normal incidence linearly polarized light, sometimes denoted as s-polarized, can give rise to $\Delta M = +1$ or -1 transitions. Right circular polarized light ($q = -1$) allows $\Delta M = +1$ transitions and left circular polarized light decreases M by one. If the substrate is turned to grazing incidence the $\Delta M = \pm 1$ transitions decrease whereas $\Delta M = 0$ transitions increase.

Dichroism

The difference between normal incident and grazing incident spectra taken with linear polarized x-rays is usually denoted as (linear) x-ray dichroism. Circular dichroism is the difference between the absorption of left and right polarized x-rays under normal incidence. The condition for the occurrence of polarization dependence is a macroscopic asymmetry in the electronic and/or magnetic structure. thus non-magnetic crystals with a cubic symmetry do not show any polarization dependence because they have inversion symmetry and their x, y and z directions are equivalent. Also a non-magnetic (random) polycrystalline solid is symmetric and dichroism is prohibited by selection rules. Therefore either single crystals or oriented polycrystalline materials must be used for dichroism experiments.

The symmetry criterion which determines a possible polarization dependence is given by the space group of the crystal and not by the point group of the atom. This can be illustrated with system which has a cubic space group but in which the atom which absorbs the x-ray has a tetragonal point group (hence the elongated direction of the tetragonal point group is for some atoms directed along the x-axis, but for others along the y-axis respectively the z-axis). In this case the spectral shape is determined by the point group, however no dichroism is found because the potentially dichroic effect of the three differently oriented atoms cancels each other exactly [90]. The actual polarization dependence of all space groups can be deduced directly from the symmetry branching rules as were given in the foregoing section (figure 3.13). The polarization dependence is determined by the splittings of the irreducible representation of the dipole transition which is P-like (Δ J = +1,-1 or 0) in the atom. From figure 3.13 it can be checked that in octahedral symmetry no polarization dependence can occur, in contrast to tetragonal symmetry. For a D_{2h} space group there are three different representations (directions), which can be denoted as trichroism [90]. From this figure it is clear that the polarization dependence of quadrupolar transitions (which have atomic D-symmetry) is different, and already in octahedral symmetry polarization dependence occurs.

Linear dichroism can be caused by both electric and magnetic effects, but electric fields (such as the crystal fields) can never cause a difference between the $\Delta M = -1$ and $\Delta M = +1$ transitions. This is a direct consequence of Kramer's theorem [91] which states that the

lowest state in a static electric field is always at least twofold degenerate. The only way to break the degeneracy of the Kramer's doublet is by means of a time asymmetric field (such as a magnetic field). Thus crystal field effects can only cause linear dichroism whereas magnetic effects can also cause circular dichroism.

The potential use of polarization dependent x-ray absorption experiments is illustrated with examples from non-cubic compounds, surfaces and adsorbates, and magnetic materials.

3.6.1. Non-cubic compounds

Non-cubic compounds contain at least one axis which is distinguishable from the others, hence the x-ray absorption spectra are polarization dependent with respect to this axis. Both $BaCoF_4$ and TiO_2 are non-cubic and their polarization dependent x-ray absorption spectra are discussed.

Cobalt 2p x-ray absorption of $BaCoF_4$

$BaCoF_4$ crystallizes in a $C_{2v}^{12}(A_{2_1am})$ space group [92]. Along the [001] direction (a-axis) a macroscopic electric polarization has been found, which can be reversed by reordering the CoF_4-sheets. At room temperature $BaCoF_4$ is ferroelectric and paramagnetic. Below $T_N = 68$ Kelvin it is antiferromagnetic [92]. Given these properties it is expected that $BaCoF_4$ shows an x-ray dichroism effect with respect to the a-axis. In principle the C_{2v}-symmetry allows for a further dichroic behaviour of the b-axis with respect to the c-axis, which is not considered here. Figure 3.14 shows the cobalt $2p$ x-ray absorption spectra taken at three different temperatures and for $E \perp a$ and for $E \parallel a$. A clear linear dichroism is observed, which furthermore shows a clear temperature dependence.

Crystal field multiplet calculations have been performed to simulate the spectra. For the calculations the Co^{II}-ions are described with a $3d^7_{HS}$ ground state. The Slater integrals as given in section 3.4 have been used. In section 3.5 it was shown that $3d$ spin-orbit coupling is important for divalent cobalt and hence it is included in the calculations. The cubic crystal field is optimized and found to be 0.9 eV. The effects of lower symmetry are included as a tetragonal distortion. The possible effects of reduction to D_{2h}-symmetry have been neglected. The calculations are performed for the paramagnetic phase, hence no exchange splitting is included. Table 3.8 sketches the initial state effects of. in order of decreasing magnitude, the Slater integrals, the cubic crystal field, the $3d$ spin-orbit coupling, the tetragonal crystal field and the exchange field. The tetragonal crystal field does not split the E_2-symmetry ground state but it does affect the first excited state of G-symmetry. After inclusion of the tetragonal field the state is split and the two resulting states are called G_1 and G_2. In the crystal field multiplet calculation, which is optimized to simulate the 30 Kelvin spectra, the G_1 and G_2 are found at respectively 39 meV and 51 meV above the E_2 ground state. Assuming a Boltzmann distribution over the low-lying states this means that at 30 Kelvin these states are not populated but at 300 Kelvin their population is respectively 21% and 13%.

Figure 3.15 shows the calculated crystal field multiplet spectra for $E \parallel a$ ($\Delta M = \pm 1$) and $E \perp a$ ($\Delta M = 0$) for the 3 low lying states E_2, G_1 and G_2. Comparison of the crystal

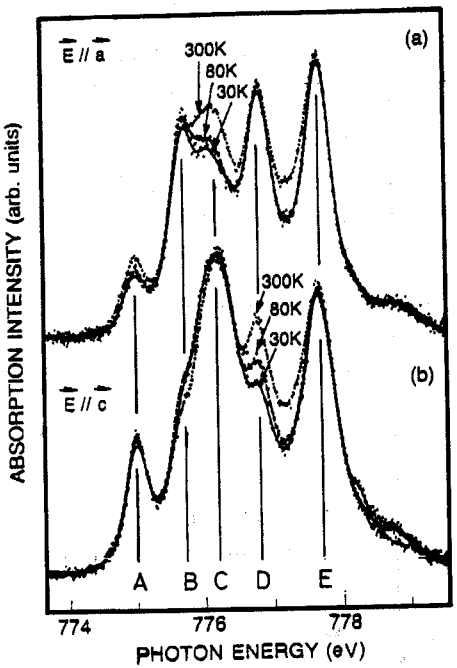

Figure 3.14: Cobalt 2p x-ray absorption spectra of $BaCoF_4$. The experiments were performed with the Dragon monochromator by B. Sinkovic et al. [93].

Ground state symmetry	Physical effect	Excited states symmetry	Ground state degeneracy
$3d^7$			120
↓	Slater integrals		
^4F		$+^4P, ^2P,$ etc	28
↓	cubic crystal field		
$^4T_1$		$+^4T_2, ^4A_2$	12
↓	$3d$ Spin-orbit coupling		
E_2		$+G, G^*, E_1$	2
↓	tetragonal crystal field		
E_2		but: $G \rightarrow G_1 + G_2$	2
↓	magnetic exchange field		
E_2^+		$+E_2^-$	1

Table 3.8: Splitting of the initial state multiplet of a $3d^7$-configuration. The tetragonal crystal field (or any other lower symmetry field) does not split the 'Kramers doublet' E_2 ground state, but the first excited state of G-symmetry is split.

field multiplet calculation with experiment shows that the main features, including the dichroism effects, are reproduced. Some minor discrepancies exist: The D peak is too high in the calculated $E \perp a$ spectrum (it is close to absent in the experimental 30 K spectrum)

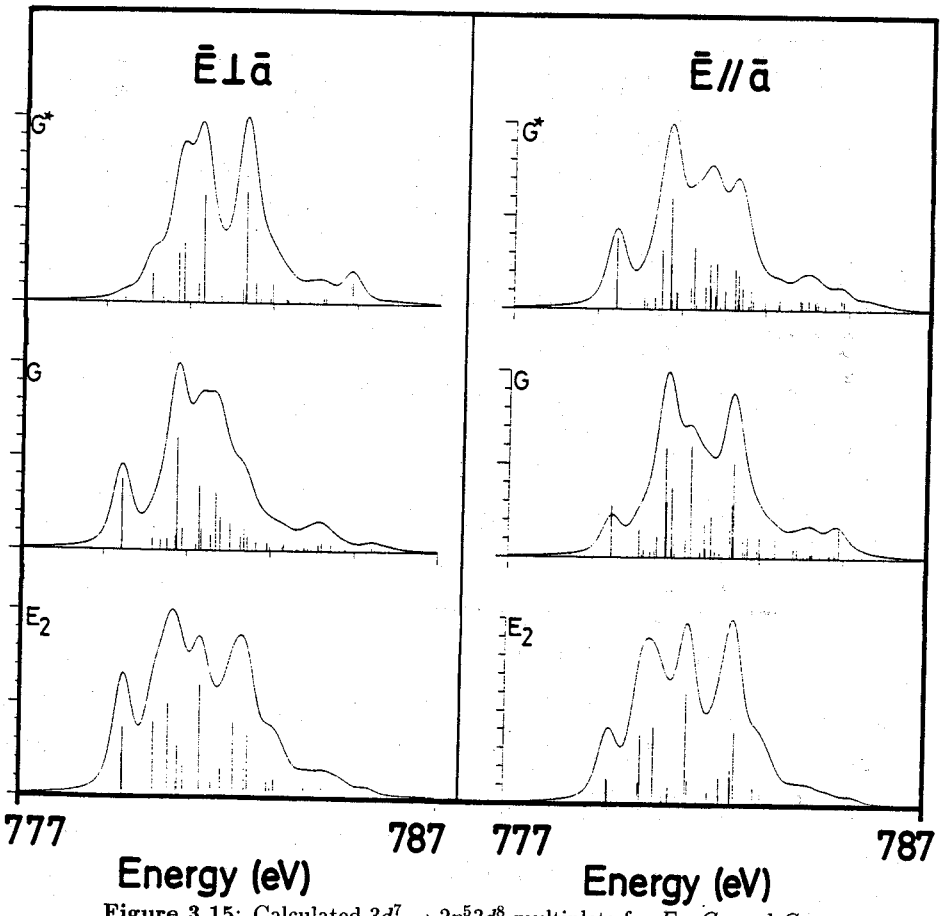

Figure 3.15: Calculated $3d^7 \rightarrow 2p^5 3d^8$ multiplets for E_2, G_1 and G_2.

and the E peak is too broad. As can be checked in figure 3.16, which gives the theoretical 30 Kelvin and 300 Kelvin spectra for $E \perp a$, the reversal of the asymmetry of peaks B and C is nicely reproduced. From the accuracy of the description the following conclusions can be drawn:

- The crystal field multiplet model is capable of reproducing the main features of the dichroism and its temperature dependence, despite uncertainties in the precise magnitudes of the parameters used (Slater integrals, crystal field couplings and $3d$ spin-orbit coupling).

- Above T_N the ground state of $BaCoF_4$ is a Kramer's doublet of E_2 symmetry with states originating from cubic G-symmetry at excitation energies in the range of kT, thereby creating a large temperature dependence between 80 Kelvin and 300 Kelvin. (From the present analysis it is not possible to be more precise about the exact energy

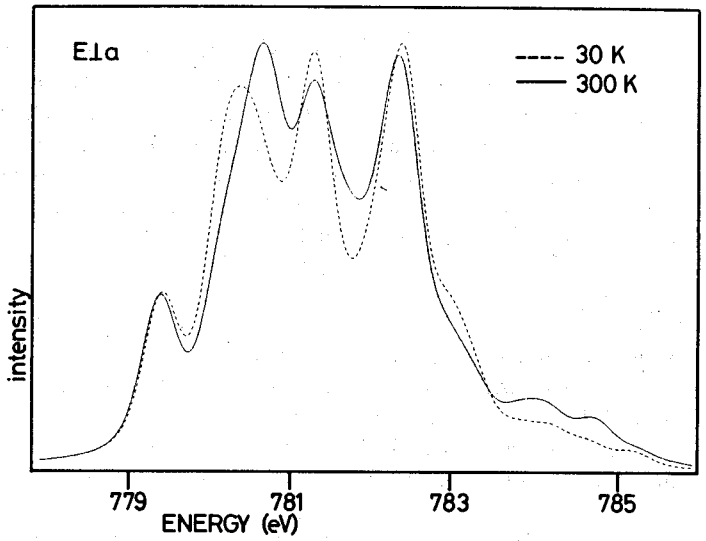

Figure 3.16: Calculated $3d^7 \rightarrow 2p^5 3d^8$ multiplet for $E \perp a$ for 30 Kelvin (dashed line) and 300 Kelvin (solid line).

differences and symmetries, also because the actual symmetry is D_{2h} and the symmetry lowering from D_{4h} influences the G states as well as the transition matrices).

- Below T_N an additional effect from the splitting of the Kramer's doublet occurs, which modifies the linear dichroism, and additionally causes circular dichroism effects.

More detailed temperature dependent measurements of B. Sinkovic et al. [94] reveal that above T_N the amount of linear dichroism, detected from specific peak-ratios, follows a smooth trend originating from population effects of excited states in agreement with the present analysis. At T_N a jump in the peak-ratios occurs which indicates the additional dichroic effect of the exchange splitting. The effects of the exchange splitting can be tested directly with use of circular polarised x-rays.

Titanium 2p x-ray absorption of TiO_2

TiO_2 has a D_{4h}^{14} space group symmetry in the rutile crystal structure and the point group of titanium is D_{2h}. Titanium has six oxygen neighbours, 2 at 1.98 Å and 4 at 1.94 Å, forming a quasi-tetragonal (D_{4h}) environment which is slightly distorted. The overall spectrum can be simulated with tetragonal crystal field parameters of the order of 0.75 eV. Thus the tetragonal symmetry distortion is strong and effects on the spectrum are clearly visible. From this observation one expects a large linear dichroism effect. However a closer look at the crystal structure of rutile reveals that there are two titanium sites which have their elongated axis rotated over 90°. Thus within the *ab*-plane the angular dependent effect of the tetragonal symmetry distortion, the main lower symmetry effect on the spectral shape, exactly cancels and no dichroism is expected. In principle a dichroism effect might

be expected because the c-axis is different from the ab-plane. However in experiments performed thus far no dichroism has been observed. In contrast to the $2p$ edge, the pre-edge region of the titanium $1s$ x-ray absorption spectrum of rutile shows a clear angular dependence [95, 96]. Angular dependent measurements within the ab-plane clearly reveal angular dependence of the quadrupolar transitions, for which the two (90° rotated) sites are in phase [90]. Thus from the angular dependence observed the leading peak is proven to be (at least partly) related to quadrupolar transitions [95].

3.6.2. Surfaces and adsorbates

A surface presents a clear breaking of the (x, y, z)-symmetry, and will therefore always present a rather large linear dichroism between polarizations in the surface plane and perpendicular to it. A linear polarized x-ray impinging perpendicularly upon a surface excites core electrons to bonds lying in the surface plane. A grazing incident x-ray excites exclusively bonds perpendicular to the surface plane, which can be used to determine the surface electronic structure.

A problem with electron yield is that due to its mean probing depth of the order of 30 Å , the surface signal is overwhelmed by the signal from the bulk. To separate the surface signal it is fruitful to use ion yield which, with its probing depth of only 1 or 2 layers, is a true surface probe. The combination of ion-yield and electron yield detection has been applied to the CaF_2-Si(111)-system. The paper included in section 5.4.1 confirms that it is indeed possible to pick out the surface signal with ion yield detection.

Surface dichroism effects are particularly useful for adsorbates. A nice example is given for the absorption of boron on a silicon (111) surface, for which the sharp boron π-peak, related to the silicon-boron bond, is visible solely with p-polarized x-rays [102]. Given that the adsorbates are present on the surface only, the x-ray absorption spectrum can be measured with any method [98, 99]. Because electron yield measurements are easier in their use, adsorbates are usually measured with (partial) electron yield. Besides an interest in the structure of the x-ray absorption edges, the surface extended x-ray absorption fine structure (SEXAFS) is important for the determination of for example the surface bond lengths [100]. The common procedure of analysis for the 'near edge structure' is by means of multiple scattering calculations. Emphasis is given to the complicated problem of correct determination of the surface structure [101]; the problems regarding the limitations of the one-electron approach are generally not considered. Specifically if a $3d$-metal surface (or adsorbate) is analysed the applicability of one-electron like models, like multiple scattering, is doubtful.

3.6.3. Magnetic materials

As has been discussed magnetic fields can cause linear as well as circular dichroism. Because circular dichroism effects can not be caused by symmetry effects from surfaces and crystal fields they present a direct measure of the magnetic structure of materials. Circular dichroism has been studied in the hard x-ray range by the groups of G. Schütz [103, 104] and A. Fontaine / E. Dartyge [105], and clear magnetic circular dichroism (MCD) effect have been

found for the $L_{2,3}$ of rare earths and the K edges of $3d$-metals. Recently it became possible to extend the circular dichroism experiments to the soft x-ray range and as yet some rare earth $M_{4,5}$ edges [106–108] and $3d$-metal $L_{2,3}$ edges [108,109] have been measured.

For the interpretation of the MCD effects the common methods to explain the x-ray absorption spectra have been extended to include magnetic fields:

- The band structure approach, mainly used for the metal K edges and rare earth $L_{2,3}$ edges, has been modified to perform spin-dependent relativistic calculations by Ebert et al. [110].
- The multiple scattering method has been modified by C. Brouder et al. [111].
- The circular dichroism of the atomic multiplet spectra of rare earth $M_{4,5}$ edges has been analysed by J. Goedkoop [112], using the results of B.T. Thole, and also by Imada and Jo [113].
- G. van der Laan and B.T. Thole calculated all MCD spectra for the $L_{2,3}$ edges of transition metal compounds in cubic crystal fields [114].
- The MCD spectrum of nickel has been explained with a band structure approach with empirically optimized exchange and spin-orbit values [115], and also with an Anderson impurity model (including the crystal field multiplet) [116].

In the crystal field multiplet approach the addition of a magnetic field splits the Kramer's doublet. Mathematically the symmetry is reduced from cubic symmetry to C_4 symmetry via the branching $O_h \rightarrow D_{4h} \rightarrow D_4 \rightarrow C_4$ with inclusion of an exchange splitting in the z direction. As the effects of crystal field symmetry reduction have been neglected in Ref. 114, the linear dichroism spectra apply to pure octahedral symmetry only. The discussion of the linear dichroism of $BaCoF_4$ in the last section reveals that the inclusion of lower symmetries is crucial for the correct description of linear dichroism effects.

Magnetic effects on linear dichroism

Magnetic effects generate circular dichroism, but additionally they can have a large effect on the linear dichroism of rare earth $M_{4,5}$-edges as was first shown by van der Laan et al. [117]. The basic reason is the strong correlation between ΔM_J and ΔJ transitions as a result of the properties of the 3J-symbol (equation 3.5). Under the assumption that only the $M_J = -J$ magnetic level of the ground state is filled, this correlation is given in table 3.9.

Because the J-values for the rare earths are found to be in between 5/2 and 8, the correlation is rather strong and $\Delta J = \pm 1$ transitions are almost exclusively correlated with $q = \Delta M_J = \pm 1$ transitions. The polarization averaged spectrum is formed from a combination of all transitions from the $4f^N$ ground state of specific J to all $3d^9 4f^{N+1}$ final states of $J+1$, J and $J-1$. Figure 3.17 shows the atomic multiplet spectrum for Tm^{3+}.

The M_5 edge has three possible transitions, the first one with $\Delta J = 0$ (dashed line) and the two others with $\Delta J = -1$ (chain-dotted line) Due to the Jq-correlation the transitions to $\Delta J = -1$ are solely visible in the $q = \pm 1$ spectrum, and the $\Delta J = 0$ transition is largely

$(\Delta M_J = -q)$ / ΔJ	-1	0	$+1$
-1	1	0	0
0	$\frac{1}{J+1}$	$\frac{J}{J+1}$	0
$+1$	$\frac{1}{(2J+3)(J+1)}$	$\frac{2J+1}{(2J+3)(J+1)}$	$\frac{(2J+1)(J+1)}{(2J+3)(J+1)}$

Table 3.9: Correlation between ΔJ and ΔM_J

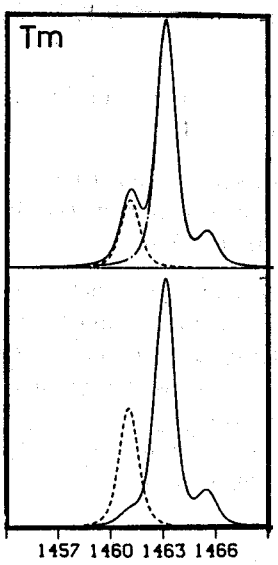

Figure 3.17: Atomic multiplet calculation of M_5 edge of thulium. Top spectrum: dashed line corresponds to $\Delta J = 0$ and chain-dotted line to $\Delta J = -1$. Bottom spectrum: the resulting spectra for $E \perp M$ (dashed) and $E \| M$ (solid).

restricted to $q = 0$ polarized x-rays. The small low-energy shoulder in the $q = \pm 1$ spectrum is an effect of the incomplete correlation. The linear and circular dichroism of the $M_{4,5}$ spectra of all rare earths, including the effects of finite temperature, have been given in Ref. 112. It has been shown experimentally that magnetic effects indeed cause a large linear dichroism [112, 118], though in some cases it is difficult to distinguish the magnetic effects from the electrostatic (surface) effects [112, 119, 120]

3.7. Multiplets and hybridization

The crystal field multiplet calculations assume the ground state to be represented by a single $3d^N$-configuration. This configuration is found from the atomic multiplet calculation and

$(\Delta M_J = -q)$ / ΔJ	-1	0	$+1$
-1	1	0	0
0	$\frac{1}{J+1}$	$\frac{J}{J+1}$	0
$+1$	$\frac{1}{(2J+3)(J+1)}$	$\frac{2J+1}{(2J+3)(J+1)}$	$\frac{(2J+1)(J+1)}{(2J+3)(J+1)}$

Table 3.9: Correlation between ΔJ and ΔM_J

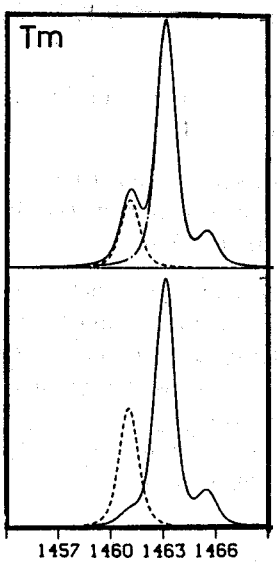

Figure 3.17: Atomic multiplet calculation of M_5 edge of thulium. Top spectrum: dashed line corresponds to $\Delta J = 0$ and chain-dotted line to $\Delta J = -1$. Bottom spectrum: the resulting spectra for $E \perp M$ (dashed) and $E \| M$ (solid).

restricted to $q = 0$ polarized x-rays. The small low-energy shoulder in the $q = \pm 1$ spectrum is an effect of the incomplete correlation. The linear and circular dichroism of the $M_{4,5}$ spectra of all rare earths, including the effects of finite temperature, have been given in Ref. 112. It has been shown experimentally that magnetic effects indeed cause a large linear dichroism [112, 118], though in some cases it is difficult to distinguish the magnetic effects from the electrostatic (surface) effects [112, 119, 120]

3.7. Multiplets and hybridization

The crystal field multiplet calculations assume the ground state to be represented by a single $3d^N$-configuration. This configuration is found from the atomic multiplet calculation and

its projections to cubic symmetry. The errors introduced in this approach are known to be not negligible. The errors are all related to the fact that the actual ground state is not single configurational but contains an admixture of a series of configurations. In an atom a number of excited configurations can be included in multi-configurational Hartree-Fock calculations. In a solid the most obvious extension is to account for hybridizational effects by means of the admixture of extra-atomic configurations such as the charge transfer states $3d^{N+1}\underline{L}$, etc. In this section some of the possible extensions of the crystal field multiplet model are discussed.

Multi-configurational atomic multiplet calculations

The obvious extension of the calculational scheme is to include excited configurations in a configuration interaction calculation. The situation is not favourable for actual calculations because there are an infinite number of small effects. Theoretical studies indicate that it is possible to approximate the infinite series of excited configurations with a single configuration which has an equivalent LS-dependence as the ground state but an opposite sign [121–124]. This finding gives a partial justification of the reduction of the Hartree-Fock values of the Slater integrals to 80% of their original values [125].

A recent effort to overcome these problems and to actually perform a multi-configurational calculation has been made by Sarpal et al. [126]. Using a multi-configurational Dirac-Fock (= relativistic Hartree-Fock) calculational scheme, the $M_{4,5}$ edges of divalent samarium and thulium atoms were calculated. The advantage of these configuration interaction calculations is that no parameter adjustments are necessary. However from comparison with experiment it appears that for the multi-configurational spectrum the agreement is not perfect and even more the (reduced) Hartree-Fock result from Thole et al. [127] compare far better with the experimental spectrum. Figure 3.18 shows the multi-configurational result in comparison with experiment. The result from Ref. 127 is given at the top This indicates that the correct configuration-interactional solution of the atomic multiplet spectra is as yet not found. Hence, for practical purposes the reduced Slater integral approach is preferred, especially because of its transparent computational method.

The effects of hybridization in solids

In contrast to atoms where an improvement was found in a more rigorous multi-configurational treatment to avoid empirical parameter adjustments, for solids the multiplet calculations are embedded in model Hamiltonians to account for solid state effects. For solids the number of possible effects on the actual ground state increases. Apart from intra-atomic configuration interaction effects, there are effects from extra-atomic hybridization. In this context it is by no means guaranteed that the intra-atomic configuration interaction effects are equal to those in the atom, if it is possible at all to separate the intra-atomic effects from extra-atomic effects.

Lynch and Cowan used an approach in which they reduced the Slater integrals from their atomic values. To simulate the hybridization of ligand character $|L\rangle$ into the original atomic $|4f\rangle$ wavefunction the ff-Slater integrals were reduced by 20% and the df-Slater

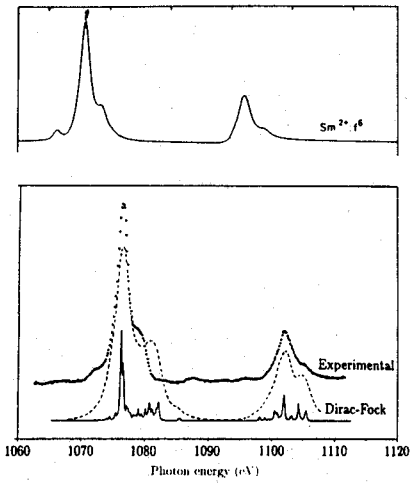

Figure 3.18: Top: Scaled down Hartree-Fock calculation from Thole et al. [127]; bottom: experimental Sm^{2+} spectrum compared with multi-configurational Dirac-Fock calculation from Sarpal et al. [126].

integrals by 10% (as the core state are not modified in a solid) [128]. Their results on the $M_{4,5}$ edges of Ce^{3+} and Pr^{3+} showed a complex reordering of states as result of the Slater integral reduction. The method of reducing the Slater integrals is rather limited and effects like extra broadenings and satellites are not reproduced. Also the intrinsic approximation is used that the radial wavefunction are identical for all states.

An alternative approach to include covalency effects is to implement the multiplet calculation into an Anderson impurity model. This model has been developed (for spectroscopy) by Gunnarsson and Schönhammer [129,130] and was used extensively to study the core level spectra of cerium [131–135]. The groups of Kotani and Jo [136–142] used the Anderson impurity method to account for both the atomic multiplets and the interaction of the localized levels with bands, and they have been able to simulate the cerium x-ray absorption and x-ray photoemission spectra with great success. The basic idea of the Anderson impurity model is to describe the effects of the interaction (V_{fk}) of a correlated localized state (ε_f) with a non-correlated band ($\sum_k \varepsilon_k$). The electron correlation shifts the localized state to higher energy (over U_{ff}) upon electron addition. The Anderson impurity Hamiltonian is written as:

$$\mathcal{H}_{AI} = \varepsilon_f n_f + \sum_k \varepsilon_k n_k + V_{fk} \sum_k (a_f^\dagger a_k + a_k^\dagger a_f) + U_{ff} n_f n_f \tag{3.6}$$

In this equation second quantization is used and $a_f^\dagger$ denotes the creation of the localized f-state; $n_f (= a_f^\dagger a_f)$ is the occupation-number operator of the localized state. For cerium compounds their 2 or 3-peaked $3d$-XPS spectrum could be accounted for by a ground state consisting of f^0-state plus a $f^1\underline{k}$ state where one electron is transferred from the band to the localized state, (plus eventually a $f^2\underline{k}\underline{k}'$-state). In the final state the effects of the core hole, the core level binding energy ($\varepsilon_{\underline{c}}$) and the core hole potential ($U_{\underline{c}f}$), are added to

the Hamiltonian. The model parameters, ε_f, V_{fk}, U_{ff} and U_{cf} have to be optimized from experiment. Alternatively these parameters have to be calculated from ab-initio calculations, and for example density functional and cluster calculations have been applied to determine these model parameters [143–145].

To include multiplet effects in the Anderson impurity description the different symmetries of the $4f$-electron states and the $3d$-core hole states have to be accounted for. This can be accomplished by an explicit summation over these symmetries (with a double summation over the U-terms) [133]. As in this procedure each individual atomic configuration is accounted for, it is possible to include the atomic multiplet terms. For the ground state this includes the Slater integrals F^2_{ff}, F^4_{ff} and F^6_{ff} and the $4f$ spin-orbit coupling. In the final state the Slater integrals concerning the df-coupling and the $3d$ spin-orbit coupling have to be included. The final state Hamiltonian uses eight Slater integrals, taken from the Hartree-Fock calculation (and reduced to 80%), two spin-orbit coupling strengths from the Hartree-Fock calculation, and empirical or calculated values for ε_f, ε_d, U_{ff}, U_{fd}, V_{fk} and $\sum_k \varepsilon_k$ (the shape of the band). Despite the numerous parameters needed, it has been shown convincingly that the model reached an unprecedented efficiency for systems like CeO_2 or CuO and related compounds. However for a reliable application to new systems it is necessary to perform extensive parameter optimizations whereby difficulties can arise because some parameters have counteracting effects on the spectral shape. Additional problems can arise in the study of systems in the middle of transition metal or rare earth series as the number of configurations is too large for the use of a similar rigorous approach. For $3d$ x-ray absorption on cerium compounds it has been found that the main effect of the implementation into the impurity model is a narrowing of the atomic multiplet [137]. For the heavily debated $4d$ x-ray absorption spectrum of CeO_2 Kotani et al. convincingly showed that the actual spectral shape is a direct consequence of the interplay between atomic multiplets and the interactions of the localized states with the band [138].

The impurity model for transition metal compounds

The impurity model has been applied to transition metal compounds by the Groningen group. The many body description has been started by van der Laan et al. in the description of the photoemission spectra of copper dihalides [152]. Zaanen et al. applied the Anderson impurity model to the nickel dihalides, whose ground state is dominated by a $3d^8$ configuration but in which going from the fluoride to the iodide the admixture of the $3d^9\underline{L}$ configuration becomes more dominant as a result of a decreasing charge transfer energy (Δ) [65]. Compared to the cerium-compounds for the nickel halides the correlations are smaller and the interaction between the localized state and the band is larger which results, given the variations in Δ, in a complicated, but nicely explained, variation of the nickel $2p$ XPS spectral shape. Comparison of the $2p$ XPS spectra with the $2p$ XAS spectra of the nickel dihalides shows that whereas the XPS spectra showed drastic spectral changes, the x-ray absorption spectra resemble each other much more closely and furthermore the main features of all spectra are reasonably accounted for by a single configuration crystal field multiplet calculation. The agreement is increased considerably after implementation of the

multiplets in the impurity model. The main result is, apart from the appearance of small satellites, a reduction of the multiplet splittings [151], a result similar to that obtained for cerium compounds [137].

The impurity model versus Slater integral reduction

From the foregoing it can be concluded that there are two approaches to include hybridization effects in the single configuration multiplet spectra: (1) the reduction of the Slater integrals from their atomic values and (2) the implementation of the atomic multiplets into the impurity model. The impurity model is more rigorous and has been proven to account well for the experimental spectra. Its disadvantage however is that it is a more complicated calculation. Specifically for compounds in the middle of the transition metal series (with a large number of configurations), impurity calculations similar to those performed for the nickel halides [65] are not possible. Therefore it would be of great help if Slater integral reduction would reproduce the experimental spectra (apart from the intensity coming from the satellites, which is not accounted for in this approach). Because only the Slater integrals are modified the calculation is exactly equivalent to a normal crystal field multiplet calculation.

To test the validity of Slater integral reduction and to compare it with the impurity model, the nickel dihalide spectra are simulated. Divalent nickel presents a special case for the crystal field multiplet calculations as the $2p^5 3d^9$ final state contains only a single $3d$-hole and thus does not contain any dd-correlations. This simplifies the multiplet calculation and, apart from the spin-orbit coupling which is not essential for this problem, only two sets of Slater integrals remain: F^2_{dd} and F^4_{dd} for the initial state and F^2_{pd}, G^1_{pd} and G^3_{pd} for the final state. Furthermore the x-ray absorption spectral shape is not sensitive to the actual values of the ground state dd integrals as the $^3A_2$ ground state is the sole state of this symmetry and consequently does not mix with any excited state. Thus the only set of parameters which determine the spectral shape are the final state pd-Slater integrals. To test the Slater integral reduction they were stepwise reduced from their atomic values and figure 3.19 shows the corresponding spectral changes. It should be noted that a cubic crystal field a value of 0.9 eV is used, in agreement with the values (for all nickel halides) determined from optical spectroscopy. In the original paper on the impurity model a crystal field value of 1.5 eV had been used (corresponding to NiO).

For comparison the experimental spectra are reproduced from Ref. 151. It can be seen that with the reduction of the pd Slater integrals the splitting between the main peak and its high-energy shoulder is reduced, a similar effect to that obtained in the impurity model calculations. The experimental spectra show exactly the same trend in going from the fluoride to the iodide. Also the modifications in the L_2 edge are reproduced nicely. From this agreement it can be concluded that in case of the nickel dihalides the Slater integral reduction gives a good account of the main spectral modification upon increasing hybridization (apart from the satellite structure). It is important to note that the amount of Slater integral reduction gives an alternative measure of the amount of hybridization. For the halides it is found that whereas the fluoride corresponds to the atomic values, for chloride,

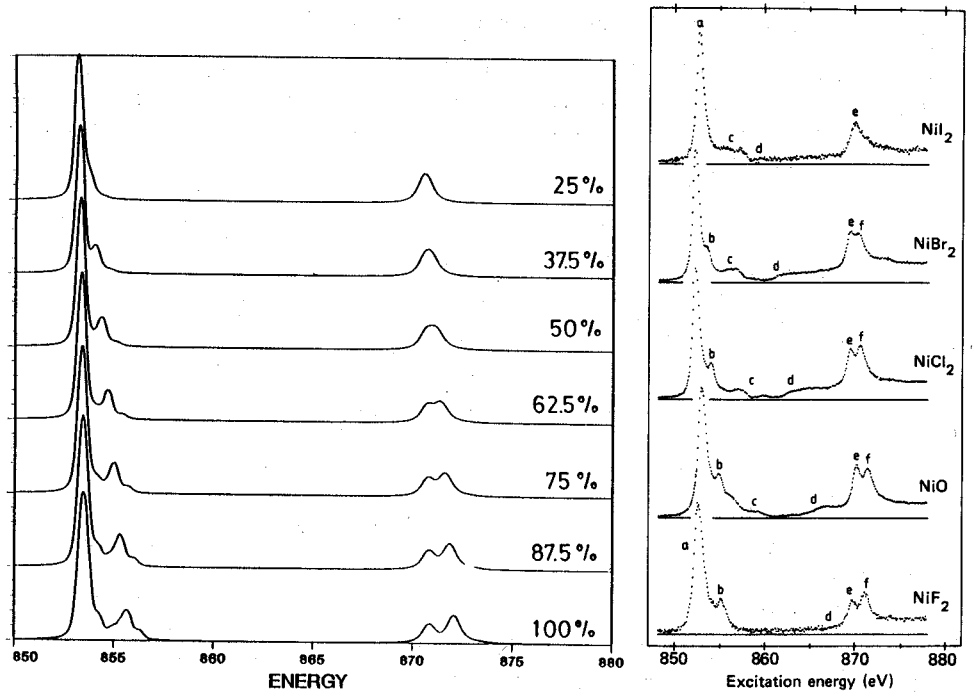

Figure 3.19: Reduction of Slater integrals (left) compared with experiment (right). The experimental data are reproduced from Ref. 65. (100 % relates to the atomic values).

bromide and iodide the Slater integrals have to be approximately reduced to respectively 75%, 65% and 25% of their atomic value. This trend is a nice example of the so-called 'nephelauxatic series' obtained from the analysis of optical spectra [154, 155]. There is also a close relation between the Slater integral reduction and the ratio of the charge transfer energy (Δ) and the interaction strength with the band (V_{dk} or T). For NiF_2 $(\Delta/T)^2$ is 0.09 [153] and the atomic Slater integrals are correct. For NiI_2 $(\Delta/T)^2$ is 1.8 and the effects of the Slater integrals on the spectral shape is negligible. For $NiCl_2$ and $NiBr_2$ the values are respectively 0.3 and 0.6, and an intermediate situation occurs for which the values of the Slater integrals are reduced but still they have considerable influence on the spectral shape.

Why are the satellites so small in x-ray absorption ?

In this section it is argued why the charge transfer satellites are small or absent in $2p$ x-ray absorption spectra, in contrast to their importance in the $2p$ XPS spectra of ionic $3d$-metal compounds. Furthermore the absence of satellite structures is an additional justification of the Slater integral reduction method.

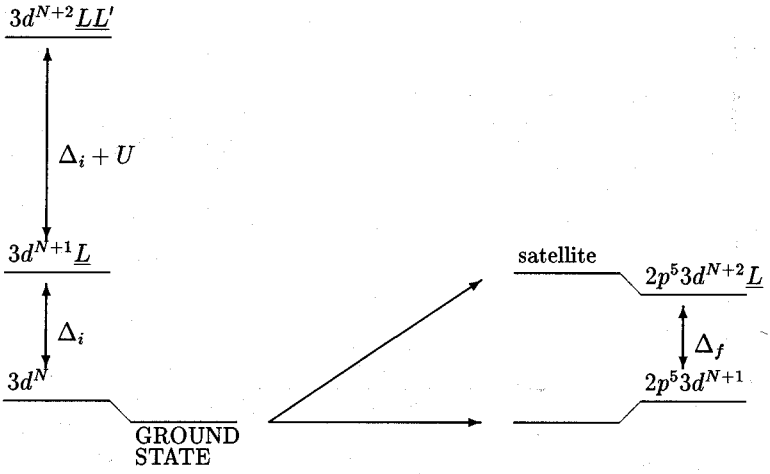

Figure 3.20: Initial and final states of metal $2p$ x-ray absorption in the charge transfer model. The ground state is formed by the bonding combination of $3d^N + 3d^{N+1}\underline{L}$. The arrows indicate the transitions to the bonding and anti-bonding (= charge transfer satellite) final states.

Figure 3.20 sketches the energy levels in the charge transfer model. The ground state has $3d^N$-character which mixes with $3d^{N+1}\underline{L}$ character after hybridization is taken into account. The energy of the $3d^{N+2}\underline{LL'}$ is large and its contribution to the ground state can be neglected. The consequence of the interaction between $3d^N$ and $3d^{N+1}\underline{L}$-character is the forming of bonding and anti-bonding states which both consist of admixtures of these two configurations. Similarly in the final state the interaction between $2p^5 3d^{N+2}\underline{L}$ and $2p^5 3d^{N+1}$-character gives rise to bonding and anti-bonding combinations. In the charge transfer model it is found that the amount of admixture of $3d^{N+1}\underline{L}$-character in the ground state is given as the hopping (T) over the energy difference (Δ) squared. In the final state Δ_f is approximately equal to Δ_i - Q + U and because Q is in general slightly larger than U, Δ_f is slightly decreased which results in an increased hybridization. Possibly the hopping is increased in the final state which will further increase the hybridization [65]. Under the assumption that the hybridization is not modified, all intensity goes to the

bonding combination of the final state. Furthermore under neglect of interference effects the overall spectral shape is given as the superposition of the crystal field multiplets of the $3d^N \rightarrow 2p^5 3d^{N+1}$ and the $3d^{N+1}\underline{L} \rightarrow 2p^5 3d^{N+2}\underline{L}$ transitions. Thus the crystal field multiplet analysis as used in section 3.3 and 3.4 is extended with the superposition of the transitions from the $3d^{N+1}\underline{L}$-character of the ground state. If the hybridization is increased the main effect will be that the amount of $2p^5 3d^{N+1}$-character in the anti-bonding state increases with respect to (the $3d^N$-character in) the initial state. This will result in transitions to the anti-bonding combination, hence to a charge transfer satellite as is for example observed for the nickel-halides [151]. In summary it can be concluded that hybridization itself gives rise to a reduction of the energy splittings in the multiplet and to the superposition of transitions from $3d^{N+1}\underline{L}$-character, but that only the *changes* in the hybridization will give rise to a satellite structure.

In x-ray absorption the change in hybridization is considerably smaller than for XPS, which is a direct consequence of the charge conservation. The mere absence of charge transfer satellites explains the good agreement of the x-ray absorption spectra with the crystal field multiplet calculations and additionally it is a partial justification of the Slater integral reduction method.

3.8. Electronic structure calculations

In contrast to sections 3.2 to 3.7, in this section the emphasis will be on the weakly correlated limit. The electronic structure of ordered solids is, in the weakly correlated limit, accurately described with density functional theory within the local density approach [156,157]. As discussed in chapter 1 the x-ray absorption cross section is in the weakly correlated limit related to the unoccupied density of states with one extra valence electron and with the presence of a core hole ($\mathcal{P}_{\underline{c}N+1}$): the final state rule [158,159]. Under the additional assumption that the effects of the core hole as well as the extra valence electron are negligible, the density of states which results from a ground state calculation, the non-observable N-particle density of states ($\mathcal{P}_N$), bears close resemblance to the spectral shape ($\mathcal{P}_N \approx \mathcal{P}_{\underline{c}N+1}$). Evidently this assumption breaks down completely for the rare earth metals and their compounds. In the preceding sections it was shown that also for the metal $2p$ x-ray absorption edges of the $3d$-metal compounds, this assumption is violated and correlation effects dominate the spectral shape. Despite the fact that from the metal $2p$ spectra the conclusion is drawn that $3d$-metal oxides are highly correlated, in this section the model of a weakly correlated system is tested for the analysis of the oxygen $1s$ x-ray absorption spectra of the $3d$-metal oxides. There are some favourable factors for the use of the description within the weakly correlated limit:

- The oxygen $1s$ core hole bears no angular momentum and hence there are no multipole interactions of the core hole with the electrons in the valence band. (The G^1_{sp} Slater integral (exchange coupling) is neglected).

- X-ray absorption is a local process which is charge conserving with the consequences that the modifications in the hybridization are small and mainly local (also it places

x-ray absorption close to the adiabatic limit).

- The core hole is located on the oxygen site and the $3d$ valence electrons are localized mainly on the metal sites, hence (the effect of) the core hole potential is small. However still the oxygen $1s$ core hole will attract the valence electrons to the oxygen site and thereby it tends to counteract the correlations within the $3d$-band.

The density of states is calculated within the local density approximation of density functional theory, which as discussed in the introduction presents an accurate ab-initio method to solve the Schrödinger equation for weakly correlated, ordered solids. The Hamiltonian to solve includes respectively the kinetic term, the Hartree term, the nuclear term and the exchange-correlation term:

$$\mathcal{H} = -\frac{1}{2}\nabla^2 + \int \frac{n(r')}{|r - r'|} d^3r' + V_N(r) + \frac{\partial E_{xc}[n]}{\partial n} \tag{3.7}$$

The exchange-correlation energy is approximated according to the Hedin-Lundqvist expression [160]. The Hamiltonian itself is dependent on the electron density (the wavefunctions as far as occupied), hence the solution is found in a self-consistent iterative procedure. A specific starting set of wavefunctions $\phi^{in}(r)$ is chosen, the Hamiltonian is determined and thereafter the eigenvalue-problem is solved which yields a new set of wavefunctions $\phi^{out}(r)$. This new set of wavefunctions can be used for the next cycle of the calculation. The actual iterative procedure uses a specific combination of the wavefunction-sets to speed up the convergence. For example a linear combination of $\phi^{out}_{N-1}(r)$ and $\phi^{in}_{N-1}(r)$ can be used.

3.8.1. The Localized Spherical Wave method

To tackle the calculation of an actual solid a number of numerical methods have evolved, differing in specific choices with respect to the treatment of the valence and core electrons, the division of space and the effectiveness to shape the calculation into a manageable form. The specific method used is the Localized Spherical Wave (LSW) method, which originates from the Augmented Spherical Wave (ASW) method of Williams et al. [161]. With respect to ASW, there are two essential developments:

- The idea of tight-binding (localized) muffin-tin orbitals, suggested by Andersen and Jepsen for the linearized muffin-tin orbital (LMTO) method [162, 163], has been reformulated and implemented for the ASW method by F. Springelkamp et al. [164].

- The extended basis set option was added to LSW in order to describe appropriately the unoccupied states in the energy range higher than a few eV above the Fermi level [165].

The LSW method, including the extended basis sets has been applied to a number of systems, including Ag_2O [165, 166], CuO [167, 168], TiSi and other silicides [166, 169] and MoNi-alloys [170].

Treatment of valence electrons

All band structure methods divide the electrons into core and valence electrons of which only the latter are expanded in reciprocal space to derive the band structure. The LSW method uses spherical waves to expand the valence electrons, contrary to linearized augmented plane wave (LAPW) and LMTO methods which use plane waves. For each angular quantum-number and for each site the wavefunction is written as a radial Hankel function [161] times the respective spherical harmonics (Y_{LM}). The Hankel functions of a specific site are at another site expanded in a series of Bessel functions [171].

Treatment of core electrons

The core electrons can be treated in two ways: they can be frozen to their atomic values or alternatively they can be calculated after each step in the iteration procedure. This second approach, which is used in the LSW calculation, allows one to detect the reaction of the core levels on the hybridizational effects of the valence electrons.

Division of space

A major problem in all density functional methods is to divide the space of the unit cell into manageable sections. There are two main approaches known as muffin-tin and atomic sphere approximation. In the muffin-tin approach each atom is surrounded by a sphere in such a way that, if possible, they just touch each other. Inside the spheres an atomic potential is used and the interstitial region outside the spheres is approximated with a flat potential. In the atomic sphere approximation a similar approach is followed but the radii of the spheres are chosen as to fill a volume equal to the total volume of the unit cell. This procedure creates overlapping spheres, so there are regions inside the unit cell which are encompassed in two or sometimes three spheres. Additionally in the atomic sphere approximation the total space of the interstitial regions is much smaller than in the muffin-tin approach. As each atomic site is surrounded by a sphere the overlap occurs in the bonding directions whereas the interstitial regions are found in non-bonding directions. The choice of the atomic radii is important and for this purpose one can use tables of radii in the ionic and covalent limits [172]. However many, if not all, interesting compounds contain an intermediate character and the radii have to be optimized. In crystal structures which have a filling which is rather far from closed-packed the overlapping spheres give rise to numerical problems and therefore a method has been developed to improve the division of space by creating empty spheres, that is spheres which are allocated to open places in the crystal structure and which consequently have no ion core.

Number of basisfunctions

In standard LSW calculations one Hankel function per site and per l-value is used. In $SrTiO_3$ there are 5 atoms per unit cell [57] and in the self-consistent iteration process s, p and d Hankel functions are allocated to the strontium, titanium and oxygen sites. It is

necessary to include empty spheres at a 12-fold degenerate site and a Hankel function of s-symmetry is assigned to each empty sphere. As a result the total size of the matrix is 5 times 9 for the atoms, plus 12 (times 1) for the empty spheres. The set of Bessel functions used in the expansion is limited to $l \leq 3$. For the empty spheres only s, p and d Bessel functions are included.

Extended basis sets

In order to give an accurate description of the states above the Fermi level, which is essential for the comparison with the x-ray absorption cross section, it is necessary to increase the number of basis-functions to more than one per angular momentum [165]. Because the potential is dependent only on the occupied states, which are hardly influenced by the addition of new states at high energies, it is possible to use the potential as determined with the smaller basis. Thus it is not necessary to repeat the self-consistent calculation and one can manage with a single calculation to determine the density of states within the extended basis set.

3.8.2. LSW calculation of the density of states of $SrTiO_3$

$SrTiO_3$ has (at room temperature) a cubic perovskite crystal structure (O_h^1). The positions of the ions in the unit cell are given in table 3.10 For numerical reasons, it is necessary to include empty spheres at the 12-fold degenerate $(\frac{1}{2}, x, x)$-positions with the x as given in the table. Two sets of radii have been used. A covalent set with a small oxygen radius (I), and a more ionic set with an increased oxygen radius (II). The two sets of radii given in table 3.10 are optimized touching spheres. The actual radii are renormalized from these values by multiplication with the total volume of the unit cell over the total volume of the given spheres. The renormalization values ($V_{WS}/\sum_i V_i$) are given in table 3.10. The densities of states emerging from these two sets of radii are, within the accuracy needed for x-ray absorption, equal to each other which is an additional check for the correctness of the density of states.

The basis set used in the calculation is given in table 3.11. The size of the Hamiltonian is 57. It was checked that inclusion of the $2p$-Hankel functions for the empty spheres, which increases the Hamiltonian size to 83, did not have any detectable effect. The k-points in the self-consistent iteration procedure are chosen in a 8 by 8 by 8 grid in the unit cell, which from symmetry arguments reduces to 35 points. The iteration procedure converges after approximately 25 cycles. With the self-consistent potential the density of states is calculated with an extended basis set, in which apart from the Hankel functions as given in table 3.10, also oxygen $3s$ and $3p$ states are included. Furthermore the strontium and titanium $4f$-states have been included in the Hamiltonian, which increases its size to 83. The density of states is calculated with a 16 by 16 by 16 grid of k-points, which is reduced to 165 points in the irreducible zone.

Results

El.	site		radii (I)	radii (II)
Sr	$(0,0,0)$	*1a*	1.70	1.57
Ti	$(\frac{1}{2},\frac{1}{2},\frac{1}{2})$	*1b*	1.05	0.92
O	$(\frac{1}{2},\frac{1}{2},0)$	*3c*	0.90	1.03
Ze	$(\frac{1}{2},x,x)$	*12j*	0.51 ($x=0.19$)	0.50 ($x=0.13$)
$\cdot V_{WS}/\sum_i V_i$			1.130	1.147

Table 3.10: Unit cell parameters and sets of radii used in the LSW-calculation

El. (N_s)	core	Hankel	N_H	Bessel	N_{tot}
Sr	$1s2s2p$	$5s$		$+4f$	
(1)	$3s3p3d$	$5p$	9		16
	$4s4p$	$4d$			
Ti	$1s2s2p$	$4s$		$+4f$	
(1)	$3s3p$	$4p$	9		16
		$3d$			
O	$1s$	$2s$		$+4f$	
(3)		$2p$	9		16
		$3d$			
Ze		$1s$	1	$+2p$	9
(12)				$+3d$	

Table 3.11: Number of Hankel functions in the Hamiltonian (N_H) and number of Bessel fuctions used in the expansion at other sites.

Figure 3.21 shows from bottom to top the total density of states and the partial density of states for the strontium, the titanium and the oxygen sites. The zero refers to the highest filled state. The main features in the DOS are the oxygen $2p$-band between -5 and 0 eV. It is dominated by oxygen $2p$ character, which can be checked from figure 3.22 in which the oxygen states are projected to the respective angular momenta. The oxygen $2p$-band is split in two sub-bands: the (lower) bonding band has a relatively larger contribution of titanium and strontium than the non-bonding band. Figures 3.22 give the angular momentum projected states for respectively titanium, strontium and oxygen.

The first band of unoccupied states is the rather narrow band between 2 and 4 eV,

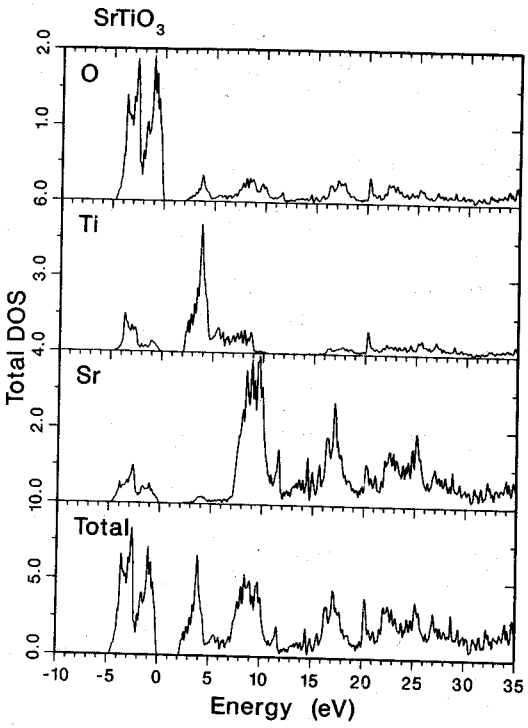

Figure 3.21: $SrTiO_3$ density of states. The total density of states (bottom) is split in the partial strontium, titanium and oxygen density of states.

which is dominated by titanium $3d$-character. It represents the t_{2g} states which in a tight-binding picture are only π anti-bonding. The next band, between 4 and 9 eV, is related to the titanium $3d$ states of e_g character. It has rather low intensity and a relatively large dispersion. The e_g-band overlaps with the strontium $5d$ band between 7 and 10 eV. Notice that the strontium $6s$-band is split into a part below and above the $5d$-band.

Under the assumption that $SrTiO_3$ can be described in the weakly correlated limit and with the approximation that $\mathcal{P}_{\underline{c}N+1} \approx \mathcal{P}_N$, the oxygen p-projected density of states simulates the oxygen $1s$ x-ray absorption spectral shape. In principle the density of states has to be modified with the transition matrix elements which are energy dependent, though it is expected that the effects of the matrix elements are not essential [174]. The oxygen p-projected density of states as given in figure 3.22 is broadened with a Lorentzian to mimic the lifetime of the oxygen $1s$ core hole and with a Gaussian to mimic the experimental resolution. Figure 3.23 compares the broadened oxygen p-projected density of states with the oxygen $1s$ x-ray absorption spectrum. The peaks in the broadened spectrum relate to respectively the oxygen p contribution to the t_{2g}-band at about 3.5 eV and the strontium $5d$-band between 7 and 10 eV. The shoulder at 12 eV relates mainly to oxygen p-character hybridized with strontium $6s$-states as can be checked in figure 3.22. The peak at about 17 eV marks the onset of the titanium $4sp$-band and the structure at about 23 eV also relates to this band. The experimental spectrum bears resemblance to the theoretical curve and the peaks discussed can also be found in the experiment, though their calculated energy position

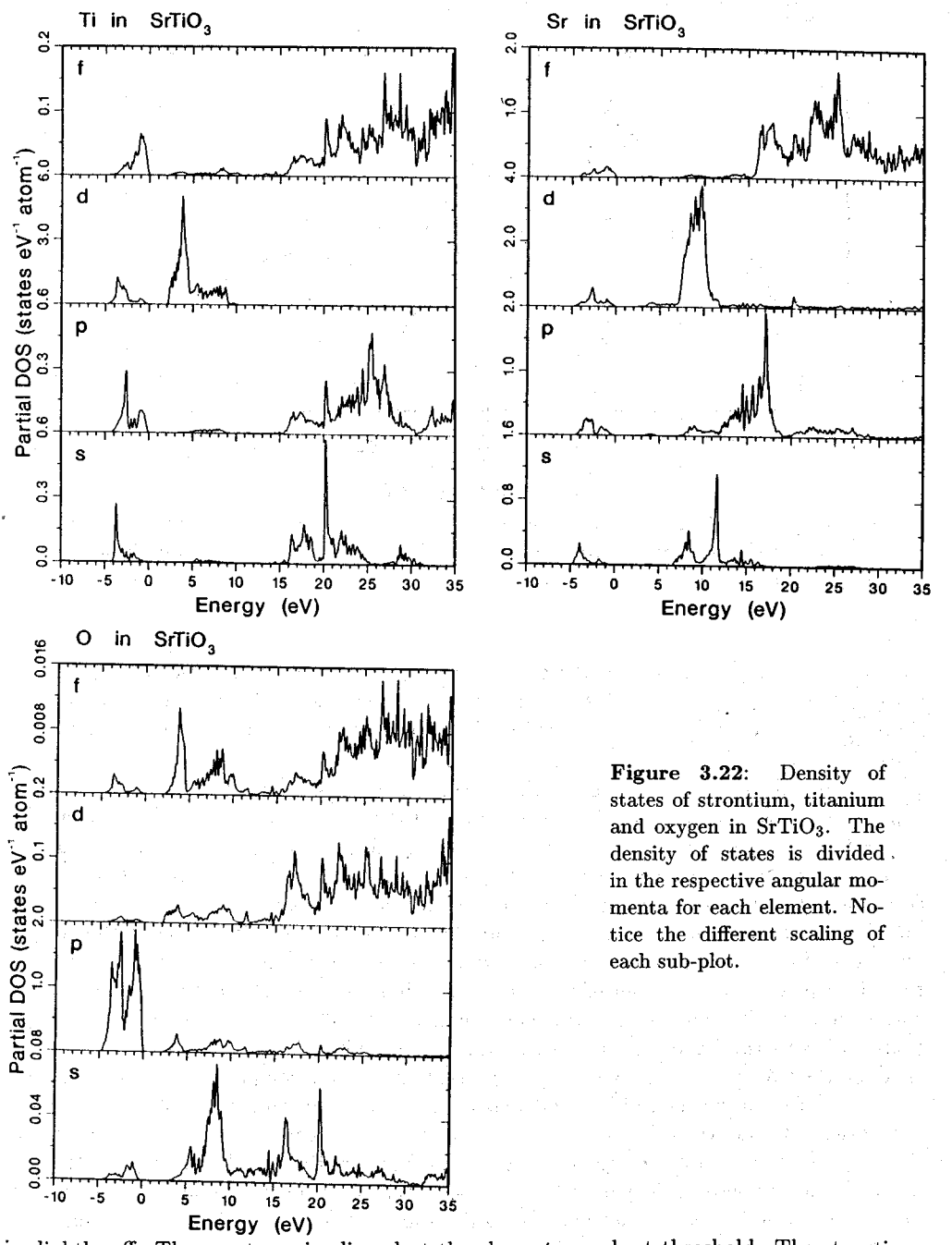

Figure 3.22: Density of states of strontium, titanium and oxygen in $SrTiO_3$. The density of states is divided in the respective angular momenta for each element. Notice the different scaling of each sub-plot.

is slightly off. The spectrum is aligned at the sharp t_{2g}-peak at threshold. The strontium

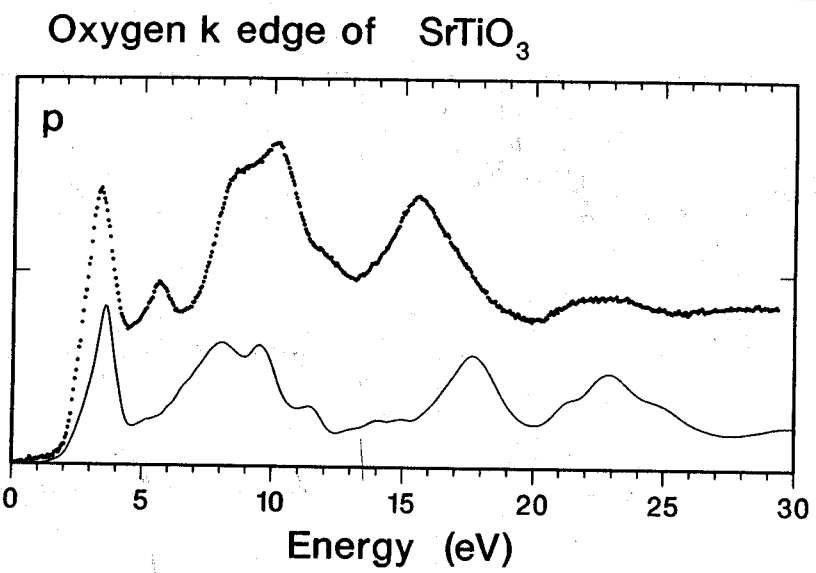

Figure 3.23: The oxygen $1s$ x-ray absorption spectrum of $SrTiO_3$ (dots) compared with the broadened oxygen p projected density of states (solid line). The scaling of the y-axis is arbitrarily.

$5d$-band including its $6s$-shoulder are found at slightly higher energy in the experiment whereas the peaks related to the titanium $4sp$-band are found at slightly lower energy. The sharp e_g-peak present in the experiment is visible as a weak shoulder only in the calculated density of states.

As indicated an approximation of the present analysis is the usage of the ground state density of states. Qualitatively it can be expected that an oxygen $1s$ core hole affects the spectral shape mainly as an attractive potential which pulls weight to the bottom of the respective bands (see also next section). Especially the narrow $3d$-bands are sensitive to the core hole potential and it is to be expected that the final state oxygen p density of states pile up at the bottom of the t_{2g} and the e_g-band. The t_{2g}-band is already narrow in the ground state and after the broadening little effect will be visible. However the e_g-band is expected to form a peak at the bottom of the band, as is indeed observed. From the comparison with experiment it is noticed that the bands related to strontium are found at higher energy compared with the bands related to titanium, which might indicate a stronger core hole effect on the states which are bonded to the titanium sites (as compared with the strontium sites). Additional effects which might explain part of the discrepancies observed include correlations effects, which are not treated correctly in the local density methods. As far as the major structures are concerned the agreement between the calculated oxygen p density of states and the observed oxygen $1s$ x-ray absorption spectrum is reasonably good, but the fine details as well as the exact energy-positions are influenced by effects not included in the N-particle density of states.

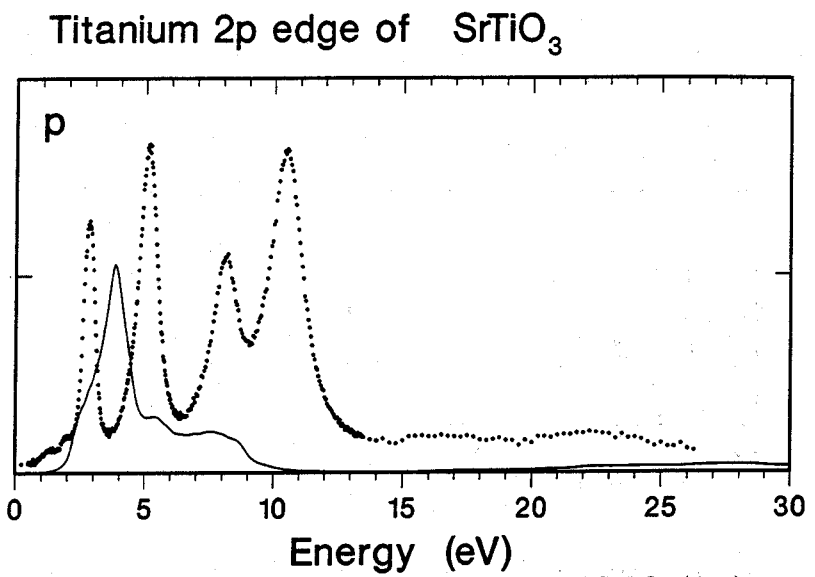

Figure 3.24: The titanium $2p$ x-ray absorption spectra of $SrTiO_3$ (dots) compared with the broadened titanium d projected density of states (solid line). The scaling of the y-axis is arbitrarily.

To show the importance of correlation effects for the metal $2p$ x-ray absorption edge, as discussed in the preceding sections, figure 3.24 compares the experimental spectrum with the titanium $3d$-projected density of states. The multipole correlation effects in combination with the $2p$ spin-orbit coupling and the cubic crystal field give rise to a multiplet structure consisting of seven sharp peaks which was explained in detail in section 3.3. These interactions make a N-particle density of states approach to the spectrum useless as is obvious from the large disagreement.

An LSW-calculation similar to the one described for $SrTiO_3$ has been performed for $LaTiO_3$. In section 4.4 the density of states description of $SrTiO_3$ and $LaTiO_3$ is used to discuss the oxygen $1s$ x-ray absorption spectra of the series of $La_{1-x}Sr_xTiO_3$-compounds and a series of similar perovskites with respectively manganese, iron and cobalt.

LSW results for CuO

To place the calculation of $SrTiO_3$ in perspective, a similar LSW for CuO ($3d^9$) is discussed shortly. The details are discussed by Grioni et al. [168]. The $3d$-band in CuO contains 9 electrons and is situated between -3 and +1 eV and the oxygen $2p$ band is with respect to $SrTiO_3$ shifted to lower energy (-7.5 to -3 eV). Above the $3d$-band there is a gap of approximately 2 eV followed by a slowly rising copper $4sp$-band. The density of states calculation has a band crossing the Fermi level, which is in contrast to the finding that CuO is an insulator. This error is most likely a consequence of the incomplete treatment of

correlation (and/or the incorrect treatment of the spin and orbital polarization).

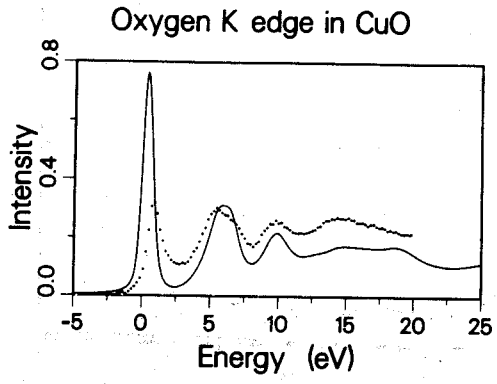

Figure 3.25: The oxygen $1s$ x-ray absorption spectrum of CuO compared with the broadened oxygen p-projected density of states. Reproduced from Ref. 168.

As there is one $3d$-hole per copper this hole will tend to localize, thereby prohibiting electric conduction. Figure 3.25 compares the oxygen $1s$ x-ray absorption spectrum with the broadened oxygen $2p$ density of states. The agreement is good apart from the $3d$-band which has an offset of 0.5 eV and an intensity which is far too high theoretically. The high intensity in the theoretical spectrum is greatly reduced after inclusion of the core hole. The energy offset however cannot be related to the core hole as it is also present in the BIS spectrum [167]. The offset is therefore related to an incomplete treatment of (correlation within) the $3d$-band.

3.8.3. Inclusion of core hole effects

The core hole can be included in the LSW electronic structure calculations by the removal of a core electron of one of the atoms. To reduce non-physical interactions between two sites with a core hole, the size of the unit cell is increased and a so-called supercell calculation is performed. This supercell calculation is a complete new self-consistent calculation of $\mathcal{P}_{\underline{c}N+1}$ instead of $\mathcal{P}_N$ and according to the final state rule [158, 159], the correct spectral shape (within the weakly correlated limit) is calculated in this manner. This approach has been applied successfully to the $L_{2,3}$-edges of Ag_2O [165, 166] and the silicon K edges of TiSi and $TiSi_2$ [166, 169].

An LSW calculation with an oxygen $1s$ core hole has been performed for $LiCoO_2$ [175]. In this compound cobalt has the low-spin $3d^6$-configuration ($^1A_1$-symmetry). Consequently the density of states consists of the oxygen $2p$ band and the t_{2g}-band, which both are filled. The empty bands are the e_g-band and at higher energy the $4sp$-band and bands related to lithium. The oxygen $1s$ x-ray absorption spectrum probes the e_g-band and at higher energies the other empty bands. Figure 3.26 gives the comparison of the x-ray absorption spectrum with the density of states, with and without inclusion of the core hole. A general agreement is found and the overestimation of the intensity of the e_g-band is clearly removed

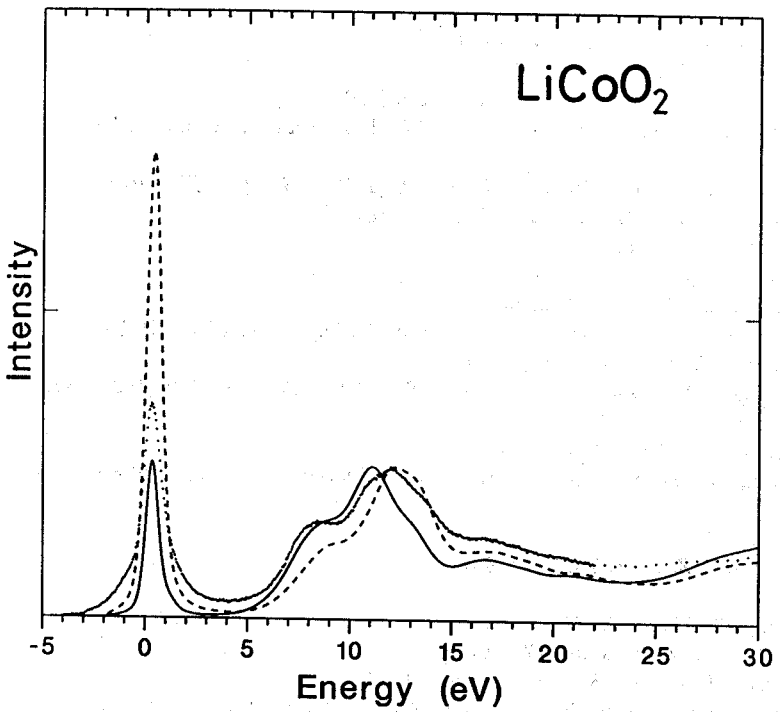

Figure 3.26: The oxygen $1s$ x-ray absorption spectrum of $LiCoO_2$ compared with the broadened oxygen p-projected density of states. The dashed line refers to the ground state density of states. The solid line refers to the density of states after inclusion of the oxygen $1s$ core hole: $\mathcal{P}_{\underline{c}N+1}$.

after inclusion of the core hole. In fact the density of states is slightly too low in the core hole calculation.

The core hole effect as calculated for the $LiCoO_2$ spectrum confirms that an oxygen $1s$ core hole will locally pull down states to the bottom of the bands. The result for $3d$-metal oxides is that the intensity of the narrow $3d$-band is reduced The bands at higher energy are less influenced because they are more extended. The main effect is a redistribution of spectral weight which in general results in an increase of intensity at the bottom of each band. As a final remark it is noticed that though the core hole LSW-calculations give the correct final state density of states needed to describe the x-ray absorption spectrum within the weakly correlated limit, for narrow band materials like the $3d$-metal oxides there will be omissions as the dd-correlations (or in other words fluctuations) are not treated correctly.

References

[1] R. Stumm von Bordwehr, *Ann. Phys. Fr.* **14**, 377 (1989).

[2] W.C. Röntgen, *Sitzungsberichte Phys. Mediz. Gesellschaft zu Würzburg* **137**, 132 (1895);

English translation in: *Nature* **53**, 274 (1896).
[3] H.G.J. Moseley, *Phil. Mag.* **26**, 1024 (1913).
[4] R. Sagnac, *Ann. Chim. Phys. Ser. VII* **23**, 145 (1901).
[5] C.G. Barkla, *Phil. Mag.* **22**, 396 (1911); C.G. Barkla and V. Collier, *Phil. Mag.* **23**, 987 (1912).
[6] N. Bohr, *Phil. Mag.* **26**, 1 (1913); *ibid.* **26**, 476 (1913); *ibid.* **26**, 857 (1913).
[7] W. Stenström, *Ann. Phys.(Leipzig)* **57**, 347 (1918).
[8] H. Fricke, *Phys. Rev.* **16**, 202 (1920).
[9] W. Kossel, *Z. Phys.* **1**, 119 (1920).
[10] J. Bergengren, *Z. Phys.* **3** 247 (1920).
[11] L. Pauling, *Phys. Rev.* **34**, 954 (1929); based on K. Fajans, *Z. Phys.* **50**, 531 (1928).
[12] W. Heisenberg, *Z. Phys.* **33**, 879 (1925).
[13] E. Schrödinger, *Ann. Phys. (Leipzig)* **79**, 361 (1926); *ibid.* **79**, 489 (1926); *ibid.* **80**, 437 (1926); *ibid.* **81**, 109 (1926).
[14] H. Hall, *Rev. Mod. Phys.* **8**, 358 (1936).
[15] R.D. Cowan, *The Theory of Atomic Structure and Spectra* (Univ. of California Press, Berkeley, 1981).
[16] Ref. 1; chapter 3.
[17] R. de L. Kronig, *Z. Phys.* **70**, 317 (1931).
[18] Ref. 1; page 399.
[19] J. Veldkamp, *Z. Phys.* **77**, 250 (1932).
[20] R. Smoluchowski, *Z. Phys.* **94**, 775 (1935).
[21] P.A.M. Dirac, *Proc. Roy. Soc. A.* **114**, 243 (1927).
[22] H.M. O'Bryan and H.W.B. Skinner, *Phys. Rev.* **45**, 370 (1934).
[23] H. Jones, N.F. Mott and H.W.B. Skinner, *Phys. Rev.* **45**, 379 (1934).
[24] J.E. Müller and J.W. Wilkins, *Phys. Rev. B.* **29**, 4331 (1984).
[25] R. Natoli and M. Benfatto, *J. Phys. Coll. C8.* **47**, 11 (1986).
[26] E. Lindberg, *Diss. Nova Acta Reg. Soc. Sci. Uppsalenius* **7**, IV, 7 (1931).
[27] Sandström, *Diss. Nova Acta Reg. Soc. Sci. Uppsalenius* **9**, IV, 2 (1935).
[28] K.C. Rule *Phys. Rev.* **68**, 246 (1945).
[29] E.A. Stewardson and P.A. Lee, *Proc. Phys. Soc. A.* **64**, 318 (1951); E.A. Stewardson and J.E. Wilson, *ibid.*, **69**, 93 (1956).
[30] H.F. Zandy, *Proc. Phys. Soc. A.* **65**, 1015 (1952).
[31] K.C. Williams, *Proc. Phys. Soc.* **87**, 983 (1966).
[32] H. F. Zandy, *Phys. Rev.* **162**, 1 (1967).
[33] F.H. Combley, E.A. Stewardson and J.E. Wilson, *J. Phys. B.* **1**, 120 (1968).
[34] T.M. Zimkina, V.A. Fomichev, S.A. Gribovskii and I.I. Zhukova, *Sov. Phys. Sol. State* **9**, 1128 (1967).
[35] V.A. Fomichev, T.M. Zimkina, S.A. Gribovskii and I.I. Zhukova, *Sov. Phys. Sol. State* **9**, 1163 (1967).
[36] R. Haensel, P. Rabe and B. Sonntag *Solid State Comm.* **8**, 1845 (1970).
[37] U. Fano, *Phys. Rev.* **124**, 1866 (1961); J.W. Cooper, *Phys. Rev. Lett.* **13**,762 (1964); U. Fano and J.W. Cooper, *Rev. Mod. Phys.* **40**, 441 (1968).
[38] J. L. Dehmer, A.F. Starace, U. Fano, J. Sugar and J.W. Cooper, *Phys. Rev. Lett.* **26**, 1521 (1971).
[39] A.F. Starace, *Phys. Rev. B.* **5**, 1773 (1972).

[40] J. Sugar, *Phys. Rev. B.* **5**, 1785 (1972).
[41] J.L. Dehmer and A.F. Starace, *Phys. Rev. B.* **5**, 1792 (1972).
[42] J.L. Dehmer, *J. Chem. Phys.* **56**, 4496 (1972).
[43] C. Froese, *Can. J. Phys.* **41**, 1895 (1963).
[44] S. Sugano, Y. Tanabe and H. Kitamura, *Multiplets of Transition Metal Ions* (Academic Press, New York, 1970).
[45] E.J. McGuire, *J. Phys. Chem. Solids* **33**, 577 (1972).
[46] N.N. Axelrod and M.P. Givens, *Phys. Rev.* **120**, 1205 (1960).
[47] B. Sonntag, R. Haensel and C. Kunz, *Solid State Comm.* **7**, 597 (1969).
[48] R.E. Dietz, E.G. McRae, Y. Yafet and C.W. Caldwell, *Phys. Rev. Lett.* **33**, 1372 (1974).
[49] L.C. Davis and L.A. Feldkamp, *Phys. Rev. B.* **15**, 2961 (1977).
[50] L.C. Davis and L.A. Feldkamp, *Phys. Rev. B.* **23**, 6239 (1981).
[51] R. Bruhn, B. Sonntag and H.W. Wolff, *Phys. Lett. A.* **69**, 9 (1978).
[52] L.C. Davis, *J. Appl. Phys.* **59**, R25 (1986).
[53] S.-I. Nakai, H. Nakamori, A. Tomita, K. Tsutsumi, H. Nakamura, C. Sugiura, *Phys. Rev. B.* **4**, 1870 (1974).
[54] S. Shin, S. Suga, H. Kanzaki, S. Shibuya and T. Yamaguchi, *Solid State Comm.* **38**, 1281 (1981).
[55] F. Brown, C. Gähwiller and A.B. Kunz, *Solid State Comm.*, **9**, 487 (1971).
[56] S. Asada, C. Satako and S. Sugano, *Technical Report of the Institute of Solid State Physics* (Univ. of Tokyo, 1974) A, 671.
[57] S. Asada, C. Satako and S. Sugano, *J. Phys. Soc. Jap.* **37**, 855 (1975).
[58] T. Yamaguchi and S. Sugano, *J. Phys. Soc. Jap.* **42**, 1949 (1977).
[59] R.P. Gupta and S.K. Sen, *Phys. Rev. B.* **10**, 71 (1974).
[60] R.P. Gupta and S.K. Sen, *Phys. Rev. B.* **12**, 15 (1975).
[61] S.P. Kowalczyk, L. Ley, F.R. McFreely and D.A. Shirley, *Phys. Rev. B.* **11**, 1721 (1975).
[62] T. Novakov, *Phys. Rev. B.* **3**, 2693 (1971).
[63] A. Kotani and Y. Toyozawa, *J. Phys. Soc. Jap.* **37**, 912 (1974).
[64] S. Asada and S. Sugano, *J. Phys. Soc. Jap.* **41**, 1291 (1976).
[65] J. Zaanen, C. Westra and G.A. Sawatzky, *Phys. Rev. B.* **33**, 8060 (1986).
[66] This in contrast to the calculations in this thesis for which essentially the atomic values are used and in general no reduction is applied.
[67] S. Suga, S. Shin, M. Taniguchi, K. Inoue, M. Seki, I. Nakada, S. Shibuya and T. Yamaguchi, *Phys. Rev. B.* **25**, 5487 (1982).
[68] S. Shin, S. Suga, M. Taniguchi, H. Kanzaki, S. Shibuya and T. Yamaguchi, *J. Phys. Soc. Jap.* **51**, 906 (1982).
[69] T. Yamaguchi, S. Shibuya, S. Sugano, *J. Phys. C.* **15**, 2625 (1982).
[70] T. Yamaguchi, S. Shibuya, S. Suga, S. Shin, *J. Phys. C.* **15**, 2641 (1982).
[71] B.T. Thole, G. van der Laan, J.C. Fuggle, G.A. Sawatzky, R.C. Karnatak and J.-M. Esteva, *Phys. Rev. B.* **32**, 5107 (1985).
[72] R.D. Cowan, *J. Opt. Soc. Am.* **58**, 808 (1968).
[73] B.T. Thole, R.D. Cowan, G.A. Sawatzky, J. Fink and J.C. Fuggle, *Phys. Rev. B.* **31**, 6856 (1985).
[74] P.H. Butler, *Point Group Symmetry Applications: Methods and Tables* (Plenum Press, New York, 1981).
[75] B.T. Thole, G. van der Laan and P.H. Butler, *Chem. Phys. Lett.* **149**, 295 (1988).

[76] G. van der Laan, B.T. Thole, G.A. Sawatzky and M. Verdaguer, *Phys. Rev. B.* **37**, 6587 (1988).
[77] K.M. Karplus and R.N. Porter, *Atoms and Molecules* (Benjamin Publ., Marlo Park, 1970).
[78] C.W. Nielson and G.F. Koster, *Spectroscopic Coefficients for the p^N, d^N and f^N Configurations* (M.I.T. Press, Cambridge Massachutes, 1963).
[79] E.U. Condon and G.H. Shortley, *The Theory of Atomic Spectra* (Univ. Press, Cambridge, 1935).
[80] J.S. Griffith, *The Theory of Transition Metal Ions* (Univ. Press, Cambridge, 1964).
[81] J. van Elp, PhD. thesis: *The electronic structure of doped late transition metal monoxides*, (University of Groningen, 1990).
[82] F. Hund, *Linienspektren und Periodisches System der Elemente* (Julius Springer, Berlin, 1927), page 124 ff.
[83] C.J. Ballhausen, *Introduction to Ligand Field Theory*, (McGraw-Hill, New York, 1962).
[84] B.T. Thole, G. van der Laan and P.H. Butler, *Chem. Phys. Lett.* **149**, 295 (1984).
[85] Jahn and Teller, *Proc. Roy. Soc.* **161**, 220 (1937).
[86] D. van de Marel, PhD. Thesis, (University of Groningen, 1985).
[87] J.C. Fuggle, G.A. Sawatzky and J.W. Allen (Eds): *Narrow Band Phenomena* (Plenum Press, New York, 1988); page 3.
[88] J.A. Wilson, *Adv. Phys.* **19**, 1 (1970).
[89] P. Carra and M. Altarelli, *Phys. Rev. Lett.* **64**, 1286 (1990).
[90] C. Brouder, *J. Phys. C.* **2**, 701 (1990).
[91] K. Kramers, *Akad. van Wetenschappen*, **33**, 959 (Amsterdam, 1930).
[92] E.T. Keve, S.C. Abrahams and J.L. Bernstein, *J. Chem. Phys.* **53**, 3279 (1970).
[93] B. Sinkovic, private comm.; C.T. Chen and F. Sette, *Physica Scripta* **T31**, 119 (1990).
[94] B. Sinkovic et al. to be published.
[95] C. Brouder, J.-P. Kappler and E. Beaurepaire, *Conference Proceedings of the 2nd European Conference on Progress in X-ray Synchrotron Radiation Research*, Eds. A. Balerna, E. Bernieri and S. Mobilio (SIF, Bologna, 1990), page 19.
[96] B. Poumellec, R. Cortes, G. Tourillon and J. Berthon, *Conference Proceedings of the 2nd European Conference on Progress in X-ray Synchrotron Radiation Research*, Eds. A. Balerna, E. Bernieri and S. Mobilio (SIF, Bologna, 1990), page 23.
[97] F.J. Himpsel, U.O. Karlsson, A.B. McLean, L.J. Terminello, F.M.F. de Groot, M. Abbate, J.C. Fuggle, J.A. Yarmoff, B.T. Thole and G.A. Sawatzky, *Phys. Rev. B.* **43**, 6899 (1991).
[98] J. Somers, *X-ray absorption spectroscopy of small molecules* in: *Unoccupied Electronic States*, Eds: J.C. Fuggle and J. Inglesfield, (Springer, Berlin, 1991).
[99] M. Pedio, J.C. Fuggle, J. Somers, E. Umbach, J. Haase, Th. Lindner, U. Höfer, M. Grioni, F.M.F. de Groot, B. Hilert, L. Becker and A. Robinson, *Phys. Rev. B.* **40**, 7924 (1989).
[100] *X-ray Absorption Fine Structure VI*, Ed. S.S. Hasnain, (Ellis Horwood, Chichester,1991); chapter IV, pages 191-282; references therein.
[101] M. Pedio, L. Becker, B. Hillert, S.D. Addato and J. Haase, *Phys. Rev. B.* **41**, 7462 (1990).
[102] A.B. McLean, L.J. Terminello and F.J. Himpsel, *Phys. Rev. B.* **41**, 7694 (1990).
[103] G. Schütz, W. Wagner, W. Wilhelm, P. Kienle, R. Zeller, R. Frahm and G. Materlik, *Phys. Rev. B.* **58**, 737 (1987).
[104] G. Schütz, R. Wienke, W. Wilhelm, W.P. Zeper, H. Ebert and K. Spörl, *J. Appl. Phys.* **67**, 4456 (1990).
[105] F. Baudelet, E. Dartyge, A. Fontaine, C. Brouder, G. Krill, J.P. Kappler and M. Piecuch,

Phys. Rev. B. **43**, 5857 (1991).
[106] P. Fisher, G. Schütz, M. Knülle, S. Stähler, A. Puschmann and W.D. Brewer, *BESSY-report 1990* (1991); page 197.
[107] M. Sacchi, unpublished results.
[108] F. Sette, C.T. Chen, Y. Ma, S. Modesti and N.V. Smith, *X-ray Absorption Fine Structure VI* Ed. S.S. Hasnain, (Ellis Horwood, Chichester,1991).
[109] C.T. Chen, F. Sette, Y. Ma and S. Modesti, *Phys. Rev. B.* **42**, 7262 (1990).
[110] H. Ebert, G. Schütz and W.M. Temmerman, *Solid State Comm.* **76**, 475 (1990).
[111] C. Brouder and M. Hikam, *Phys. Rev. B.* **43**, 3809 (1991).
[112] J.B. Goedkoop, PhD. Thesis, *X-ray dichroism of rare earth materials* (University of Nijmegen, 1989).
[113] S. Imada and T. Jo, *J. Phys. Soc. Jap* **59**, 3358 (1990).
[114] G. van der Laan and B.T. Thole, *Phys. Rev. B.* **43**, 13401 (1991).
[115] C.T. Chen, N.V. Smith and F. Sette, *Phys. Rev. B.* **43**, 6785 (1991).
[116] T. Jo and G.A. Sawatzky, *Phys. Rev. B.* **43**, 8771 (1991).
[117] G. van der Laan, B.T. Thole, G.A. Sawatzky, J.B. Goedkoop, J.C. Fuggle, J.-M. Esteva, R.C. Karnatak, J.P. Remeika and H.A. Dabkowska, *Phys. Rev. B.* **34**, 6529 (1986).
[118] M. Sacchi, R.J.H. Kappert, J.C. Fuggle and E.E. Marinero, *Appl. Phys. Lett.*, accepted for publication.
[119] M. Sacchi, O. Sakho and G. Rossi, *Phys. Rev. B.* **43**, 1276 (1991).
[120] R.J.H. Kappert, PhD. Thesis, (University of Nijmegen, in print).
[121] K. Rajnak and B.G. Wybourne, *Phys. Rev.* **132**, 280 (1963).
[122] K. Rajnak and B.G. Wybourne, *Phys. Rev.* **134**, 596 (1964).
[123] B.G. Wybourne, *Phys. Rev.* **137**, 364 (1965).
[124] B.G. Wybourne, *Spectroscopic Properties of Rare Earths*, (Interscience, New York, 1965), chapter 2,17.
[125] R.D. Cowan, *The Theory of Atomic Structure and Spectra*, (University of California Press, Berkeley, 1981), page 464.
[126] B.K. Sarpal, C. Blancard, J.P. Connerade, J.M. Esteva, J. Hormes, R.C. Karnatak and U. Kuetgens, *J. Phys. B.* **24**, 1593 (1991).
[127] B.T. Thole, G.A. Sawatzky, R. Karnatak and J.-M. Esteva, *Phys. Rev. B.* **33**, 4253 (1986).
[128] D.W. Lynch and R.D. Cowan, *Phys. Rev. B.* **36**, 9228 (1987).
[129] O. Gunnarsson and K. Schönhammer, *Phys. Rev. B.* **28**, 4315 (1983).
[130] O. Gunnarsson and K. Schönhammer, *Phys. Rev. B.* **31**, 4815 (1985).
[131] A. Kotani, H. Mizuta, T. Jo and J.C. Parlebas, *Solid State Comm.* **85**, 805 (1985).
[132] T. Jo and A. Kotani, *Solid State Comm.* **54**, 451 (1985).
[133] T. Jo and A. Kotani, *J. Phys. Soc. Jap.* **55**, 2457 (1986).
[134] A. Kotani, T. Jo, K. Okada, T. Nakano, M. Okada, A. Bianconi, A. Marcelli and J.C. Parlebas, *J. Magn. Magn. Mat.* **70**, 28 (1987).
[135] A. Kotani, *Many body effects in core-level spectroscopy of solids* in: *Core Level Spectroscopy*, Eds: J. Kanamori and A. Kotani, (Springer, 1988), page 3.
[136] T. Jo and A. Kotani, *theory of high energy spectroscopy in* CeO_2 in: *Core Level Spectroscopy*, Eds: J. Kanamori and A. Kotani, (Springer, 1988), page 34.
[137] T. Jo and A. Kotani, *J. Phys. Soc. Jap.* **57**, 2288 (1988).
[138] A. Kotani, H. Ogasawara, K. Okada, B.T. Thole and G.A Sawatzky, *Phys. Rev. B.* **40**, 65 (1989).

[139] T. Jo, *J. Phys. Soc. Jap.* **58**, 1452 (1989).
[140] S. Imada and T. Jo, *J. Phys. Soc. Jap.* **58**, 402 (1989).
[141] S. Imada and T. Jo, *J. Phys. Soc. Jap.* **58**, 2665 (1989).
[142] S. Imada and T. Jo, *Physica Scripta* **41**, 115 (1990).
[143] O. Gunnarsson, O.K. Andersen, O. Jepsen and J. Zaanen, *Phys. Rev. B.* **39**, 1708 (1989).
[144] M.S. Hybertsen, M. Schlüter and N.E. Christensen, *Phys. Rev. B.* **39**, 9028 (1989).
[145] A.K. McMahan, R.M. Martin and S. Satpathy, *Phys. Rev. B.* **38**, 6650 (1988).
[146] A. Kotani, T. Ikeda, K. Okada and H. Ogasawara, *J. El. Spec. Rel. Phen.* **51**, 229 (1990).
[147] T. Ikeda, K. Okada, H. Ogasawara and A. Kotani, *J. Phys. Soc. Jap.* **59**, 622 (1990).
[148] J.-I. Igarashi, *J. Phys. Soc. Jap.* **59**, 1868 (1990).
[149] J.-I. Igarashi, *J. Phys. Soc. Jap.* **59**, 348 (1990).
[150] H. Eskes and G.A. Sawatzky, *Phys. Rev. Lett.* **61**, 1415 (1988).
[151] G. van der Laan, J. Zaanen, G.A. Sawatzky, R. Karnatak and J.-M. Esteva, *Phys. Rev. B.* **33**, 4253 (1986).
[152] G. van der Laan, C. Westra, C. Haas and G.A. Sawatzky, *Phys. Rev. B.* **23**, 4369 (1981).
[153] Values derived from table II in Ref. 65.
[154] C.K. Jorgensen, *Absorption Spectra and Chemical Bonding in Complexes*, (Pergamon Press, Oxford, 1962).
[155] C.K. Jorgensen, *Modern Aspects of Ligand Field Theory*, (North Holland, Amsterdam, 1971).
[156] P.C. Hohenberg and W. Kohn, *Phys. Rev.* **136**, 864 (1964).
[157] W.Kohn and L.J. Sham, *Phys. Rev.* **140**, 1133 (1965).
[158] U. von Barth and G. Grossman, *Solid State Comm.* **32**, 645 (1979); U. von Barth and G. Grossman *Phys. Rev. B.* **25**, 5150 (1982).
[159] G.D. Mahan, *Phys. Rev. B.* **21**, 1421 (1980).
[160] L. Hedin and B.I. Lundqvist, *J. Phys. C.* **3**, 2065 (1971).
[161] A.R. Williams, J. Kübler and C.D. Gelatt Jr., *Phys. Rev. B.* **19**, 6094 (1979).
[162] O.K. Andersen and O. Jepsen, *Phys. Rev. Lett.* **53**, 2571 (1984).
[163] O.K. Andersen, O. Jepsen and D. Glötzel, *Highlights of Condensed Matter Theory*, Eds. F. Bassani, F. Fumi and M. Tosi (North-Holand, Amsterdam, 1985); page 59 ff.
[164] F. Springelkamp, M.T. Czyżyk and R.A. de Groot, (1987), unpublished; see also H. van Leuken, A. Lodder, M.T. Czyżyk, F. Springelkamp and R.A. de Groot, *Phys. Rev. B.* **41**, 5613 (1990).
[165] M.T. Czyżyk, R.A. de Groot, G. Dalba, P. Fornasini, A. Kisiel, F. Rocca and E. Burattini, *Phys. Rev. B.* **39**, 9831 (1989).
[166] M.T. Czyżyk and R.A. de Groot, *Conference Proceedings of the* 2^{nd} *European Conference on Progress in X-ray Synchrotron Radiation Research*, Eds: A. Balerna, E. Bernieri and S. Mobilio (SIF, Bologna, 1990); page 47.
[167] J. Ghijsen, L.H. Tjeng, J. van Elp, H. Eskes, J. Westerink, G.A. Sawatzky and M.T. Czyżyk, *Phys. Rev. B.* **41**, 5613 (1990).
[168] M. Grioni, M.T. Czyżyk, F.M.F. de Groot, J.C. Fuggle, B.E. Watts, *Phys. Rev. B.* **39**, 4886 (1989).
[169] P.J.W. Weijs, M.T. Czyżyk, J.F. van Acker, W. Speier, J.B. Goedkoop, H. van Leuken, H.J.M. Hendriks, R.A. de Groot, G. van der Laan, K.H.J. Buschow, G. Wiech and J.C. Fuggle, *Phys. Rev. B.* **41**, 11899 (1990).
[170] M.T. Czyżyk, K. Lawniczak - Jablonska, S. Mobilio, *Phys. Rev. B.*, submitted.
[171] Methfessel, PhD. Thesis: *Multipole Green Functions for Electronic Structure Calculations*

(University of Nijmegen, 1986); references therein.
[172] L.A. Shuvalov, *Modern Crystallography IV; Physical properties of crystals* (Springer series in Solid State Sciences, Berlin, 198x).
[173] R.W.G. Wyckoff, *Crystal Structures II* (Interscience, New York, 1964).
[174] J.J.M. Michiels et al., *Phys. Rev. B.*, submitted.
[175] M.T. Czyżyk and G.A. Sawatzky, *Phys. Rev. B.*, submitted.
[176] L.F. Mattheis, *Phys. Rev. B.* **6**, 4718 (1972).